FRETTING BEHAVIOR OF AISI 301 STAINLESS STEEL SHEET IN FULL HARD CONDITION

A Thesis
Presented to
The Academic Faculty
By
Michael Robert Hirsch

In Partial Fulfillment
Of the Requirements for the Degree
Master of Science in Mechanical Engineering

Georgia Institute of Technology
August 2008

FRETTING FATIGUE OF AISI 301 STAINLESS STEEL SHEET IN FULL HARD CONDITION

Approved by:

Dr. Richard W. Neu, Chairman
School of Mechanical Engineering
School of Materials Science and Engineering
Georgia Institute of Technology

Dr. David L. McDowell
School of Mechanical Engineering
School of Materials Science and Engineering
Georgia Institute of Technology

Dr. Itzhak Green
School of Mechanical Engineering
Georgia Institute of Technology

Date Approved: 26 June 2008

ACKNOWLEDGEMENTS

I would first like to thank my advisor, Dr. Neu for giving me the opportunity to work on this project and for all of his help along the way.

I thank my group members and office mates for sharing their knowledge and experience with me throughout my time here, especially Zach Moore and Kyle Webber.

Thank you to my committee members, Dr. McDowell and Dr. Green, for taking the time to review my work.

Thanks also to Dana Corporation, especially Frank Popielas and Rohit Ramkumar. This project would not have been possible without their support.

Lastly, I would like to thank my wife Alison and the rest of my family for their encouragement and understanding.

TABLE OF CONTENTS

LIST OF TABLES

LIST OF FIGURES

LIST OF SYMBOLS

a	Contact semi-width
a_0	Intrinsic crack length
AFM	Atomic Force Microscopy
B	Fatigue crack growth specimen thickness
BCC	Body Centered Cubic
c	Stick zone semi-width
C	Paris crack growth coefficient
CG	Course Grained
COF	Coefficient of Friction
CTE	Coefficient of Thermal Expansion
da/dn	Fatigue crack growth rate
EDM	Electrical Discharge Machining
EIFS	Equivalent Initial Flaw Size
EL	Elongation to failure
FCC	Face Centered Cubic
FDP	Fretting Damage Parameter
FF	Fretting Fatigue
FFDP	Fretting Fatigue Damage Parameter
FG	Fine Grained
GMR	Giant Magneto-Resistance sensor
GSR	Gross Slip Regime
HCF	High Cycle Fatigue
HCP	Hexagonal Close Packed
K_c	Critical stress intensity
K_{crit}	Critical stress intensity factor in NASGRO
m	Paris crack growth exponent
M(T)	Middle Tension crack growth specimen
M_d	Upper limit temperature for martensite formation

M_f	Lower limit temperature for presence of austenite
MFM	Magnetic Force Microscopy
MMPDS	Metallic Material Properties Data Sheet
MRFM	Material Response Fretting Map
M_s	Upper limit temperature for thermally induced martensite transformation
MSR	Mixed Slip Regime
N	Cycles to failure
n	Paris exponent in NASGRO equation
P	Normal Force
p	Exponent in NASGRO equation
p_0	Hertz peak normal pressure
PF	Plain Fatigue
PSR	Partial Slip Regime
Q	Global tangential force
q	Exponent in NASGRO equation
q(x)	Shear traction distribution
R	Force ratio
RCFM	Running Condition Fretting Map
S-N	Stress-life
SQUID	Superconducting Quantum Interference Device
TEM	Transmission Electron Microcopy
TRIP	Transformation Induced Plasticity
TS	Tensile Strength
VSM	Vibrating Sample Magnetometer
Vα	Volume fraction of α' martensite
W	Fatigue crack growth specimen width
XRD	X-Ray Diffraction
YS	Yield Strength
α'	BCC martensite phase
γ	FCC austenite phase
δ	Displacement

Δ	Displacement Amplitude
ΔK	Stress intensity range
ΔK_0	Threshold stress intensity range at R = 0
ΔK_{th}	Threshold stress intensity range
ΔP	Force range
$\Delta \varepsilon d$	Cyclic strain amplitude
ε	HCP martensite phase
μ	Coefficient of Friction
σ	Maximum Normal Stress Parallel to the Surface
τ	Shear stress

SUMMARY

Austenitic stainless steels, such as AISI 301, are widely utilized because of their many desirable properties. They are high strength, corrosion resistant, and typically have good machinability. Cold rolling causes a large increase in strength, partially due to a phase transformation from austenite to martensite. Because austenitic stainless steel is used as spring components at attachments, such as multilayer gaskets, it is important to understand its fretting behavior and the impact it has on the fatigue behavior.

Fretting, which can occur when two bodies in contact undergo a low amplitude relative slip, can drastically reduce the fatigue performance of a material. The extent of fretting damage is dependent on the material combination and is affected by many parameters, making it difficult to design against fretting. The primary parameters are the contact pressure, displacement amplitude, and coefficient of friction. This work develops a method for quantifying the extent of damage from fretting as a function of these parameters for a thin sheet of AISI 301 stainless steel in the full hard condition in contact with both ANSI A356 aluminum and AISI 52100 steel contacting bodies.

Tensile tests, fatigue tests, and crack growth tests were performed to characterize the baseline response of the AISI 301 stainless steel sheet in full hard condition (cold rolled approximately 50%). Fretting experiments were conducted on a Phoenix Tribology DN55 Fretting Machine using a fixture which was developed for holding thin specimens. The displacement amplitude and normal force were systematically varied in order to cover a range that could typically be experienced during service. The tribological

behavior was studied by analyzing friction force during cycling and inspecting the resulting surface characteristics.

After fretting damage was generated, the damaged specimens were cycled in tension in a servohydraulic test system to failure. The decrease in fatigue life caused by fretting damage was determined by comparing the stress-life (S-N) response of the fretted specimens to the S-N response of the virgin material, thus characterizing the severity of the fretting damage. The conditions that lead to the greatest reduction in life were identified in this way.

Using the fracture mechanics based NASGRO model, an Equivalent Initial Flaw Size (EIFS) was used to quantify the level of fretting damage, thus separating the life of the component into crack nucleation and subsequent propagation. This method and data will allow engineers to design more robust components that resist fretting damage, thus increasing the safety and reliability of the system.

CHAPTER 1

INTRODUCTION

Fretting occurs when two bodies in contact undergo low amplitude relative slip. Components damaged by fretting can exhibit a drastic reduction in fatigue performance due to the acceleration of fatigue crack nucleation. The extent of fretting damage is dependent on the material combination and is affected by many parameters, making it difficult to design against fretting. These parameters include the contact pressure, displacement amplitude, coefficient of friction (COF), temperature, geometry of contact, contacting materials and their properties, and surface treatments [1]. It is important to understand how each of these parameters affects the severity of fretting damage so that components can be designed to maximize fatigue life.

Austenitic stainless steels are the most used metallic materials in applications requiring corrosion resistance because of their high strength and ductility [2]. They are relatively soft in the annealed condition, but can be hardened substantially through cold work. The plastic deformation induces a transformation of the metastable austenite to martensite, which causes a considerable increase in strength [3]. This transformation has also been found to increase fatigue crack growth resistance by introducing a compressive residual stress at the crack tip [4-6]. The transformation also occurs during wear and alters the contact behavior, however whether the effect is beneficial depends on the conditions of the interaction [7].

AISI 301 stainless steel is the least alloyed of the chromium-nickel austenitic stainless steels (300 series). This results in lower austenite stability compared to the other

300 series alloys [6], and therefore demonstrates the positive effects associated with martensitic transformation to a greater extent, such as good formability [8]. Because of these characteristics, AISI 301 stainless steel sheet in full hard condition (cold rolled approximately 50%) has been used in many applications, including for springs and clamping devices such as multilayer gaskets [9].

Of the fretting studies on austenitic stainless steels reported in the literature, all were in the annealed condition [10-18]. Austenitic stainless steels in the annealed condition have been found to demonstrate a 15 to 30% reduction in fatigue strength due to fretting [14, 16]. However, no reported research was located in the open literature on fretting behavior of AISI 301 in the higher-strength cold-worked condition. Because the fatigue crack growth and wear behavior are quite sensitive to the hardness of the material, the fretting behavior of material in the cold rolled condition is expected to be much different compared to the annealed condition. Increased hardness is expected to improve the wear and high cycle fatigue properties but can be detrimental to the fretting fatigue and low cycle fatigue behavior.

The goal of this work is to investigate the fretting behavior of AISI 301 stainless steel sheets in full hard condition. An experimental method is developed to systematically investigate the fretting behavior of these thin specimens. The fretting damage is characterized in several ways. Fretting scars are inspected microscopically to gain knowledge about the wear behavior. Friction data logged during fretting experiments is analyzed to determine whether the running condition is partial slip, mixed slip, or gross slip [19]. The extent of the fretting damage is experimentally determined by finding the residual fatigue strength. This is done by cycling a specimen that was subjected to

fretting in a servohydraulic tests system until failure. Comparing this residual fatigue life to the fatigue life of the virgin material serves as a measure of the severity of fretting damage. A crack growth methodology is used to show that fretting damage is equivalent to a small crack, which can readily grow under bulk cyclic loading resulting in a large knockdown of the fatigue strength.

CHAPTER 2

BACKGROUND

2.1 Fretting

2.1.1 Damage Mechanisms and Characteristics

Fretting is a damage mechanism caused by two bodies in contact that are subjected to vibration or cyclic stress that causes low amplitude slip. Fretting is experienced across many industries, with failures occurring in aircraft, trains, automobiles, ships, and electrical contacts [20-22]. Depending on the materials, environment, and contact conditions, three forms of fretting can occur: fretting corrosion, fretting wear, and fretting fatigue.

The first reported study on fretting was performed in 1927 in regard to fretting corrosion by Tomlinson [23]. Fretting corrosion is the process of particle removal by contact and subsequent formation of oxides [24]. Materials such as stainless steel are resistant to corrosion because of the formation of a passivation layer. In the case of stainless steel, this passivation layer is composed of Cr_2O_3 [25]. When this passivation layer is removed by fretting, the exposed surface is susceptible to corrosion. Fretting corrosion is more severe when the frequency of motion is low, which allows more time for environmental interaction [24].

Fretting wear is characterized by the removal of surface material. In a 1985 survey, Sato [26] reported that the occurrence of fretting wear in machinery had not declined over previous decades, unlike other forms of wear. Wear can take place by abrasion, adhesion, or delamination. Abrasive wear is characterized by the formation of

hard granular wear debris, often referred to as third body particles. These third body particles can accelerate the removal of material when they have high hardness and irregular shape. Wear debris can also be smaller spherical particles. These fine third body particles can act as a solid lubricant, lowering the COF (the ratio of tangential force to normal force during gross slip) and decreasing the wear rate [27]. Adhesive wear takes place when local welding occurs between the two contacting bodies and the welds are broken during cycling. This removes large particles from the surface and results in large tangential forces. Tangential forces are higher for hard material pairs because of the increased force required to break welds. Adhesion is common between like materials because similar chemistry promotes welding. Adhesion is also more dominant in noble metals and in inert environments because surface oxides interfere with the local welding. High temperatures and forces promote adhesive wear because of the increased likelihood of welding [28]. Some materials that have been shown to exhibit adhesion include copper, austenitic stainless steel, and mild steel [29].

Delamination is caused when cracks are formed near the surface and run parallel to the surface. The cracking leads to removal of material which has a plate-like appearance. Suh's delamination theory [30] states that the subsurface microcracks are caused by the cyclic shear stresses caused by asperity contact on the surface. Cracks are not generated at the surface because of the high triaxiality of the stress state at the surface [31]. The depth of the microcracks is less when the COF is lower causing the plate-like debris to be thinner [32]. Titanium alloys have been found to wear primarily by delamination during fretting [28]. Figure 2.1 shows the appearance of wear caused by delamination on Ti-6Al-4V.

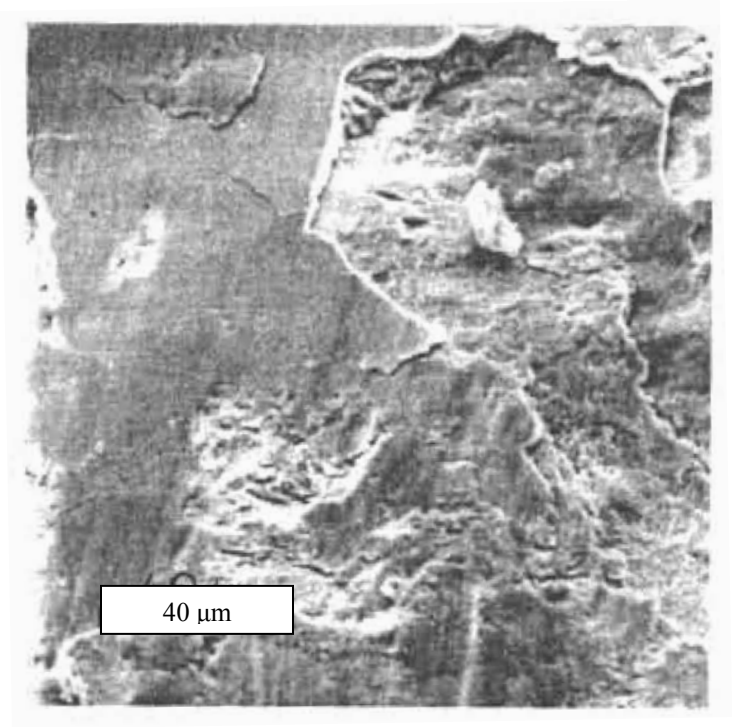

Figure 2.1: The plate-like appearance of wear of Ti-6Al-4V by delamination [28].

Fretting fatigue is a damage process caused by the interaction of fretting and fatigue. The fatigue process can be divided into crack nucleation and crack propagation. When a component subjected to fatigue loading also experiences fretting, the crack nucleation process is accelerated due to the cyclic stresses at contact. Cracks have been found to form due to fretting in the absence of bulk cyclic loading [33]. Therefore, several authors have proposed separating the fretting fatigue life of the component where initiation is controlled by fretting and subsequent long crack propagation or arrest is controlled solely by bulk stresses in thick specimens [34-38]. The initial growth of initiated cracks is determined by the stresses at contact. Cracks initially form at an angle between 35 and 55 degrees from the surface and propagate under shear (mode II) conditions due to shear from friction forces at contact. Once the crack has grown out of

the influence of the contact stresses, cracks turn to 90 degrees from the surface and growth is controlled by tensile (mode I) conditions due to bulk stresses [27].

The term knockdown refers to the decrease in fatigue performance due to fretting. A knockdown in fatigue life refers to the difference between the number of cycles to failure due to plain fatigue and the number of cycles to failure due to fretting fatigue for the same cyclic stress conditions divided by the plain fatigue life. A knockdown in fatigue strength refers to the difference between the cyclic stress level that results in a certain life of a component during plain fatigue and the cyclic stress level that results in the same life during fretting fatigue divided by the plain fatigue limit. The fatigue life reduction factor is the fretting fatigue life divided by the plain fatigue life. Similarly, the fatigue limit reduction factor is defined as the fretting fatigue limit divided by the plain fatigue limit.

The knockdown in the fatigue life due to fretting has been reported to be as high as 74% [39]. Cracks initiated during fretting are especially problematic because they are hidden by the contact itself, making visual inspection of components ineffective. In 1999, Nicholas [40] reported that “Fretting fatigue in dovetail joints is one of the most difficult and costliest problems in the US Air Force related to HCF”.

2.1.2 Influential Parameters

Fretting is a complex synergistic damage mechanism. As many as 50 parameters have been identified as influencing fretting. The primary parameters include the COF, contact pressure, and magnitude of slip [41].

Oxygen content and humidity of the atmosphere affect the oxidation behavior of the surface. The composition and quantity of oxides have a strong effect on the fretting behavior. High oxygen content and humidity increase oxidation. Fine oxides can act as lubrication which helps prevent adhesion, lowering stress due to friction. Alternatively, oxides can cause abrasive wear. Low oxygen and humidity decrease oxidation. The absence of oxides may result in adhesion, which increases friction and therefore the driving force for crack nucleation [1]. Temperature affects the material properties and the oxidation behavior. High temperatures can degrade material strength which can accelerate damage. However, a thicker glaze oxide can form at high temperatures which lowers the COF and increases the fretting fatigue life [17]. These effects vary greatly depending on material combination.

The contact condition during fretting is described by hysteresis loops; tangential force Q plotted versus displacement δ. The area inside the loop describes the amount of energy dissipated by frictional work. The two different types of contact conditions with their corresponding characteristic hysteresis loops are shown in Figure 2.2. Partial slip is the contact condition where a portion of the body is stuck and the edges of contact are experiencing slip. This is characterized by a narrow elliptical hysteresis loop. The amount of slip at the edge of contact increases as the tangential force increases and the hysteresis loop widens. When the ratio of tangential force to normal force rises above the COF, the entire interface experiences slip. This is known as gross slip, and is characterized by a wide hysteresis loop having a slope of nearly zero along the top and bottom portions of the loop. Reciprocating sliding occurs when the displacement amplitude is larger than the

contact half-width, so that the contact area at the peak displacement in one direction does not overlap the contact area at the peak displacement in the reverse direction.

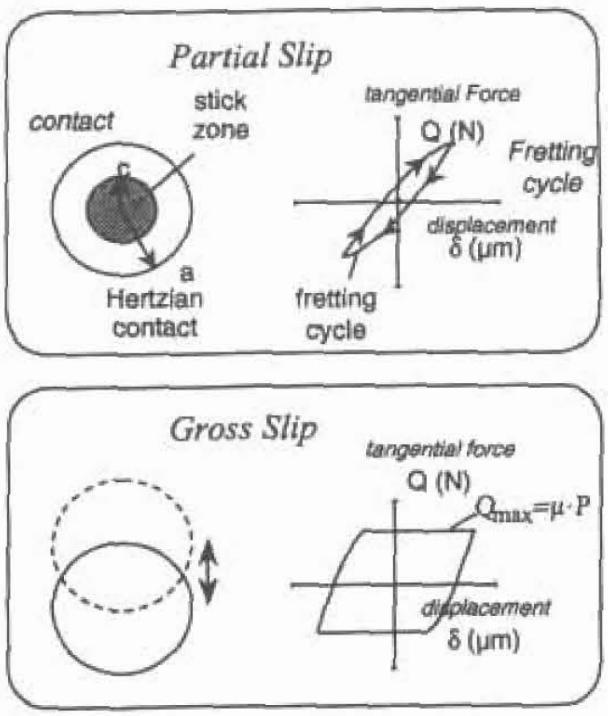

Figure 2.2: Illustration of partial slip and gross slip contact conditions showing the corresponding characteristic hysteresis loop [42].

During fretting, the contact conditions can change. A three dimensional plot of friction force versus displacement as a function of cycles, called a friction log, describes the change in contact condition as a function of cycles [43]. The running condition is divided into three different regimes: the Partial Slip Regime (PSR), Mixed Slip Regime (MSR), and Gross Slip Regime (GSR) [19]. These regimes make up the running condition fretting map shown in Figure 2.3 with the corresponding characteristic friction logs. The partial slip regime is distinguished by a partial slip contact condition for all cycles. The friction log for partial slip shows hysteresis loops that stay closed for all

cycles. The mixed slip regime (also known as the mixed fretting regime) is characterized by gross slip initially and a transition to partial slip as cycling continues. This can be seen in the friction log as open loops that transition to closed loops over the duration of cycling, typically because friction is increasing with cycles as fretting damage is generated at the interface. The gross slip regime is defined by gross slip conditions for all cycles.

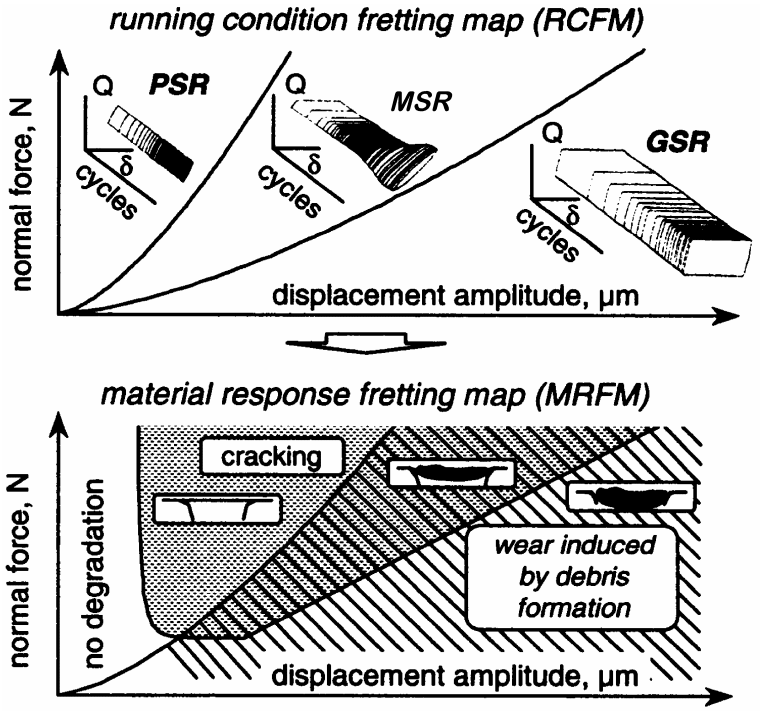

Figure 2.3: Running condition fretting map showing corresponding friction logs and material response fretting map showing corresponding damage mechanisms [42].

The relationship of the running condition fretting map to the material response, as shown in Figure 2.3, was first shown by Blanchard et al. in 1991 [44]. When the displacement amplitude is small, there is no damage. This is a very small value however, as damage has been observed at displacement amplitudes as low as 0.5 μm [45]. For

larger displacement amplitudes in the partial slip regime, cracking is the dominant damage mechanism, with little or no wear. The mixed slip regime demonstrates a combination of wear and cracking. In the gross slip regime wear is the prevailing damage process.

Figure 2.4 shows the general relationship between fatigue life and wear for the different running conditions as a function of displacement amplitude [19]. This is the expected behavior for a specimen that is thick relative to the wear depth. The largest knockdown in fatigue life due to fretting occurs near the transition between mixed slip and gross slip where both cracking and wear occur. At higher displacement amplitudes the increasing wear rate is responsible for reducing the knockdown in fatigue life. The wear rate becomes greater than the crack growth rate. Cracks are worn away, and therefore do not decrease the fatigue life [46-49]. In addition, the wearing of the surface changes the pressure distribution in a way that decreases the shear traction at the interface by spreading the pressure over a larger area [48, 50, 51].

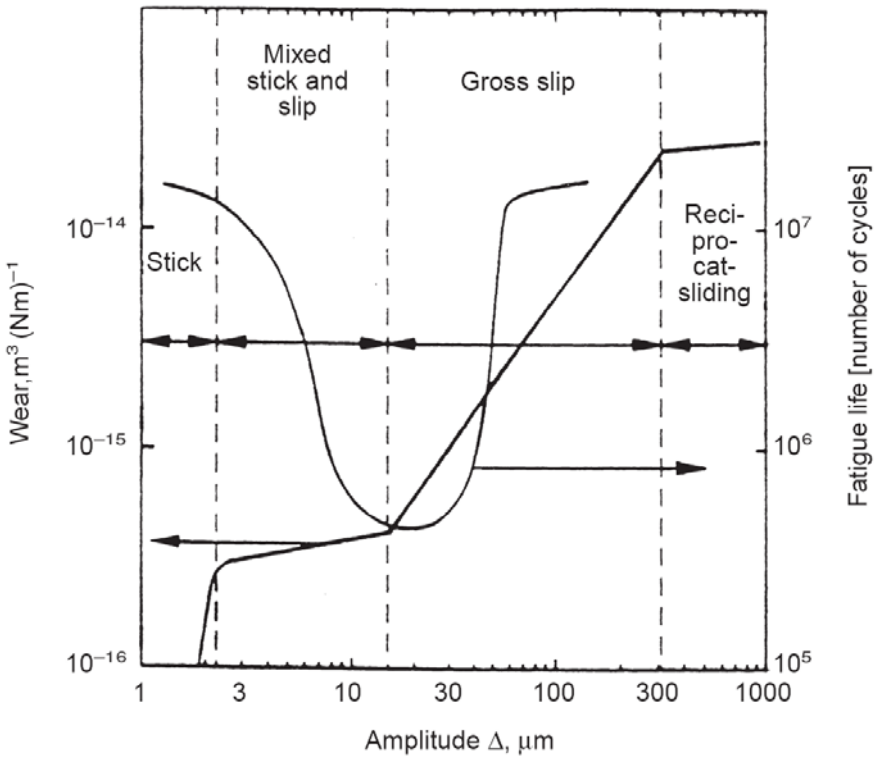

Figure 2.4: Relationship between fatigue life and wear for different running conditions as a function of displacement amplitude [19].

The classical solution of the shear tractions for perfectly smooth elastic cylinders in contact, derived by Mindlin [52] and Cattaneo [53], is shown in Figure 2.5. The global normal force P, the global friction force Q, and the COF μ determine the size of the stick region (-c to c) within the contact region (-a to a). Figure 2.5(b) shows how the shear traction within contact (q(x) normalized by the product of the COF μ and the Hertz peak normal pressure p_0) changes as a function of Q/μP. When Q is equal to μP (Q/μP = 1) the entire contact will be in slip and the shear traction has a parabolic shape, which is the same as the Hertz normal pressure distribution since q(x) = μp(x) where p(x) is the normal pressure distribution. When the interface remains in partial slip, |Q| is less than μP, and a region of stick occurs in the center of contact. The shear traction in the slip

region remains the same but decreases in the stick region. Therefore, the peak shear traction occurs at the boundary between stick and slip. As the tangential force decreases further, the boundary between stick and slip, and therefore the maximum shear traction, shifts closer to the edge of contact.

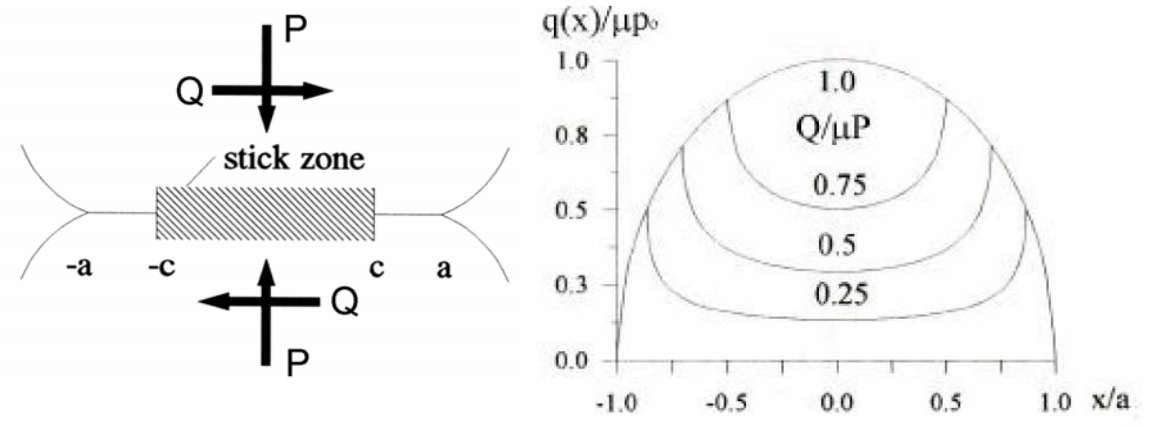

(a) (b)

Figure 2.5: (a) Schematic of the stick and slip regions during partial slip, and (b) shear stress distribution for partial slip conditions [54].

During fretting the friction force varies sinusoidally as shown in Figure 2.6(a). Here, the shear tractions along the interface also vary with time as shown in Figure 2.6(b). The hash marks in this figure represent the region of stick. At the peak tangential force, at point A in the cycle, the traction is as described above. Upon instantaneous unloading (point B), the shear reduces infinitesimally and the stick region expands to cover the entire contact. As Q is reduced (point C), reverse slip occurs near the edges of contact. This is because the normal pressure at the edge of contact is too low to prevent slip. At point D, the global friction force is zero and so the local tractions over the contact area must sum to zero to maintain equilibrium. Reversing Q to $-Q_{max}$ (point E) results in a shear state equal to that at point A but in the reverse direction.

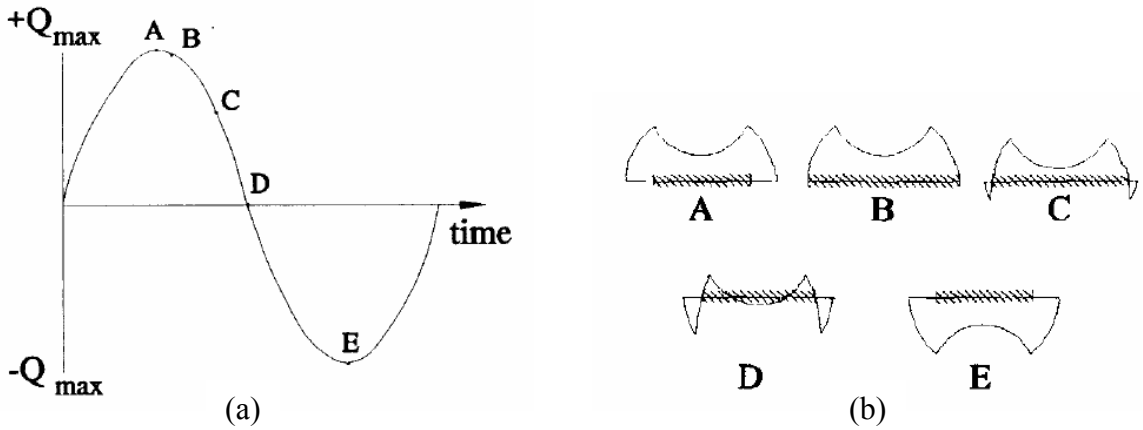

Figure 2.6: (a) Friction force history and (b) corresponding local shear tractions during fretting [54].

The location of crack formation from fretting during gross slip can occur anywhere in the scar from the interactions of asperities or microstructural inhomogeneities. The location of crack formation in partial slip often occurs in the microslip region near the boundary of stick and slip [27] because of the peak in shear stress at that location.

The location of greatest fretting damage has been proposed by Ruiz et al. [55] to occur at the location of maximum energy dissipation per area due to fictional work. The Fretting Damage Parameter (FDP) was suggested to determine the level of fretting damage at different points along the interface,

$$FDP = \tau\delta \tag{2.1}$$

where τ is the maximum shear traction attained during one cycle at a point and δ is the relative amplitude of slip between the surfaces at the same point. The location with the

maximum value of the FDP will be the most damaged. In regions of stick $\delta = 0$, and so there will be no damage.

Ruiz et al. also recognized that cracks are more likely to form in areas that have a bulk tensile stress. Therefore, they proposed that the probability of crack formation at a location may correlate to the product of maximum frictional work per area and the maximum value of the normal stress parallel to the surface during a cycle, called the Fretting Fatigue Damage Parameter,

$$FFDP = \sigma(\tau\delta) \tag{2.2}$$

where σ is the maximum normal stress parallel to the surface during one cycle, i.e., the tangential stress, during one cycle. The tangential stress distribution during fretting fatigue has been shown by Nowell and Hills [56]. The peak value of the FFDP has been found to correlate well with the location of fretting fatigue crack initiation and its magnitude can correlate to the number of cycles to crack formation [55, 57-60].

2.2 Austenitic Stainless Steel

Bermo Strauss and Edward Maurer developed the austenitic Fe-Cr-Ni alloys in Krupp Laboratories in Germany from 1909 to 1912. Strauss et al. later developed steels which led to the 18-8 series of stainless steels (the 300 series) [61].

Austenitic stainless steels are the most used metallic materials in applications requiring corrosion resistance because of their high strength and ductility [2]. In the cold worked condition they have been used as clamps and springs including head gaskets in automobiles [9]. They are relatively soft in the annealed condition where the composition

is fully austenitic, but can be hardened substantially through cold work due to a transformation from austenite to martensite [3]. The yield strength of AISI 301 in the annealed condition is 275 MPa, but ultimate strengths as high as 1900 MPa can be obtained by cold work [62]. Ductility is very high in the annealed condition, with a minimum elongation to failure for 301 specified by ASTM A 666-03 of 40%. Intermediate amounts of cold work can alter the material properties to suit a variety of applications.

Austenitic stainless steels belong to the category of steels known as Transformation Induced Plasticity (TRIP) steels [63]. More specifically, austenitic stainless steels belong to one of two categories called H-TRIP steels, which are classified by high Ni and Cr contents that results in a structure consisting of metastable austenite at room temperature. The other category, L-TRIP steels, contains less alloying and consists of a ferritic-bainitic matrix with 10-15% retained austenite [64-66]. The austenite in TRIP steels undergoes a deformation induced transformation to martensite [67]. The transformation in H-TRIP steels is strain-induced while the transformation in L-TRIP steels is stress-assisted at room temperature. The TRIP effect provides a considerable enhancement of ductility and toughness [68].

Austenitic stainless steels have excellent resistance to corrosion because of the formation of a passivation layer. This passivation layer is composed of a chemically resistant chromium oxide film that protects the substrate from chemical attack. Type 301 has on oxide film composed of as much as 90% Cr_2O_3 [25]. This film is very thin, with a typical thickness of between 1 and 10 nm in air at room temperature [69, 70]. This layer can be removed easily by abrasion, and will readily reform.

The compositions of the austenitic stainless steels as specified by ASTM A 666-03 are shown in Table 2.1. Types with an L designation have lower carbon content and types with an LN designation have reduced carbon and nitrogen content for better weldability. The 200 series have lower nickel content than the 300 series, making them less temperature resistant and less expensive. Manganese is added to maintain the austenite stability lost by removing nickel. Type 301 is the least alloyed of the 300 series, resulting in the lowest austenite stability and stacking fault energy [71].

Table 2.1: Composition of austenitic stainless steels specified by ASTM A 666-03.

Type	UNS Designation	Composition, %[B]							
		Carbon	Manganese	Phosphorus	Sulfur	Silicon	Chromium	Nickel	Other Elements
201	S20100	0.15	5.5–7.5	0.060	0.030	0.75	16.0–18.0	3.5–5.5	N 0.25
201L	S20103	0.03	5.5–7.5	0.045	0.030	0.75	16.0–18.0	3.5–5.5	N 0.25
201LN	S20153	0.03	6.4–7.5	0.045	0.015	0.75	16.0–17.5	4.0–5.0	N 0.10–0.25 Cu 1.00
202	S20200	0.15	7.5–10.0	0.060	0.030	0.75	17.0–19.0	4.0–6.0	N 0.25
. . .	S20400	0.030	7.0–9.0	0.040	0.030	1.00	15.0–17.0	1.50–3.00	N 0.15–0.30
205	S20500	0.12–0.25	14.0–15.0	0.060	0.030	0.75	16.5–18.0	1.00–1.75	N 0.32–0.40
301	S30100	0.15	2.00	0.045	0.030	1.00	16.0–18.0	6.0–8.0	N 0.10
301L	S30103	0.03	2.00	0.045	0.030	1.00	16.0–18.0	6.0–8.0	N 0.20
301LN	S30153	0.03	2.00	0.045	0.030	1.00	16.0–18.0	6.0–8.0	N 0.07–0.20
302	S30200	0.15	2.00	0.045	0.030	0.75	17.0–19.0	8.0–10.0	
304	S30400	0.08	2.00	0.045	0.030	0.75	18.0–20.0	8.0–10.5	N 0.10
304L	S30403	0.030	2.00	0.045	0.030	0.75	18.0–20.0	8.0–12.0	N 0.10
304N	S30451	0.08	2.00	0.045	0.030	0.75	18.0–20.0	8.0–10.5	N 0.10–0.16
304LN	S30453	0.030	2.00	0.045	0.030	0.75	18.0–20.0	8.0–12.0	N 0.10–0.16
316	S31600	0.08	2.00	0.045	0.030	0.75	16.0–18.0	10.0–14.0	Mo 2.00–3.00
316L	S31603	0.030	2.00	0.045	0.030	0.75	16.0–18.0	10.0–14.0	Mo 2.00–3.00
316N	S31651	0.08	2.00	0.045	0.030	0.75	16.0–18.0	10.0–14.0	Mo 2.00–3.00

The phase of 300 series stainless steel depends on the temperature. Three temperatures define the possible composition and transformation mechanisms: $M_f < M_s < M_d$. The values of M_s and M_d for 301 are approximately -100^{o}C and 100^{o}C [5]. Above M_s (including room temperature), austenitic stainless steels are composed of a Face Centered Cubic (FCC) γ austenite phase, hence, why these are called austenitic stainless steels. Below M_s, austenite begins to spontaneously transform to martensite by thermally assisted transformation. Below M_f, all austenite has transformed to martensite. Between

M_s and M_d, austenite is metastable and can transform to martensite by a strain-induced transformation mechanism Between M_s and M_f, a stress-assisted transformation to martensite can take place.

There are two common second-phase constituents found in austenitic stainless steels. The most commonly observed carbides have the composition $M_{23}C_6$ shown in Figure 2.7(a) [71, 72]. $M_{23}C_6$ has reported compositions of $(Cr_{16}Fe_5Mo_2)C_6$, $(Cr_{17}Fe_{4.5}Mo_{1.5})C_6$, and $(Fe,Cr)_{23}C_6$ [72]. Fewer carbides are present in the L and LN grades because of the reduced carbon content. However, the L and LN grades are more likely to contain the other common constituent, δ-ferrite. δ-ferrite is brittle, and often forms in stringers as shown in Figure 2.7(b) [72].

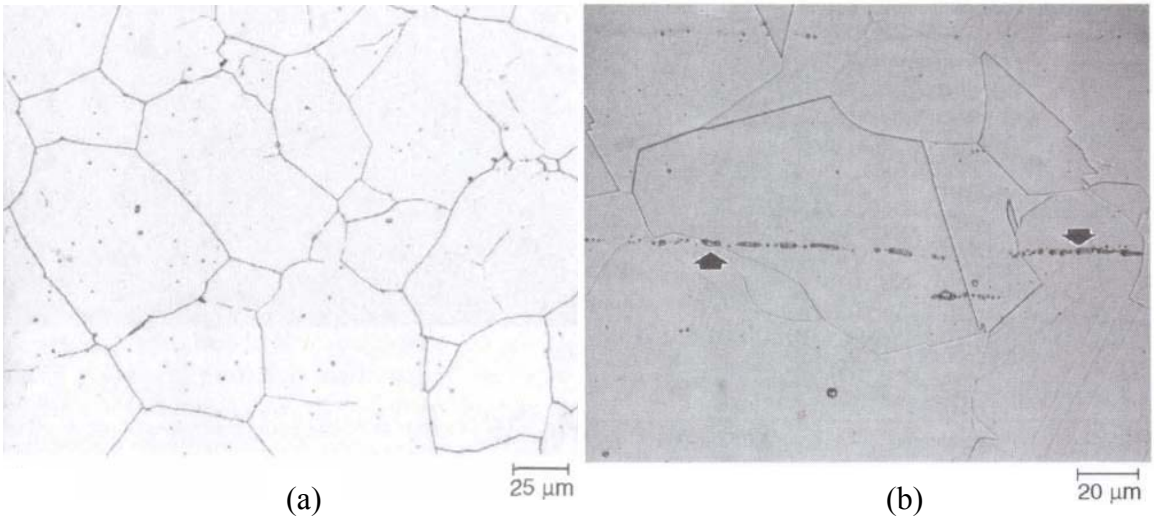

(a) (b)

Figure 2.7: (a) $M_{23}C_6$ carbides in annealed 304 and (b) δ-ferrite stringer in annealed 302 [72].

The austenite undergoes a deformation-induced transformation to either a Body Centered Cubic (BCC) α' plate martensite, or a fine, lathlike Hexagonal Close Packed (HCP) ε martensite [3]. The deformation induced transformation can be either stress-

assisted or strain-induced. Stress-assisted transformation occurs when an increase in stress is the only additional driving force required for the transformation and generally occurs at the M_s temperature and below. This results in formation of BCC martensite. Strain-induced martensite forms as a result of development of nucleation sites for transformation from cold work when between the M_s and M_d temperatures [73]. An example of the appearance of martensite due to cold work in type 303 is shown in Figure 2.8.

Figure 2.8: Martensite formed by cold rolling (arrows) in type 303 etched with waterless Kalling's reagent [72].

The extent of the transformation depends on the stability of the austenite. The stability is dependent on the composition and temperature. Increasing the amount of

alloying increases the stability of the austenite [74]. Type 301 is the lowest alloyed member of the 300 series, and therefore has the lowest stability [6]. Stability also increases with increasing temperature.

Austenite is paramagnetic, and BCC martensite is ferromagnetic. Ferromagnetic materials respond to a magnetic field, and retain their own field once removed from the externally applied field. Paramagnetic materials also respond to a magnetic field, but do not sustain their own. Therefore, the amount of BCC martensite present can be detected by magnetic testing equipment such as a ferrite scope, Vibrating Sample Magnetometer (VSM), Giant Magneto-Resistance sensor (GMR), or Superconducting Quantum Interference Device (SQUID) [75]. Magnetic Force Microscopy (MFM), which is a variant of Atomic Force Microscopy (AFM) where a magnetic tip is used to measure forces, is another option for detection of martensite with high special resolution (better than 50 nm) [76]. The HCP martensite phase is not magnetic, and is therefore requires Transmission Electron Microscopy (TEM) and X-ray diffraction (XRD) to detect.

Because the transformation takes place during deformation, cold worked materials can contain a substantial amount of martensite. Figure 2.9 shows the BCC martensite content and mechanical properties as a function of percent cold work for type 301. The martensite is stronger but more brittle than austenite. Therefore, increasing martensite increases strength but reduces ductility.

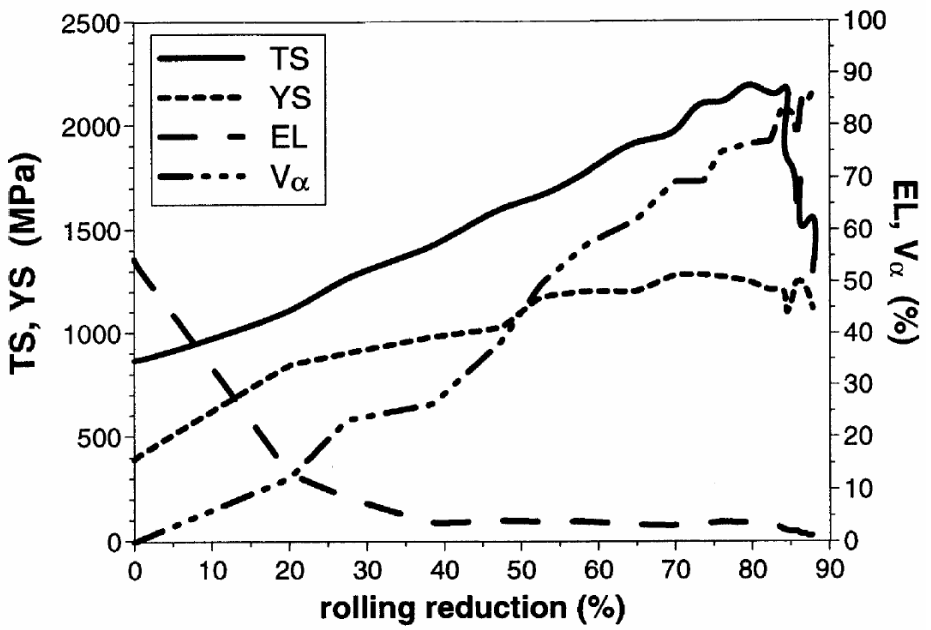

Figure 2.9: Mechanical properties and BCC martensite content as a function of the rolling reduction for 301 stainless steel [77].

Figure 2.10 shows the sensitivity of martensite stability on temperature. Talyan et al. [8] conducted tensile tests on type 301 while measuring temperature rise of the sample due to deformation as well as martensite content for three strain rates. At low strain rates, the deformation induced heating was low and a large amount of martensite formed. At higher strain rates, deformation induced heating caused a larger temperature rise which inhibited transformation. As a result, the ultimate strength fell from 980 MPa to 720 MPa. The effect was proven to be temperature driven by performing high strain rate tests in room temperature water. The increased convection reduced the temperature increase due to deformation and the strain rate effect was reduced.

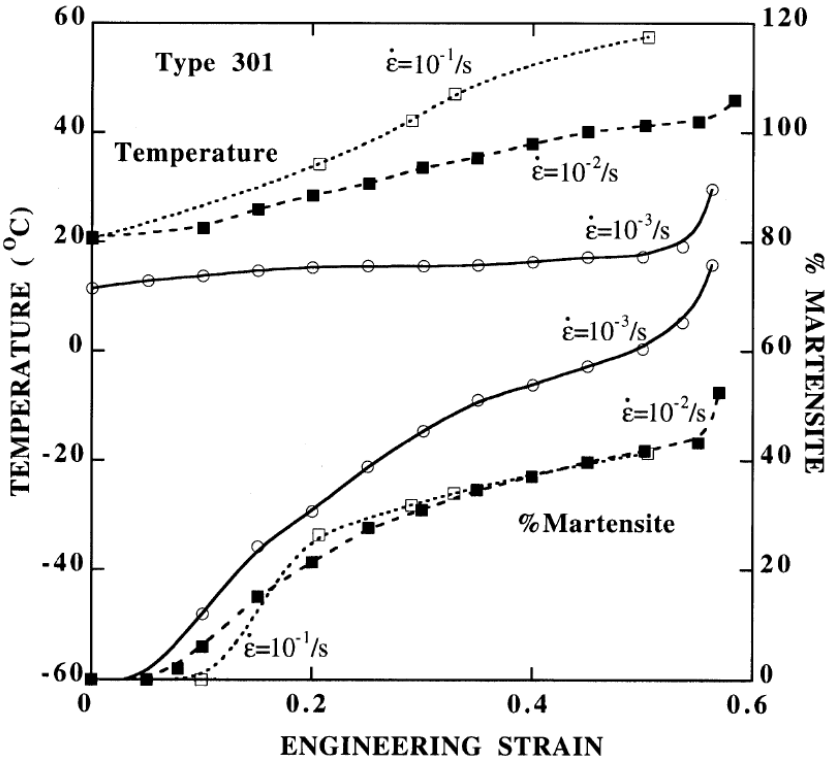

Figure 2.10: Effect of strain rate on the temperature rise and martensite transformation in 301 stainless steel [8].

Figure 2.11 shows the extent of cyclic hardening resulting from cyclic stress-strain at four temperatures within the M_s to M_d range [78]. At lower temperatures, much more cyclic hardening takes place due to the lower stability of austenite. As temperature increases, the cyclic hardening decreases because less transformation to martensite occurs. This demonstrates the sensitivity of behavior on temperature relating to the effect of phase transformation.

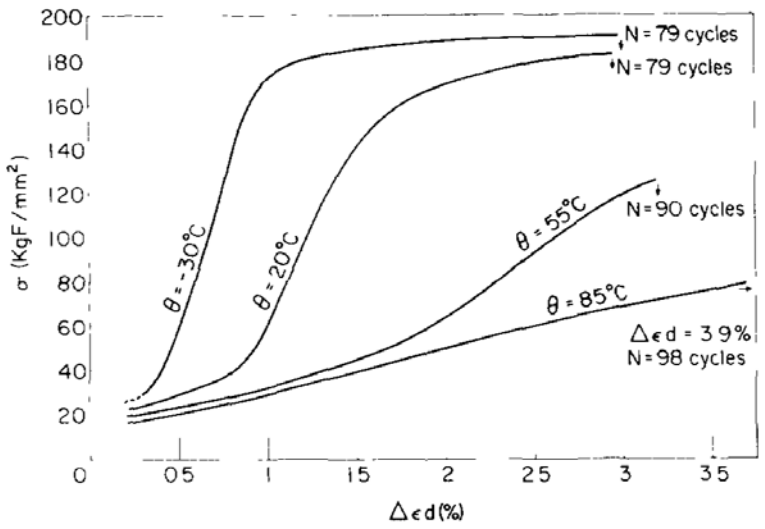

Figure 2.11: Cyclic stress-strain curves for type 301 at four temperatures between M_s and M_d indicating cycles to failure, N [78].

Barclay et al. [79] examined the deformation mechanisms austenitic stainless steel by TEM and XRD. The following six mechanisms were found to taking place during tensile deformation: (1) dislocation motion in austenite, (2) dislocation tangles, cell formation, and formation of stacking faults in austenite, (3) deformation twins in austenite, (4) martensite formation, (5) dislocation motion in martensite, and (6) deformation twins in martensite. These mechanisms were observed to take place in this order, with overlap by as many as three mechanisms.

The lower alloyed austenitic stainless steels have very low stacking fault energies. Values range from less than 15 mJ/m^2 for type 301 to 90 mJ/m^2 for type 316. Therefore, lower alloyed austenitic stainless steels primarily deform planar dislocation glide. Cross slip of dislocations is impeded and therefore the dislocation motion is restricted to the corresponding slip plane. This limits the formation of 3D dislocation arrangements such as cell structures [80].

An optimal austenite stability exists where the transformation to martensite occurs at an intermediate level of plastic strain to maximize strength and elongation. If the transformation occurs to readily, the material becomes brittle [3, 8, 14]. If the austenite is too stable, excessive dislocation generation and twinning in the austenite occurs causing fracture in the austenite before a transformation takes place [79]. It is difficult to obtain the optimal stability because of the high sensitivity to composition and temperature [3], however type 301 with 7% Ni is said to be close to optimum at room temperature [79].

The transformation to martensite has a significant effect on the fatigue crack growth behavior. At low mean stresses in annealed material, unstable austenite has a lower fatigue crack growth rate than stable austenite. This is due to a positive volume change associated with the transformation. The lower density of martensite causes the introduction of compressive stresses from transformation when the volume is constrained. Compressive stresses are introduced in the plastic zone surrounding the crack tip where transformation occurs. This lowers the mean stress and therefore reduces the driving force for crack growth [6]. However, the high hardening due to the transformation tends to increase the crack growth rate because of reduction in the resistance to crack growth due to the brittle nature of the martensite phase. This effect offsets the beneficial reduction in mean stress when tests are conducted with high mean stress [4]. Stress amplitude has been found to increase due to the secondary cyclic hardening when tests are conducted in strain control [78, 81, 82]. Hardening increases at decreased temperature because of the decreased austenite stability. In highly cold worked material the fatigue crack growth resistance is higher than in the annealed condition by a factor of 2 to 3 and is not dependent on the stability of the austenite [6]. Separate work

has reported the fatigue crack growth resistance is lower for highly cold worked material when ΔK is less than 44 MPa $\sqrt{m}$ [5].

Formation of fretting cracks occurs in a volume of material experiencing a multiaxial state of cyclic stress and strain [60]. Hence, the crack formation under multiaxial loading is relevant. The cracking behavior exhibited by annealed type 304 when tested in tension or torsion is shown in Figure 2.12. The life of the material is divided into three regions. Region A is a failure mode dominated by shear crack growth. Region B is shear crack nucleation followed by crack growth on planes of maximum principal strain (stage II growth planes). Region C is life dominated by crack nucleation. In torsion, region A behavior was observed for short lives while region B behavior was exhibited for long lives. Region C was only observed for the longest lives. When tested in tension, the fracture surface was dominated by stage II growth [83]. At low strain amplitudes up to 90% of the life is taken up by nucleation, while at high strain amplitudes 90% may be stage II growth [84]. Fretting cyclic stresses cracks early in the life, which suggests that shear crack growth might be important. Thin specimens, which have less constraint, will tend to be shear cracking.

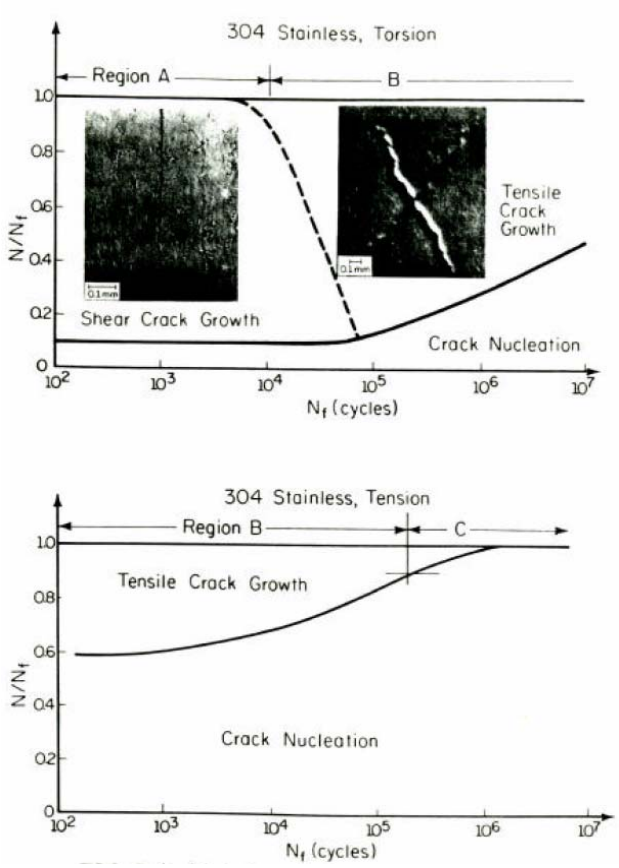

Figure 2.12: Cracking behavior of annealed type 304 in torsion and in tension [83].

During high cycle fatigue of annealed types 301, 304, and 310 cracks were found to initiate in a slip band near a grain or twin boundary [85]. Cracking at inclusions was not found. Cracks that caused failure were typically microcracks that coalesced to form the catastrophic flaw. Typical microcracks were measured to be approximately 25 μm after slow growth before linking with other cracks by fracture of the intermediate material. In cold worked material, cracks were initiated at cracked inclusions and microcrack linking did not play a role [85].

It is well known that austenitic stainless steels have poor wear and galling resistance. Macro welding can occur, which increases surface damage [29]. Materials with low stacking fault energies typically have lower crack nucleation rates, which can

decrease the tendency for delamination [86]. The transformation to martensite also occurs during wear and alters the contact behavior, however whether the effect is beneficial depends on the conditions of the interaction. The transformation hardens the surface layer, which is then supported by a softer layer. This can lead to cracking of the surface layer at the interface between the hard and soft layer where subsequent deformation tends to be more intense and can lead to an increased wear rate [7]. There are many competing mechanisms which make the wear behavior complex.

2.3 Fretting of Austenitic Stainless Steel

Many fretting studies have been carried out on austenitic stainless steel because of its widespread use and the serious effects of fretting. Fretting tests have been conducted in a variety of environments including H_2 [87], CO_2 [17], vacuum [12, 88], and simulated body fluids [10, 11, 89, 90]. Elevated temperatures tests up to 650^{o}C have been performed. However, no reported research was found on austenitic stainless steel in the cold-rolled condition.

Hsu et al. [7] studied the effect of the martensitic transformation on the fretting wear behavior. They reported an increase in the wear rate as the stability of the austenite decreased because of the composition of the oxide. Type 304 produced a fine BCC α' martensite wear debris, whereas type 316 (higher stability) had a larger plate like α' debris that had a more damaging effect on the surface. Using TEM, Hsu observed that the subsurface composition of 304 transformed to the structure shown in Figure 2.13. The thickness of the layers will vary with test conditions, but was not discussed.

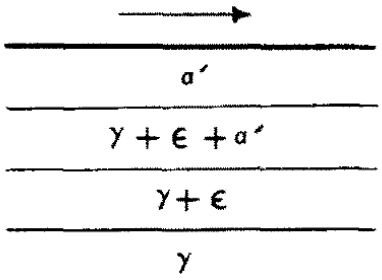

Figure 2.13: Surface composition as a function of depth resulting from sliding wear of 304 with an arrow indicating the direction of sliding [7].

The effect of grain size on the fretting fatigue behavior of 304 was studied by Raman and Jayaprakash [14]. For the two grain sizes studied (47 μm and 277 μm) the COF was found to be higher for the fine grained material by approximately 20%. The presence of martensite in the fretting scars was documented for the two grain sizes studied and was found to have a very inhomogeneous distribution. More martensite was found in the course grained material as shown in Figure 2.14 as a result of the larger quantity of annealing twins. The martensite was measured with a ferrite scope, and so the quantity of martensite was reported in terms of ferrite number. More martensite was found in fretting scars due to the increased stresses from contact. Less martensite was found in the bulk of the specimens when subjected to fretting fatigue compared to plain fatigue because of the shorter life in fretting fatigue. The fretting fatigue life of the fine grained material was found to be 50% lower than the plain fatigue life, whereas the coarse grained material showed almost no reduction. This is due to the higher COF for the fine grained material and the increased crack growth resistance from the higher martensite content in the coarse grained material.

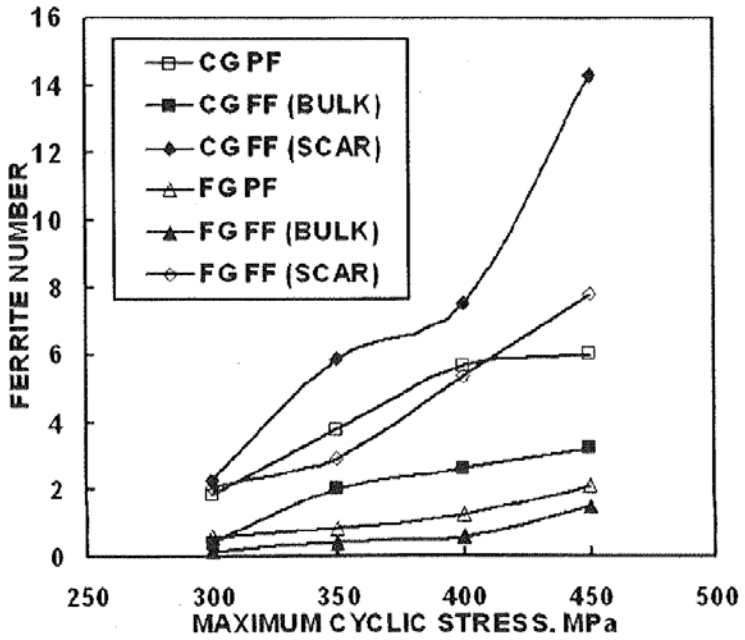

Figure 2.14: Presence of martensite in course grained (CG) and Fine Grained (FG) 304 resulting from Fretting Fatigue (FF) or Plain Fatigue (PF) [14].

Nakazawa et al. [16] investigated the effect of contact pressure on the fretting fatigue life of 316L. At a stress amplitudes of 150 MPa, the fretting fatigue life using a 60 MPa contact pressure was one third of the fretting fatigue life using a 30 MPa contact pressure, as shown in Figure 2.15. However, the stress amplitude resulting in infinite life was the same for both pressures. The reduction in fatigue strength due to fretting was found to be 30% with a 30 or 60 MPa contact pressure. Increasing pressure caused the catastrophic crack to form more toward the edge of the scar due to the increased stick region. Hence, cracks initiated at the boundary between stick and slip.

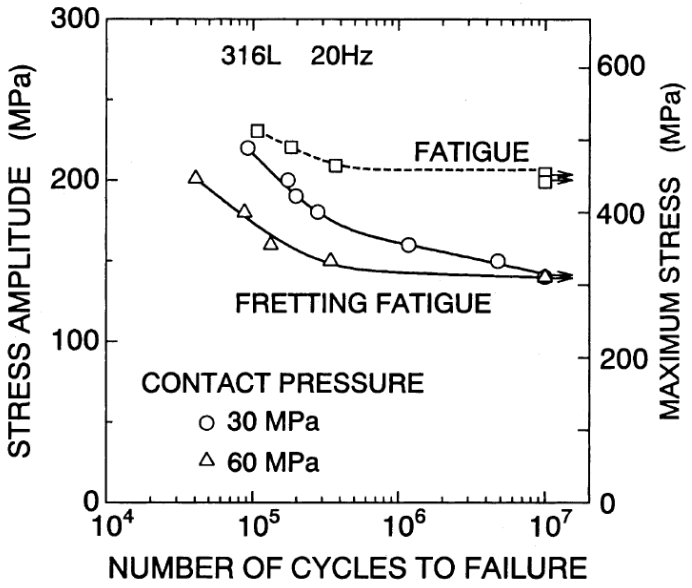

Figure 2.15: Influence of contact pressure on the fretting fatigue life of 316L [16].

In an investigation of the fretting wear of type 304 in a vacuum, Iwabuchi et al. [12] found the formation of cracks in the high slip portion of the mixed slip regime and at the lower slip portion of the gross slip regime. In the mixed slip regime a high number of small cracks were found to form. In the gross slip regime the cracks had linked so that fewer but larger cracks were present. Cracks were not created during tests in air with the same contact conditions. This was due to the oxide formation and the resulting increase in wear. The oxides formed during testing in air were removed easily from the surface, increasing the wear rate. This increased the conformity of contact, which lowers the contact stress. The oxides also decreased the stress due to friction by acting as a lubricant. The beneficial effect of the oxide was also noted by other authors [13, 91].

The composition of the iron oxide formed by type 304 during fretting was found to be Fe_2O_3 from room temperature until 300^{o}C where it changed composition to Fe_3O_4. At higher temperatures, adhesion was promoted causing transfer of material between the

contacting bodies. The amount of material transferred was also dependent on the frequency. A frequency of 16.6 Hz was found to cause twice the material transfer compared to 1.2 Hz [13]. This may be a result of the temperature rise of the material due to frictional dissipation, which would cause an increase in adhesion. Increasing temperature has also been found to cause the formation of glaze oxides in type 304, which reduce friction and wear [17, 87, 91].

Several studies have been performed in corrosive fluids, including fretting of type 316 in pseudo body fluid [10, 11, 89] and type 304 in NaCl [90]. It was found that the NaCl reduced the wear rate of 304 because of lubrication and convective heat transfer. The cooling promoted transformation to hard martensite, which therefore reduced wear. The increased oxidation in NaCl reduced the COF by eliminating adhesion that was observed during sliding in air [90]. At lower loads, delamination was found to be the dominant wear mechanism.

Because the fatigue crack growth and wear behavior are quite sensitive to the hardness of the material, the fretting behavior is expected to be much different for the cold rolled condition compared to the annealed condition. Increased hardness typically improves the wear and high cycle fatigue properties but can be detrimental to low cycle fatigue behavior, which has been related to fretting crack formation [60].

CHAPTER 3

BASELINE MATERIAL STRUCTURE AND PROPERTIES

Before studying the fretting behavior, the basic structure and properties of AISI 301 stainless steel were determined. This included microstructural characterization by etching and mechanical property investigation via tensile, fatigue, and fatigue crack growth testing.

3.1 Microstructural Characterization

3.1.1 Procedure

The microstructure was examined by mechanically polishing samples and exposing them to several different etchants. These etched samples were then examined using optical microscopy to determine grain size, inclusion size and abundance, as well as phase distributions.

Samples were mounted using Struers Epoes cold mount epoxy. Epoes has a cure time of approximately 12 hours, but has better adhesion and lower shrinkage than faster curing acrylics and epoxies. Mounted samples were polished with a Struers RotoPol-15 automatic polisher using the procedure in Table 3.1. Polishing solutions from Struers were used. Particle type and size for each solution are noted in Table 3.1. Samples were cleaned using ethanol in an ultrasonic cleaner between steps to remove abrasive particles that could cause scratching in subsequent steps. Ethanol was used for cleaning rather than water to prevent oxidation.

Table 3.1: Polishing procedure.

Disc	Solution	RPM	Force (N)	Time (min)
P800 SiC paper	Water	300	20	variable
MD-Allegro	DiaPro Allegro - Largo (9 µm diamond)	150	15	8
MD-Dac	DiaPro Dac (3 µm diamond)	150	15	4
MD-Chem	OP-A (0.02 µm alumina)	150	10	2

Polished samples were etched using three solutions commonly used for 300 series stainless steel. The solutions were chosen from ASTM E 407-99: Standard Practice for Microetching Metals and Alloys. The three solutions selected are shown in Table 3.2. These etchants were chosen based on availability and relative safety (absence of perchloric and hydrofluoric acids). Kalling's No. 2 exposes carbides, attacks austenite slightly, and darkens martensitic phases. Glyceregia also exposes carbides, with less ability to expose other phases. The electrolytic etching in 10% oxalic acid solution exposes grain boundaries and attacks austenite more rapidly, therefore also exposing martensite phases [72]. Exposure time was varied to expose different features, while chemistry and voltage were kept constant.

Table 3.2: Etchants used from ASTM E 407-99.

Etchant name	Solution	Procedure
Kalling's No. 2	5 g CuCl2, 100 mL HCl 100 mL ethanol	Swab 1 minute
Glyceregia	3 parts HCl, 2 parts glycerol 1 part HNO3	Swab 30 seconds
!0% oxalic acid	10 g oxalic acid 100 ml water	Electrolytic at 6 V 15-30 s for carbides 1 minute for grain boundaries and martensite

3.1.2 Results

Poor results were obtained when etching with Kalling's No. 2 and with Glyceregia. Kalling's No. 2 darkened the entire surface and did not expose any distinguishable features, even for short swabbing times. Glyceregia also did not expose any distinguishable features.

Figure 3.1 shows the results of electrolytic etching the face of a sheet of 301 with a 10% oxalic acid solution with 6 volts for 1 minute. Arrows point to martensite and several inclusions are circled. Martensite appears as short dark lines while austenite remains light [72]. The grain size was measured to be approximately 30 μm. Inclusions are approximately 10 μm and are expected to be $M_{23}C_6$ [71].

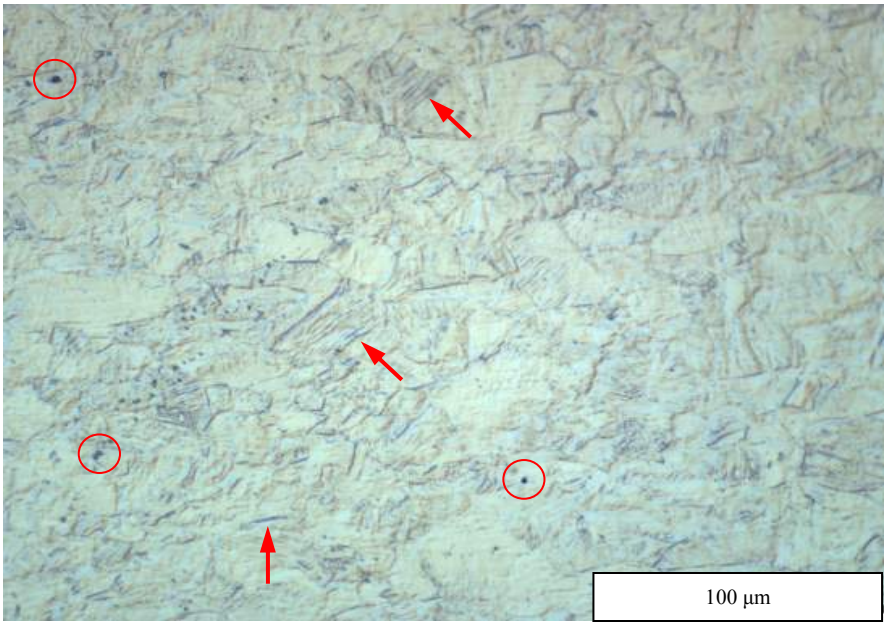

Figure 3.1: Face of a 301 sheet etched with a 10% oxalic acid solution at 6 volts for 1 minute showing martensite (arrows) and inclusions (circled).

The edge of a sheet electrolytically etched with 10% oxalic acid with 6 volts for 1 minute is shown in Figure 3.2. The vertical rolling direction is evident by the elongated structure. Several δ-ferrite stringers were observed when examining edges of the sheets. These δ-ferrite stringers are brittle [72], and are therefore a likely location for crack formation.

Figure 3.2: The edge of a 301 sheet etched with 10% oxalic acid with 6 volts for 1 minute showing longitudinal structure and a δ-ferrite stringer (arrow).

3.2 Tensile Testing

3.2.1 Procedure

Tensile tests were performed at Georgia Tech on the servohydraulic test system shown in Figure 3.3. The control system used is MTS TestStar IIs.

Specimens were fabricated using a laser cutter to have the dimensions shown in Figure 3.4. The faces of the specimens were left in the as-rolled condition, with values of the average and maximum roughness of 0.10 μm and 0.78 μm respectively. Edges were polished longitudinally with SiC paper to a maximum surface roughness R_y of 0.2 μm.

Figure 3.3: Test system used for tensile testing.

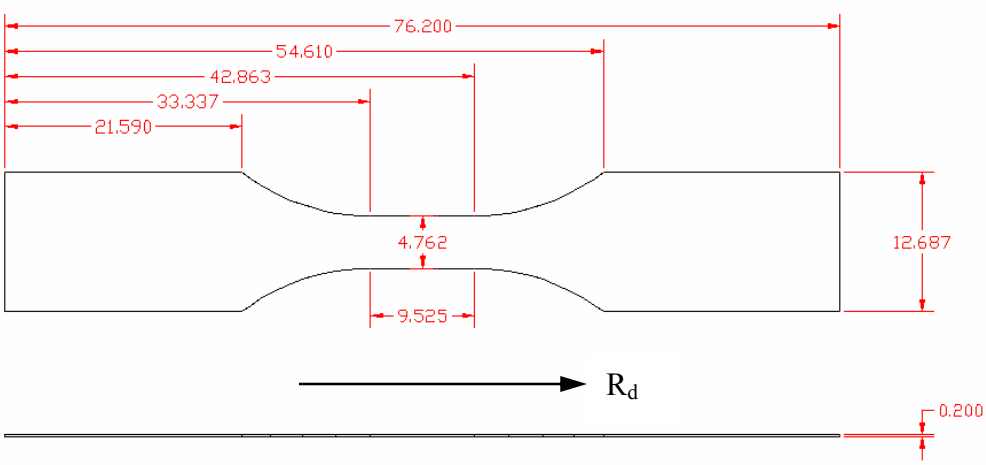

Figure 3.4: Dogbone specimen with an arrow indicating the rolling direction, R_d, with dimensions in millimeters.

Specimens were clamped using mechanical grips. A clip-on knife-edge extensometer with a gage length 8 mm of was used. Alignment of the specimen in the grips was critical. Specimens that were poorly aligned exhibited a drastically reduced elongation to failure as shown in Figure 3.5. A multiple step process was used to ensure proper alignment, represented in Figure 3.6. First, the specimen was inserted into the bottom grip with bar 1 and bar 2 in position. Bar 1 forces the angle between the specimen and the grip to be square and bar 2 sets the distance between the edge of the specimen and the edge of the grip. After tightening the bottom grip screws, bar 3 was introduced to ensure the top and bottom grips were parallel while the top grip screws were tightened.

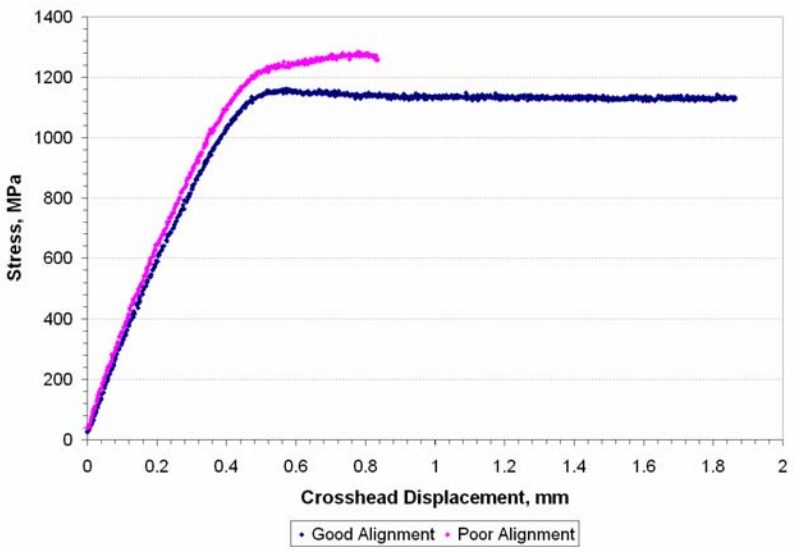

Figure 3.5: Stress-strain curve of a poorly aligned specimen and a well aligned specimen.

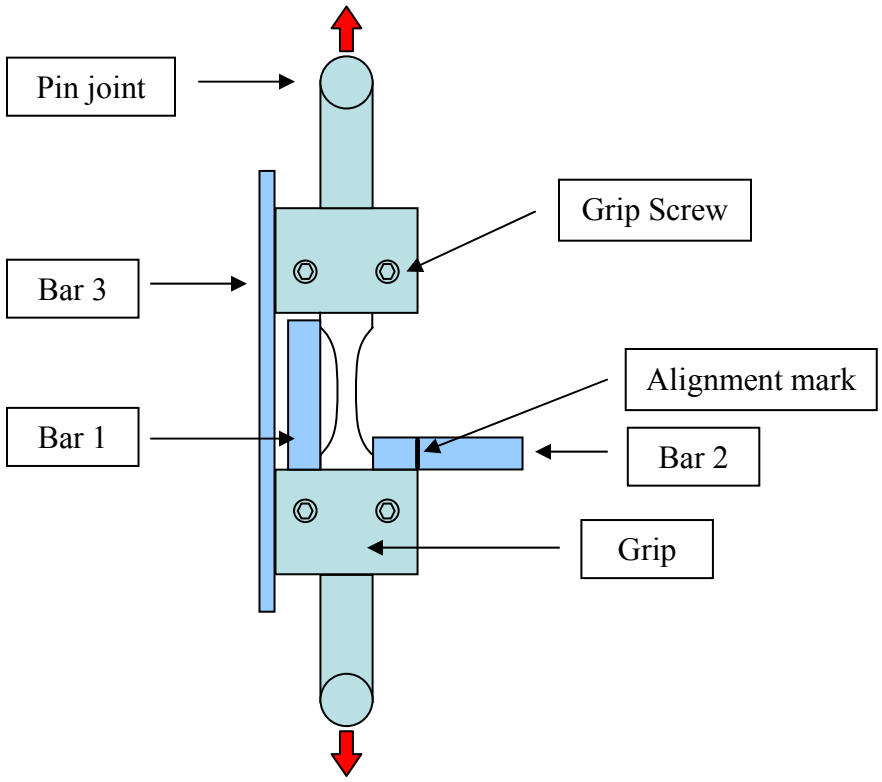

Figure 3.6: Schematic of specimen alignment procedure.

3.2.2 Results

The yield and tensile strength of the tested sheet was found to be 1263 MPa and 1322 MPa, respectively, based on the average of four tensile tests performed on dog-bone specimens from the batch of material used in this study, denoted as supplier 1 throughout. These values are compared to results from tests performed on material from a different supplier, denoted as supplier 2, and to values from MMPDS [92] in Table 3.3. The material from supplier 2 was purchased from McMaster-Carr in 0.2 mm thick sheet in as-rolled condition. The material was milled into specimens with the same dimensions as the supplier 1 specimens by the Georgia Tech Mechanical Engineering machine shop. Supplier 2 specimens were tested using the same equipment and procedure. Tests were also performed by Stork Technimet Inc using specimens fabricated with the same geometry and surface condition as specimens from supplier 1. The MMPDS data was likely obtained from thicker specimens. Good correspondence was found between the values of yield strength as well as ultimate strength between the two suppliers, however the variance in the values was higher for supplier 2. Both the yield strength and ultimate strength of the Stork specimens were slightly higher than that of the supplier 1 specimens, with a difference of 0.4% and 4.9% respectively.

Table 3.3: Comparison of tensile test results for 301 stainless steel in full hard condition.

GT Data, Supplier 1		**Stork Data [93]**		**GT Data, Supplier 2**		**MMPDS [92]**
0.2% Yield Strength (MPa)		**0.2% Yield Strength (MPa)**		**0.2% Yield Strength (MPa)**		**0.2% Yield Strength (MPa)**
Mean	1263	Mean	1268	Mean	1262	1055
Standard Deviation	44.8	Standard Deviation	38.0	Standard Deviation	70.1	
Count	4	Count	9	Count	13	
UTS (MPa)		**UTS (MPa)**		**UTS (MPa)**		**UTS (MPa)**
Mean	1322	Mean	1390	Mean	1302	1276
Standard Deviation	30.0	Standard Deviation	34.3	Standard Deviation	76.5	
Count	4	Count	9	Count	13	

A typical stress-strain plot is shown in Figure 3.7 for material from supplier 1. The material demonstrates a nearly elastic-perfectly plastic behavior. Concentrated deformation (Lüders) bands started to become visible on the surface of the specimen just past yielding and expanded with further deformation as shown in Figure 3.8. The high visibility of these Lüders bands is likely due to the low stacking fault energy of type 301, which promotes deformation bands and twins. The stability from the onset of necking has been attributed to the local hardening due to martensitic transformation [8].

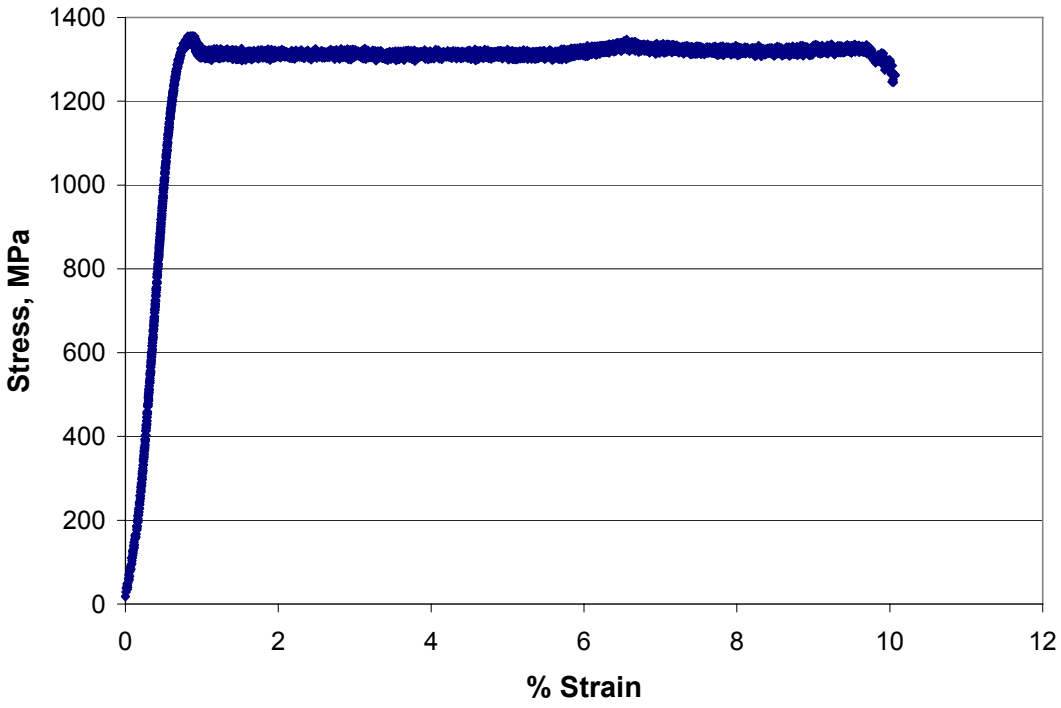

Figure 3.7: Typical tensile test result for material from supplier 1.

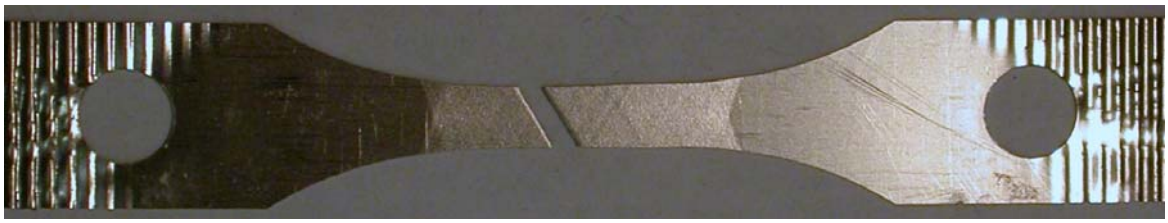

Figure 3.8: A tensile specimen showing the formation of Lüders bands in the gage section.

3.3 Fatigue Testing

3.3.1 Procedure

Fatigue testing was performed using the same equipment as tensile testing, and using specimens of the same dimensions shown in Figure 3.4. Fatigue tests were conducted at a force ratio R of 0.05. All tests were performed at a constant frequency of 10Hz. Testing thin specimens required careful tuning of the servohydraulic system because the stress depends sensitively on the force for a small cross sectional area. The tuning parameters were adjusted to P = 9.20, I = 0.39, and D = 0 in Teststar IIs. The value for D was set to zero so as not to risk introducing instability.

Before testing the material from supplier 1, fatigue tests were performed on material from supplier 2 to investigate the sensitivity of the results on sample preparation. The first study examined edge finish. Specimens had the same as-received face finish and were milled to the same dimensions. The edges of the specimens were then ground to 3 different finishes. The first condition was generated by sanding the edge of supplier 2 specimens longitudinally with successfully finer abrasive particles, starting with P320 grit, proceeding to P600 grit, and then finishing with P1200 grit SiC paper, denoted 1200 grit finish. Another condition was generated in the same manor using P320 grit SiC paper with a longitudinal stroke, denoted 320 grit finish. A third set was generated using P180 grit SiC paper with sanding motion in the transverse direction on supplier 2 specimens. This final condition was brushed in the transverse direction in order to generate the worst case scenario. This set is denoted 180 grit finish.

3.3.2 Results

The stress-life (S-N) data showing the effect of edge finish is shown in figure 3.9. Failure is defined as the separation of the specimen into two pieces. Arrows indicate that the test was stopped before failure. The 1200 grit finish had the highest fatigue limit with a stress amplitude of 448 MPa. A 320 grit finish reduced the fatigue limit to 455 MPa. A large reduction in fatigue limit was apparent for the 180 grit finish, reducing the fatigue limit to 255 MPa. Because of the importance of the surface finish, the edges of all specimens were polished using longitudinal strokes to have a maximum surface roughness R_y of 0.2μm.

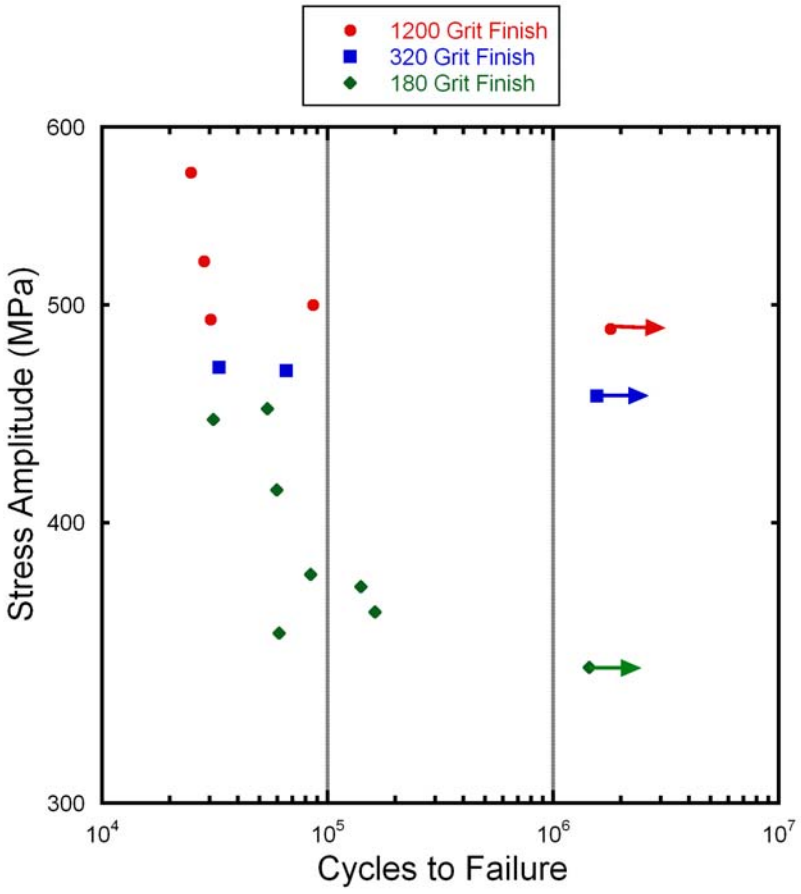

Figure 3.9: S-N plot showing effect of edge finish on supplier 2 material for R = 0.05.

Data from fatigue tests performed on material from supplier 1 is shown in Figure 3.10 along with data generated on supplier 2 material and data from Stork Technamet Inc. The Stork data included tests with both 4% pre-strain and without any pre-strain. The Stork data yielded higher fatigue limits compared to tests conducted at Georgia Tech, with values of 552 MPa without pre-strain and 483 with 4% pre-strain versus 468 MPa when tested in the MPRL. Table 3.4 summarizes the fatigue limits recorded in terms of stress amplitude.

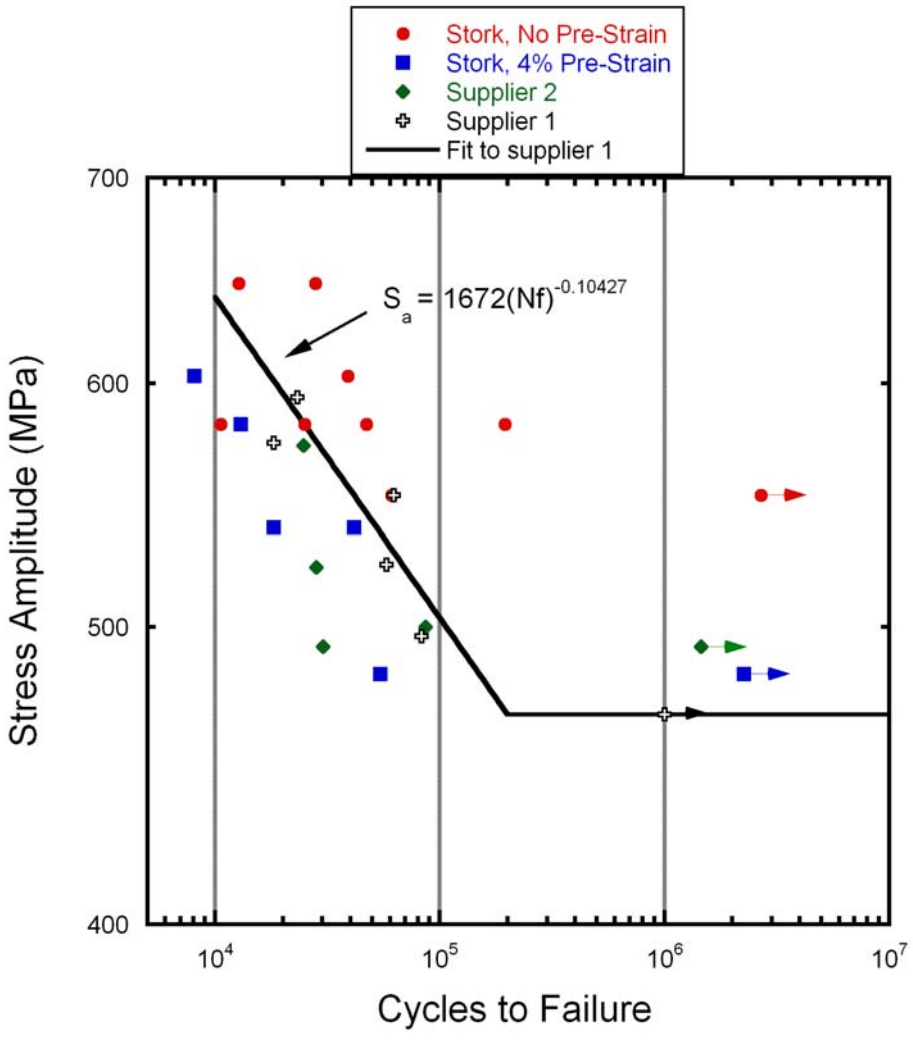

Figure 3.10: Plain fatigue S-N with R = 0.05.

Table 3.4: Summary of fatigue limits.

	Fatigue Limit (MPa)
Stork, no pre-strain	552
Stork, 4% pre-strain	483
Supplier 1	468
Supplier 2, 1200 grit	488
Supplier 2, 320 grit	455
Supplier 2, 180 grit	255

There are several factors associated with testing that contribute a small amount of scatter in the fatigue life results. Because of the small cross sectional area of the samples used, a relatively small force can cause a large change in the stress. For these samples, a change of 1 lb corresponds to a stress change of over 4 MPa. Because the force transducer used has a range of 2,000 lb, it was difficult to resolve the specified stress range, especially at higher frequencies. This caused some variation in the force ratio R which in turn affects the number of cycles to cause failure for certain stress amplitude. Another source of variation was the specimen alignment. Although great care was taken to be consistent, it was sometimes not possible to obtain perfect alignment. In addition, some variation in the fatigue life is due to microstructural influences, such as inclusion content and variation in the heterogeneity of the microstructure from supplier to supplier.

3.4 Fatigue Crack Growth Testing

Figure 3.11 shows the idealized fatigue crack growth behavior of a typical metal. Region I is the slow crack growth regime. The threshold stress intensity range, or ΔK_{th}, is the largest value of ΔK that does not result in the growth of a crack. Region II, or the

Paris Region, is represented as a power relation between the crack growth rate and the stress intensity range,

$$\frac{da}{dn} = c\Delta K^{m} \tag{3.1}$$

Region III is the fast crack growth region. The critical stress intensity, K_c, is the value of K at which crack growth becomes unstable, resulting in fast fracture of the material. Knowing the parameters that define this curve is essential for performing any crack growth modeling, which was performed in this study and is discussed in a later chapter.

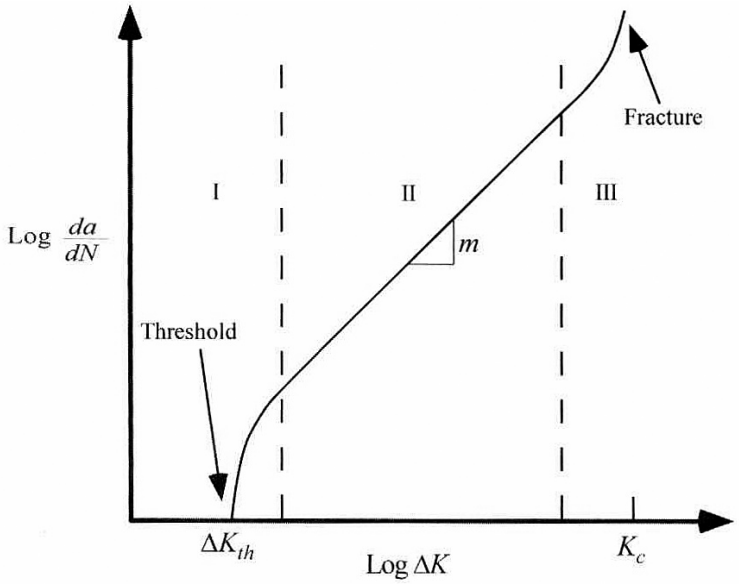

Figure 3.11: Typical fatigue crack growth behavior of metals, illustrating regions of crack growth for R = 0.

3.4.1 Procedure

Two fatigue crack growth experiments were conducted in the MPRL. Middle tension specimens, M(T), with dimensions shown in Figure 3.12 were fabricated and tested in accordance with ASTM E 647-05. The end of the specimen was designed to be

accommodated by the grips that were used for the tensile testing and fatigue testing so that the test system shown in Figure 3.3 could be used. The specimen was designed so that the width is the same as the width of the grips to aid in alignment. The starter notch was machined using plunge electrical discharge machining (EDM) for increased accuracy and minimization of unwanted deformation in the out of plane direction, which is often a problem when using a mechanical drill to form a hole in a thin sheet. Fatigue cracks are initiated at both sides of the center hole because of the stress concentration.

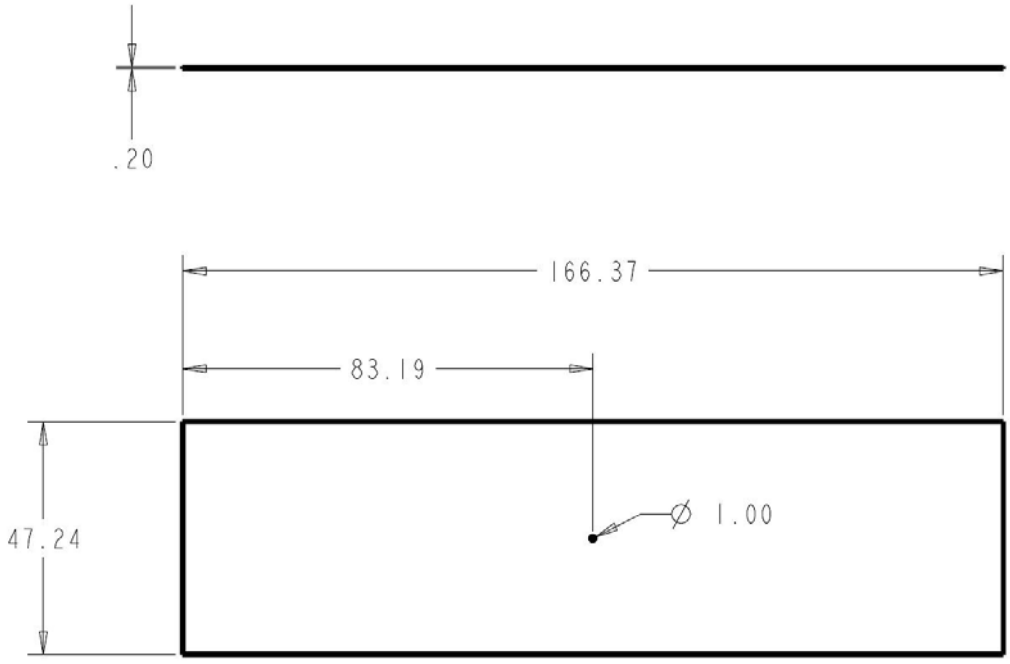

Figure 3.12: Specimen used in crack growth testing (dimensions in millimeters).

The specimen was cycled at a force ratio R of 0.05 and a frequency of 10 Hz at constant stress amplitude. Using AFGROW [94], values for 301 stainless steel (full hard) reported in the NASGRO (included with AFGROW), estimates of the crack growth

response were obtained to set the pre-cracking and testing stress amplitude. The loading histories for the two tests are given in the Table 3.5.

Table 3.5: Loading conditions of (a) Specimen 1 and (b) Specimen 2 during fatigue crack growth testing.

(a)

Test Phase	Cycles	Minimum Force (N)	Maximum Force (N)
Pre-Cracking	0-18,700	151	3038
Pre-Cracking	18,700-52,000	244	4047
Pre-Cracking	52,000-60,114	222	3692
Growth Rate Test	61,114-89,443 (failure)	151	3038

(b)

Test Phase	Cycles	Minimum Force (N)	Maximum Force (N)
Pre-Cracking	0-17,600	204	4087
Pre-Cracking	17,600-31,987	215	4314
Pre-Cracking	31,987-35,345	203	4074
Pre-Cracking	35,345-49,432	167	3335
Growth Rate Test	49,432-71,514 (failure)	151	3038

In both tests, the initially imposed force amplitude was not adequate to initiate a propagating crack at the edge of the center hole in a timely manner. Therefore, the force amplitude was increased to expedite nucleation. The edges of the hole were monitored using a long focal length microscope (Questar QM100) as is shown in Figure 3.13. After cracks initiated at the notch the force amplitude was lowered back down to the desired value. This reduction was done in two small steps in order to avoid effects from the

enlarged plastic zone caused by the higher force amplitude in accordance with ASTM E 647-05, which specifies that a higher force amplitude may be used in pre-cracking but it must be decreased by no more than 20% per step, and another force amplitude decrease must not be made until the crack had propagated at least 0.2 mm. Once the crack had propagated out of the zone affected by the stress concentration at the hole and out of the plastic zone created by the higher loading, the force amplitude was reduced to the desired value and crack measurements were taken at frequent intervals. The length of the interval was decreased as the crack growth rate increased to better capture the Region III behavior.

Figure 3.13: Middle Tension crack growth specimen being monitored by a long focal length microscope.

Crack measurements were taken by pausing the test at peak force (in order to capture the crack in the most open state) and making an acetate replica of the crack. This was done by placing a drop of acetone on the crack and placing a 23 μm thick piece of acetate ("thin replicating tape", Earnest F Fullen Inc, Serial No. 14690) onto the acetone covered crack. After approximately twenty seconds or until the acetone had dried, the cellulose was removed from the cracks on the specimen and placed between two glass microscope slides. These replicas were then measured using an optical microscope at 50x magnification with a graduated eyepiece. These measurements were taken more frequently as the test progressed because of the increase in the crack growth rate.

From ASTM E 647 - 05 Annex A.2, the stress intensity solution for a M(T) specimen is

$$\Delta K = \left(\frac{\Delta P}{B}\right)\sqrt{\frac{\pi\alpha}{2W}\sec\frac{\pi\alpha}{2}} \tag{3.2}$$

where ΔP is the force range, B is the specimen thickness, W is the specimen width, a is the crack length measured from the centerline of the specimen, and α is the ratio 2a/W. Because ΔK increases with the crack size, it was possible to obtain a range of ΔK even though constant loading was maintained.

3.4.2 Results

The crack length measurements taken during each of the 2 tests are shown in Figure 3.14.

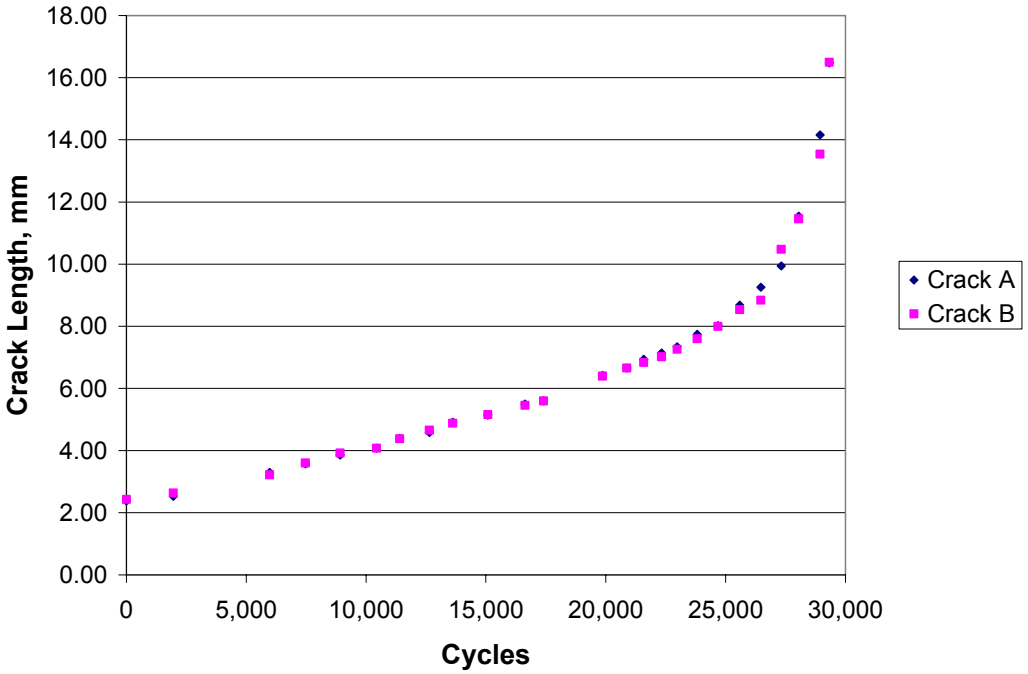

(a)

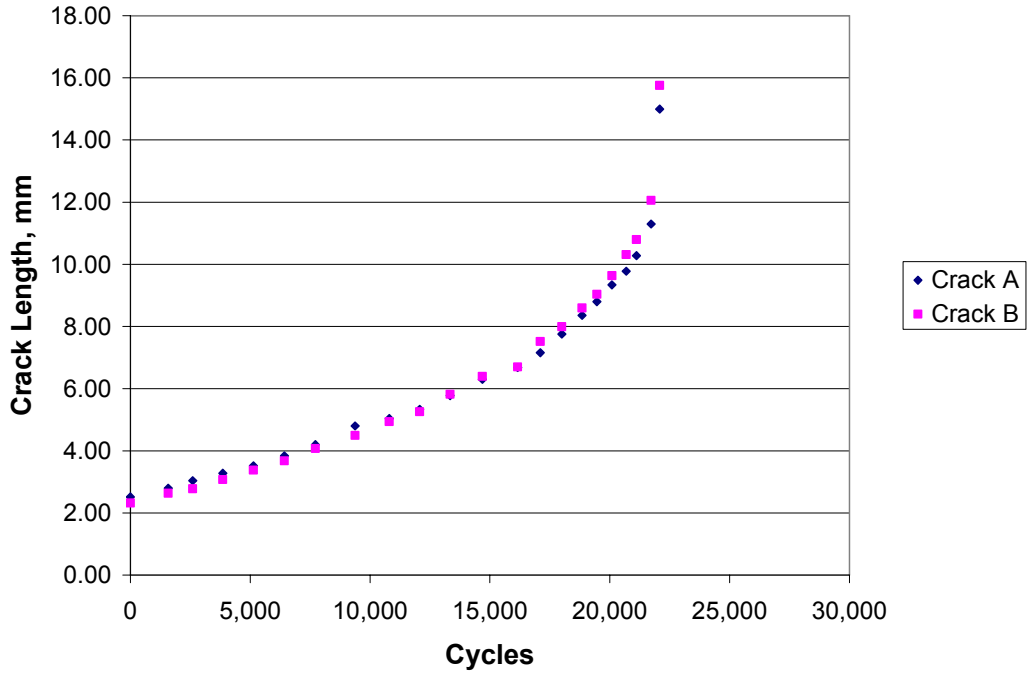

(b)

Figure 3.14: Crack length vs. cycle count for (a) Specimen 1 and (b) Specimen 2 where Crack A and Crack B are the cracks on each side of the center hole.

Figure 3.14 shows that there was a strong correspondence between the cracks on each side of the center hole for both specimens. This shows the stress distribution was adequately symmetric, indicating that alignment was satisfactory.

The experimental results were compared to a crack growth model which is based on the NASGRO 3.0 equation, described in [94], reduced for the case of R = 0.05 and for a specimen thickness of 0.2 mm. The crack growth rate is given by

$$\frac{da}{dN} = C\Delta K^n \frac{\left(1 - \frac{\Delta K_{th}}{\Delta K}\right)^p}{\left(1 - \frac{K_{\max}}{K_{crit}}\right)^q} \tag{3.3}$$

where

$$\Delta K_{th} = \frac{\Delta K_0 \left(\frac{a}{a + a_0}\right)^{\frac{1}{2}}}{1.04423} \tag{3.4}$$

The constants used to represent AISI 301 stainless steel in the full hard condition were obtained from the NASGRO database, provided with the AFGROW code, and are given in Table 3.6.

Table 3.6: NASGRO constants for AISI 301 stainless steel in full hard condition for the case of R = 0.05 and specimen thickness of 0.2 mm.

Paris crack growth rate constant, C (MPa^{-n} $m^{1-n/2}$)	6.18×10^{-11}
Paris exponent in NASGRO equation, n (dimensionless)	2.2
Exponent in NASGRO equation, p (dimensionless)	0.25
Exponent in NASGRO equation, q (dimensionless)	0.25
Threshold stress intensity factor range at R=0, ΔK_0 (MPa $m^{0.5}$)	3.846
Intrinsic crack length, a_0 (μm)	38.1
Critical stress intensity factor, K_{crit} (MPa $m^{0.5}$)	131.86

The experimental crack growth rate and NASGRO model results are shown in Figure 3.15. The experimental values lie slightly higher than the NASGRO model, and the experimental data only covers the top half of the range of ΔK. A decreasing ΔK test, where the force amplitude is decreased as the crack length increases, would be needed to capture the Region I crack growth response.

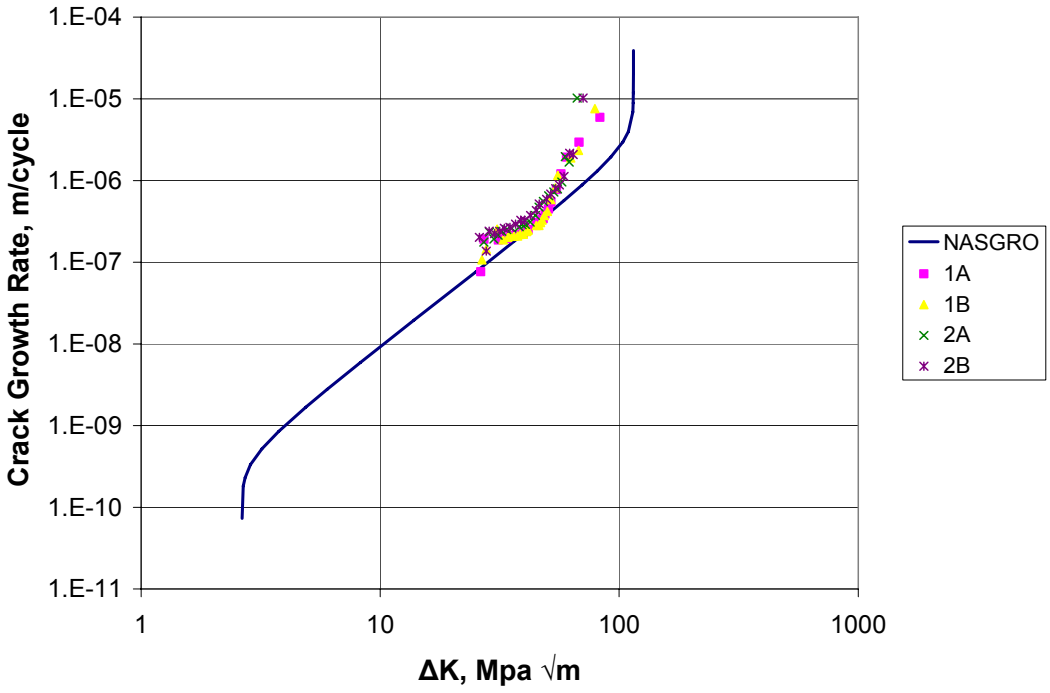

Figure 3.15: Experimental fatigue crack growth rate results plotted results using the NASGRO model for R = 0.05.

The average value of K_c based on the four crack sizes is 102 MPa√m, compared to a value of 132 MPa√m predicted using NASGRO, as shown in Table 3.6. It is likely that the discrepancy is due to a thickness effect. As shown in Figure 3.16, the toughness can decrease with decreasing thickness when samples are below a critical value [18]. It is likely that the specimens used to generate the NASGRO data were thicker than the material used in the experiments performed in this study. Thus, it is possible that the samples used here are thin enough to be in region I labeled in Figure 3.16, whereas the value in the NASGRO model is from region II.

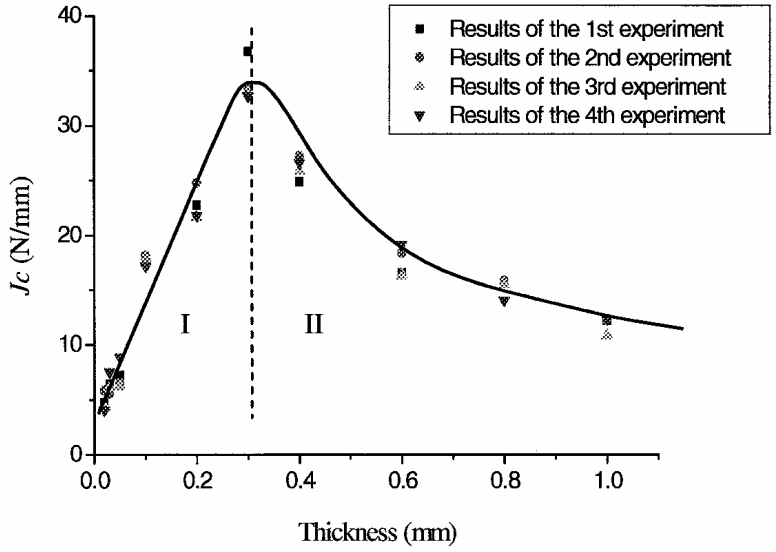

Figure 3.16. Variation of the fracture toughness with specimen thickness for copper foil [18].

A power law regression was performed on each set of data in the Paris Region to find the Paris Law constants. Table 3.7 shows the values of the Paris constant and Paris exponent with the R^2 value associated with the regression and compares it with the values supplied in the NASGRO database. Crack 2B, which had the highest R^2 value, had good correspondence with the NASGRO data, which suggests that the use of the NASGRO

model with the material data stored in the database is appropriate for use with a change in the critical stress intensity factor, K_c.

Table 3.7: Crack growth parameters.

	Crack 1A	Crack 1B	Crack 2A	Crack 2B	NASGRO
Paris Exponent	2.29	2.77	2.42	2.21	2.2
Paris Coefficient, m/(cycle-MPa√m)	5.43E-11	9.18E-12	4.52E-11	1.09E-10	1.14E-10
R^2	0.86	0.78	0.93	0.96	--
K_C, MPa√m	106.8	107.1	93.7	100.1	131.86

CHAPTER 4

FRETTING EXPERIMENTAL PROCEDURES

The impact of fretting on the fatigue response of AISI 301 stainless steel sheet was characterized using a two step process. First, fretting damage was generated using a Phoenix Tribology DN55 High Temperature Fretting Machine, causing cracks to initiate in the sample. Second, the residual fatigue life was found by performing fatigue tests on the damaged samples. Cracks formed during fretting grow under cyclic loading until the specimen fails. The residual fatigue life demonstrates the severity of fretting damage since more severe damage will result in a lower residual fatigue life.

4.1. Fretting Machine

Fretting tests were conducted using a Phoenix Tribology DN55 Fretting Machine shown schematically in Figure 4.1. A cylindrical moving specimen is clamped into the servohydraulic actuator. The position of the actuator is closed-loop controlled using feedback from a capacitance gage located at the top end of the actuator. The displacement amplitude of the moving specimen can be controlled from 15μm to 400μm at frequencies up to 400Hz. The moving specimen can be a sphere which creates a point contact, a cylinder which creates a line contact, or a cylinder rotated 90 degrees to create area contact.

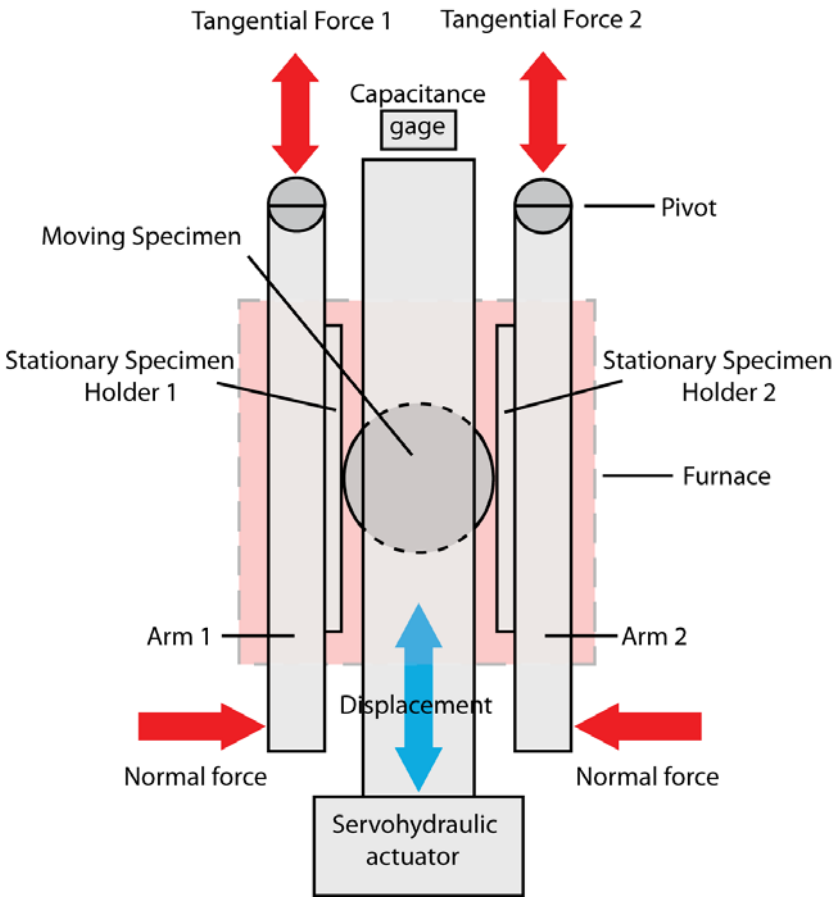

Figure 4.1: Schematic representation of a Phoenix Tribology DN55 Fretting Machine.

A stationary specimen is clamped into each arm. The normal force between the moving specimen and the stationary specimens is developed by applying a force to the ends of the arms by a pneumatic actuator. Tangential force generated from friction at the contact is transmitted by each arm to a piezoelectric force transducer at the top of the arms. The tangential force and the position of the actuator are stored on the host computer at a rate of 1 kHz. Because the displacement is measured remotely, the measurement includes compliance of the system. Therefore, displacement amplitudes reported are considerably larger than the actual displacement at the contact interface, which cannot be measured directly.

A furnace can be attached around the region shown in Figure 4.1 allowing tests to be performed at elevated temperature. Heat sensitive components are located away from the specimens so tests can be run at temperatures as high as 800^{o}C. Similarly, a gas chamber can be fitted around the experiment, allowing tests to be performed in a controlled atmosphere.

4.2 Specimen Holder Design

The specimen holder shown in Figure 4.2 holds thin specimens in place during testing. The holder is designed to hold the dogbone specimens shown in Figure 3.4 as well as strip characterization specimens that have the same width as the gage section of the dogbone specimens but no grip region and a length of 76 mm. The arm adapter shown in Figure 4.2(c) is attached to the backing plate with one M3 screw and is shaped to fit into a recess in the arms of the fretting machine. The whole assembly is then fastened into the arm with one M5 screw to create a rigid interface.

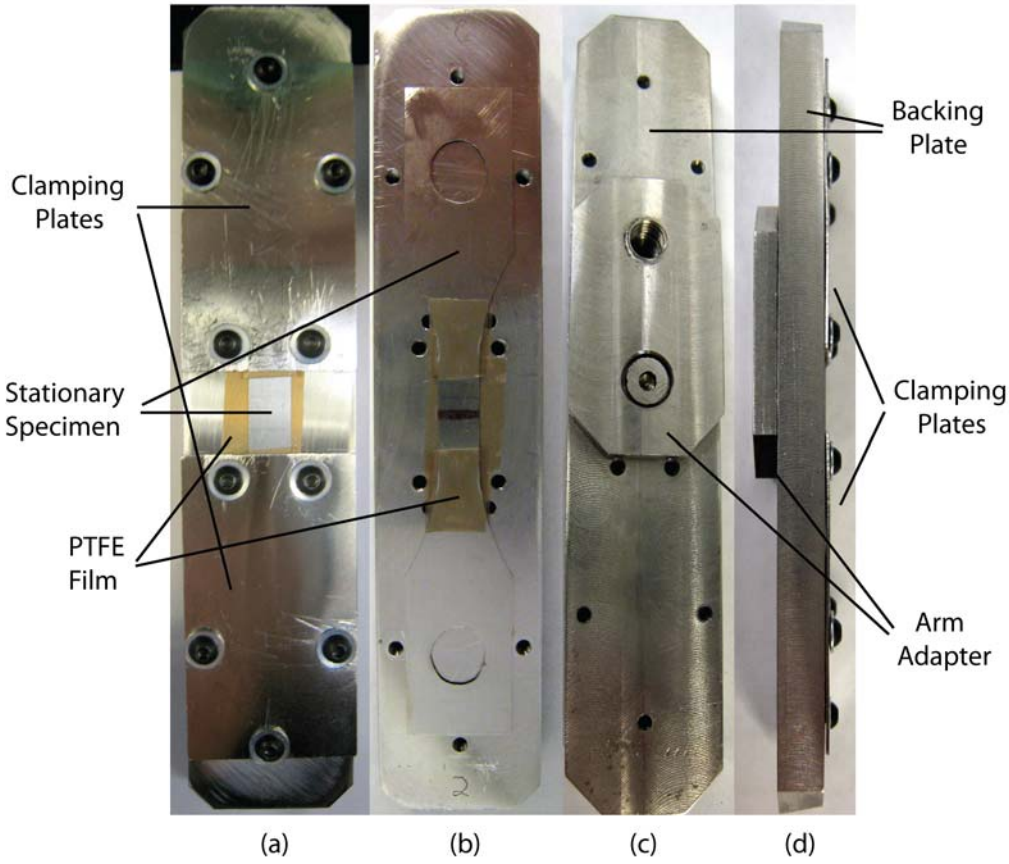

Figure 4.2: Stationary specimen holder showing the (a) top view of unfretted specimen with clamping plates in place, (b) top view of fretted specimen with clamping plates removed, (c) back view, and (d) side view.

The clamping plates secure the specimens in the holder. They are made of 0.38 mm thick stainless steel, and are attached to the backing plate using five M2 screws. The material of the holder was selected to have the same coefficient of thermal expansion (CTE) as the specimen so thermal stresses will not be generated in the specimen during heating in elevated temperature tests. To prevent unwanted fretting between the specimen and the holder, an 89 μm thick PTFE tape is adhered to the interface between the edge of the clamping plates and the specimen, as shown in Figure 4.2 (a) and (b). This area is prone to fretting because of the high contact stress from the square edge of the top plate

combined with the small amplitude relative motion from strains in the specimen from the friction force at the main contact. The PTFE tape reduces the COF, which lowers the contact stresses, and the compliance of the film helps to distribute pressure. PTFE tape was also used between the back of the specimen and the backing plate directly behind the location of the main contact to alleviate fretting between the back of the specimen and the backing plate. The PTFE layer also promotes self-alignment and hence more uniform pressure distribution across the gage width of the specimen.

4.3 Moving Specimens

Contacting bodies were chosen to be cylindrical with 20 mm diameter and 15 mm length. Using a cylindrical moving specimen creates line contact, which was chosen to simplify the analysis since the contact configuration can be modeled as 2D plane strain. Two materials were chosen for this study: AISI 52100 steel and ANSI A356 aluminum. These materials were chosen in order to represent a wide range of strength, stiffness, and corrosion resistance. The compositions of 52100 and A356 are shown in Table 4.1 from ASTM A 295/A 295M – 05 and ASTM B 108-06, respectively.

Table 4.1: Chemical composition of rider materials.

AISI 52100 Steel	
Component	**Wt. %**
C	0.93-1.05
Mn	0.25-0.45
Cr	1.35-1.60
Si	0.15-0.35
P	0.025 Max
S	0.015 Max
Ni	0.25 Max
Mo	0.10 Max
Cu	0.30 Max
O	0.0015 Max
Al	0.050 Max

ANSI A356 Aluminum	
Component	**Wt. %**
Al	90.1 - 93.3
Cu	0.25 Max
Fe	0.6 Max
Mg	0.2 - 0.45
Mn	0.35 Max
Si	6.5 - 7.5
Ti	0.25 Max
Zn	0.35 Max

The A356 specimens were machined out of a cast engine block provided by Dr. Charles E. Bates at the University of Alabama at Birmingham. The 52100 specimens were machined from an annealed rod purchased from McMaster-Carr. The surface finish of the rider samples were generated using a five step SiC abrasive paper progression. The rods were mounted on a lathe, and polished progressively using P320, P500, P600, P800, and P1200 Grit SiC abrasive paper. This was done carefully to ensure that there would be no inconsistency in the experiments due to variation in surface finish. After polishing, the rods were cut along the cross section to final dimension. The hardness of the 52100 and A356 is 21 HRC and 52 HRB, respectively.

4.4 Contact Alignment

The alignment of the fretting arms was adjusted to give a uniform pressure distribution along the line of contact between the moving specimen and stationary specimens. This was done by placing a sheet of pressure sensitive film between the stationary specimen and the moving specimen. If the pressure was not uniform, the

alignment was adjusted and checked again. This process was repeated until satisfactory alignment was obtained. Figure 4.3 shows the pressure sensitive film before and after alignment for each side of the machine. After alignment the contact on the right side is slightly more uniform than on the left side.

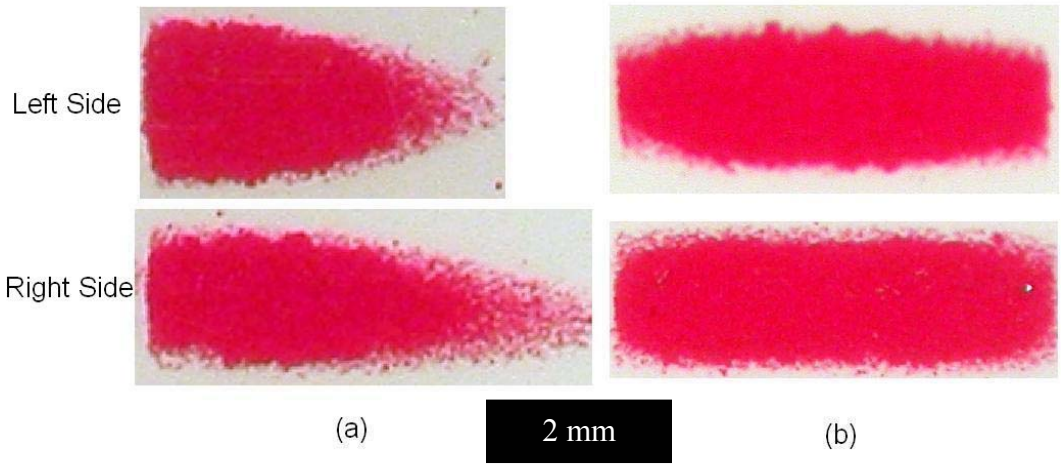

Figure 4.3: Contact pressure distribution (a) before alignment and (b) after alignment.

4.5 Test Parameters

Because the severity of fretting damage depends strongly on many parameters, it was necessary to perform many tests to fully characterize the response. Normal force, displacement amplitude, and contacting material were varied, while contact geometry, temperature, and atmosphere were kept constant. Although temperature and atmosphere are important parameters, they are out of the scope of this initial study. The effect of these parameters will be considered in future work using the current experimental setup.

A total of 64 tests were run: 35 against 52100 and 30 against A356. For each test, stationary specimen 1 was a strip characterization specimen and stationary specimen 2 was a dogbone specimen. Displacement amplitudes ranging from 15 to 200 μm were

used with normal forces of 100 or 255 N at room temperature and a frequency of 10 Hz. The frequency of the fretting test also has an effect on the response, though indirectly. Increasing the frequency leaves less time for dissipation of heat generated from friction which raises the temperature at the contact. This is important for stainless steel because of its relatively low thermal conductivity (16.3 W/m-K) and the sensitivity of temperature on martensitic transformation. The frequency was kept constant for all tests to minimize variation due to these effects. Future testing with elevated temperature and controlled oxygen content will determine the influence of these factors.

4.6 Damage Characterization

Damage generated during fretting was characterized by observation and experimentation to correlate fretting test conditions to the type and severity of damage. The strip characterization specimens were examined with an optical microscope. The surface was examined to understand the correlation between test conditions and surface appearance, such as the presence of wear debris, oxidation, and material transfer. Strip specimens were also sectioned and polished to identify subsurface features such as cracking and measure the depth of wear or thickness of transferred material.

Fretting damage generated was determined quantitatively by performing fatigue tests on dogbone specimens containing fretting damage using the same method described in section 3.3.1. The residual fatigue life found during subsequent fatigue tests was compared to the fatigue life of the same dogbone specimens without fretting damage to find the knockdown in fatigue life.

CHAPTER 5

RESULTS AND DISCUSSION

5.1 Fretting Results

5.1.1 Friction Response

Friction logs recorded during fretting tests were used to determine whether the running condition was partial, mixed, or gross slip for each test performed. The partial slip running condition was characterized by hysteresis loops that were initially closed and remained closed for the entire experiment. The mixed slip running condition was distinguished by a hysteresis loop that was initially open and evolved to a closed loop, whereas the gross slip running condition was characterized by an open hysteresis loop for the entire duration of the experiment. Examples of friction logs for contact with 52100 and A356 in the mixed slip and gross slip regimes are shown in Figure 5.1.

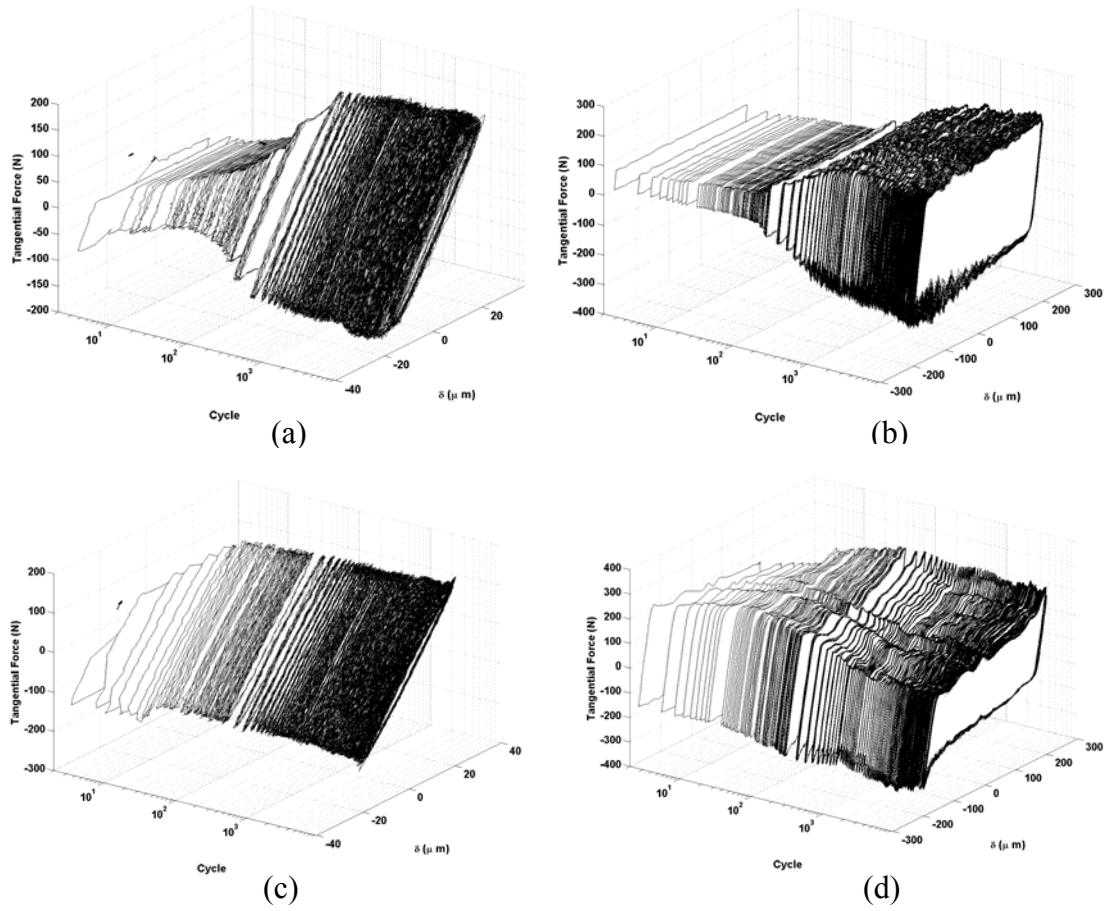

Figure 5.1: Friction logs with a normal force of 255 N for contact with and displacement amplitudes of (a) 52100 and 20 μm (MSR), (b) 52100 and a 200 μm (GSR), (c) A356 and a 20 μm (MSR), and (b) A356 and 200 μm (GSR), respectively.

Figure 5.2(a) shows hysteresis loops for several different cycles during a test with an A356 contacting body, normal force of 255 N, and 100 μm displacement amplitude. Initially, the tangential force is uniform for the entire sliding portion of the stroke. As the test progresses to 100 cycles, the tangential force increases over the entire displacement range. As the cycle count increases, the tangential force near zero displacement begins to decrease while the tangential force at the ends of the stroke begins to increase. The value of the tangential force ratio (ratio of tangential force to normal force) based on the

tangential force near the center of the displacement and the peak tangential force are shown in Figure 5.2(b). The spike in tangential force near the end of the stroke is due to an interaction between aluminum deposited on the 301 specimen and a hemi-cylindrical trough formed on the aluminum contacting body. The deposit comes into contact with the edge of the trough at the ends of the stroke that imparts a significant tangential component to the specimen. This causes an apparent rise the COF to as high as 1.4 as the deposit and trough grow compared to the actual sliding value of 0.5. This phenomenon has been observed during other fretting tests involving ductile materials such as aluminum [95-97].

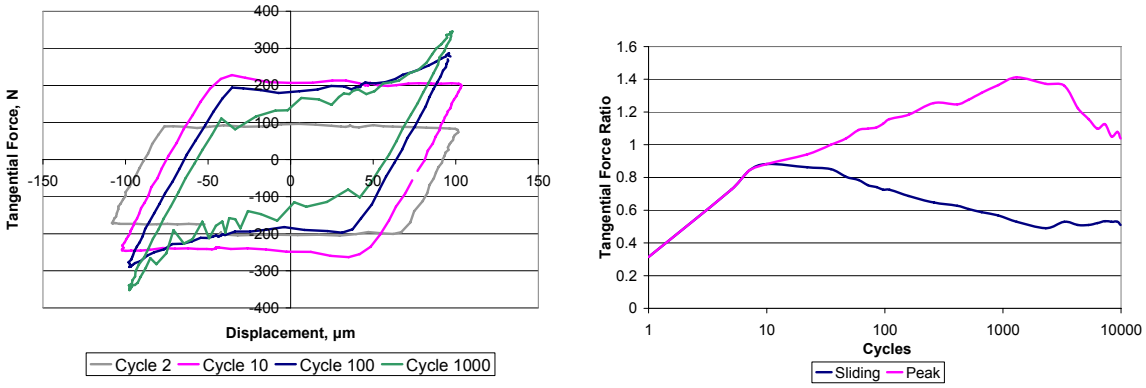

(a) (b)

Figure 5.2: (a) Hysteresis loops for several different cycles for fretting against A356 with a normal force of 255 N and a 100 µm displacement amplitude and (b) a comparison between the sliding and peak tangential forces as a function of cycles.

The evolution of the tangential force ratio for contact with A356 and a normal force of 255 N for various displacement amplitudes is shown in Figure 5.3. Solid lines represent gross slip conditions (open hysteresis loop) and dotted lines represent partial

slip conditions (closed hysteresis loop). Tangential force values for gross slip are based on the tangential force near the center of stroke whereas tangential force values for partial slip conditions are based on the peak since the center value would be approximately zero. The test conducted with a 10 μm displacement amplitude was the only test that resulted in a partial slip running condition. The transition from gross slip to partial slip occurs later for higher displacement amplitudes. Tangential force increases until the transition to partial slip and then remains constant for the duration of the test. For tests resulting in a gross slip running condition, the tangential force increases to a maximum value and then decreases to a steady state value after approximately 10^3 cycles. The decrease occurs more rapidly for higher displacement amplitudes.

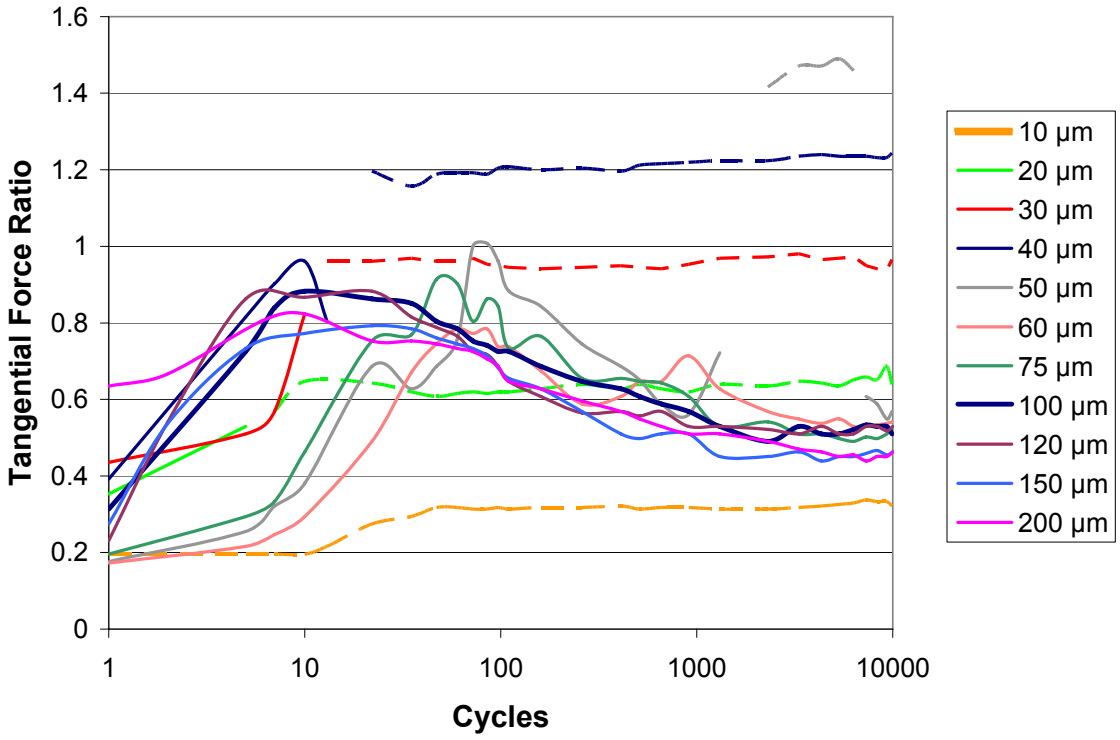

Figure 5.3: Tangential force ratio evolution for contact with 301 with a normal force of 255 N against A356 and various displacement amplitudes where dotted lines identify a partial slip condition and solid lines identify a gross slip condition.

The evolution of the tangential force ratio for contact with 52100 with a 255 N normal force and various displacement amplitudes is shown in Figure 5.4. The test performed with a 10 μm displacement amplitude was the only test with a partial slip running condition, and the 20 μm test was the only mixed slip running condition. The initial value of the tangential force ratio was lower than for contact with A356, and the maximum value was reached after more cycles. This is a consequence of the lower wear rate for contact with 52100 due to its higher hardness. The tangential force value decreases slightly toward the end of the test, however, a test conducted with a displacement amplitude of 100 μm for 10^5 cycles showed that the tangential force does not decrease significantly beyond 10^4 cycles.

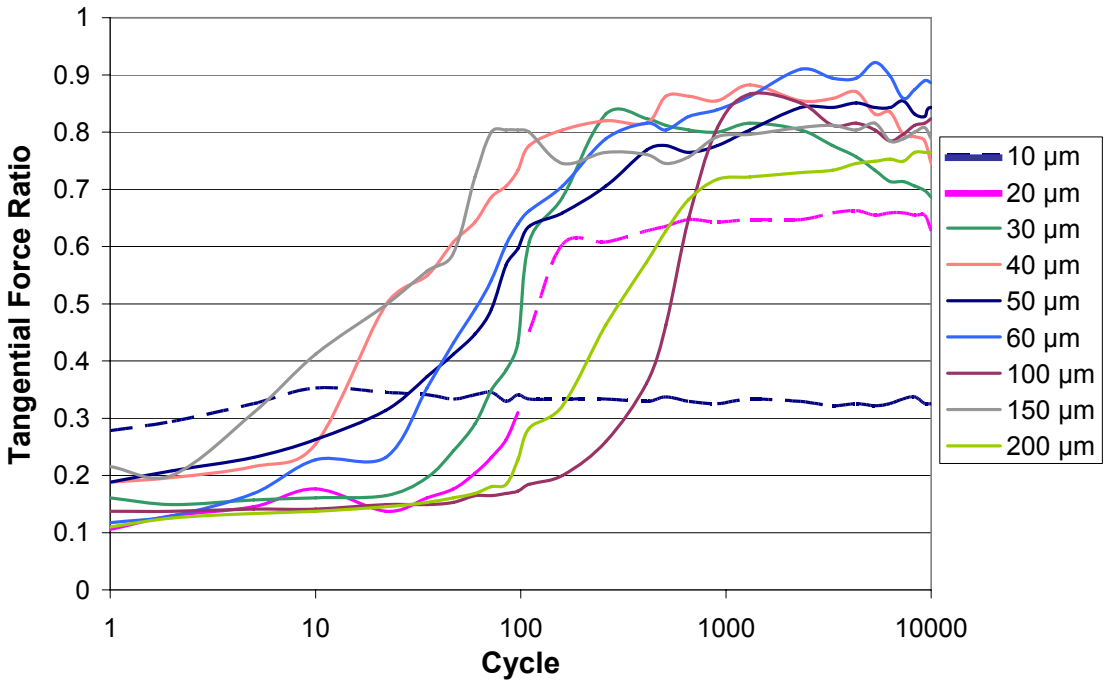

Figure 5.4: Tangential force ratio evolution for contact with 301 with a normal force of 255 N against 52100 and various displacement amplitudes where dotted lines identify a partial slip condition and solid lines identify a gross slip condition.

The steady state values of the tangential force ratio for contact with A356 for a 255 N normal force and various displacement amplitudes are shown in Figure 5.5. The maximum tangential force ratio occurred at the highest displacement amplitude in the mixed slip regime with a value of 1.22. The tangential force ratio decreases with increasing displacement amplitude after the transition to the gross slip regime.

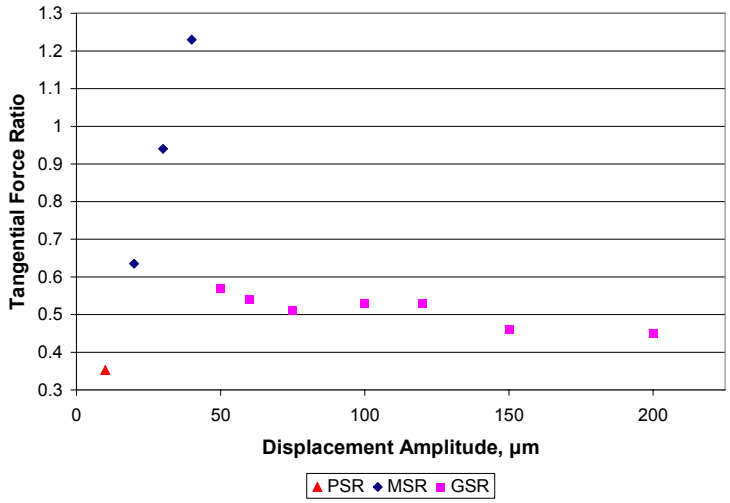

Figure 5.5: Tangential force ratio after 10^4 cycles for contact of 301 against A356 with a normal force of 255 N and various displacement amplitudes showing the corresponding running condition.

The steady state values of the tangential force ratio for 301 in contact with 52100 for a normal force of 255 N and various displacement amplitudes are shown in Figure 5.6. The maximum value of the tangential force does not occur at the upper limit of the MSR as it does for contact with A356. The tangential force continues to increase to a maximum at a displacement amplitude of 60 µm. Similar to contact with A356, the tangential force continues to decrease with increasing amplitude. The average COF after 10^4 cycles for displacement amplitudes that result in a gross slip running condition is

60% higher for contact with 52100 than with A356. However, the maximum value over the first 10^4 cycles is nearly equal.

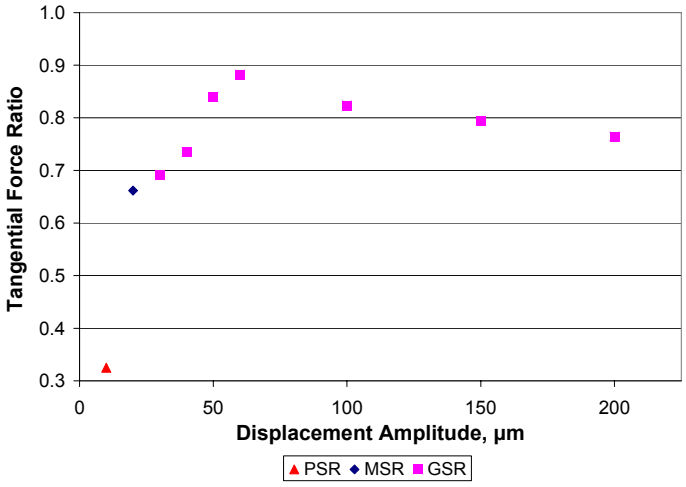

Figure 5.6: Tangential force ratio after 10^4 cycles for contact of 301 against 52100 with a normal force of 255 N and various displacement amplitudes showing the corresponding running condition.

A running condition fretting map was created for 301 in contact with A356 at three normal forces, shown in Figure 5.7. The lines drawn represent the expected boundaries between the different regimes. The PSR-MSR transition was found to occur between 20 and 30 µm with a normal force of 375 N, between 10 and 20 µm for a normal force of 255 N, and was below 10 µm for a normal force of 100 N. The MSR-GSR was found to occur between 67 and 75 µm for 375 N, 50 and 60 µm for 255 N, and 15 and 20 µm for 100 N.

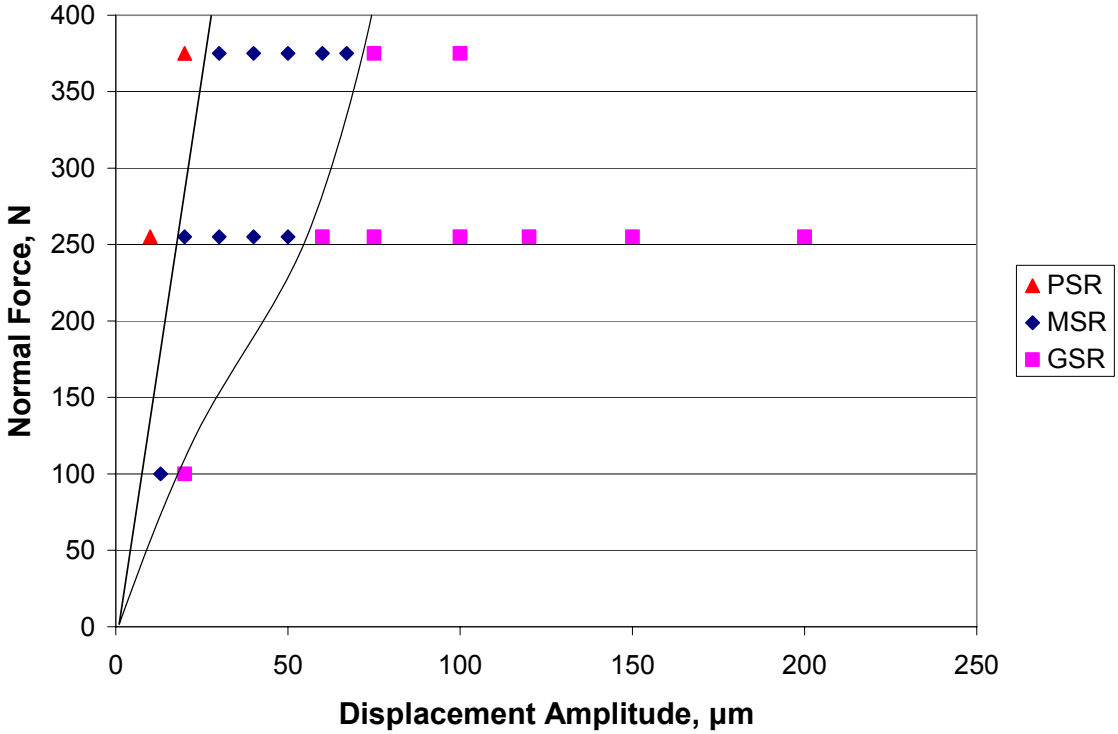

Figure 5.7: Running condition fretting map for contact against A356.

The running condition fretting map for 301 in contact with 52100 is shown in Figure 5.8. The PSR-MSR transition occurred between 10 and 20 µm for 255 N, and was below 10 µm for a normal force of 100 N. The MSR-GSR transition was found to occur between 20 and 30 for 255 N, and between 10 and 20 µm for 100 N. These transitions occurred at lower displacement amplitudes than for contact with A356. This is partly due to the higher stiffness of the 52100. Less elastic and plastic deformation takes place in the 52100 moving specimen than the A356 moving specimen, making sliding more likely to occur.

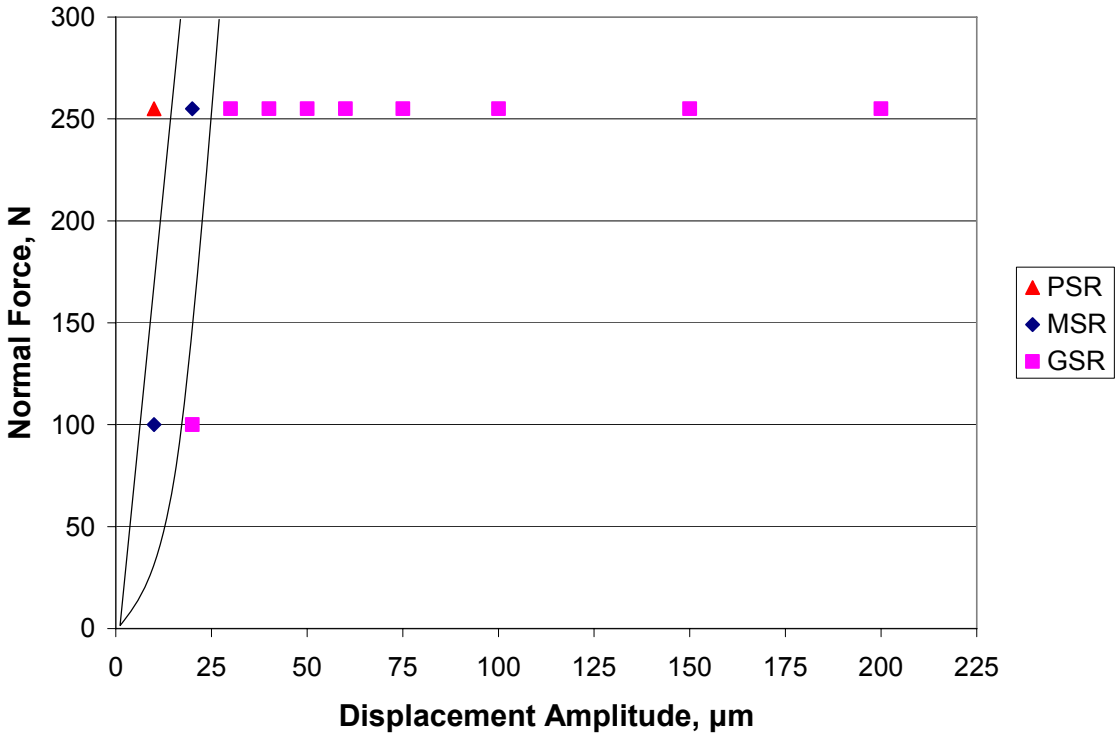

Figure 5.8: Running condition fretting map for contact against 52100.

The values of the steady-state COF observed in this study for normal forces of 255 and 375 were similar to values reported by other authors for contact of annealed 304 stainless steel against itself. Raman and Jayaprakash [14] found that steady-state values were reached by 10^4 cycles and were in the range of 0.6 to 1.0 for a grain size of 43 µm and were lower, in the range of 0.45 to 0.85, for a grain size of 277 µm. Kayaba and Iwabuchi [13] also found that steady-state values occur by 10^4 cycles for annealed 304 fretted against itself with a value of 0.65.

5.1.2 Fretting Scar Appearance

Figure 5.9 shows the fretting scars resulting from a mixed slip running condition and a gross slip running condition for contact with 52100 with a normal force of 255 N. When the displacement amplitude was 20 μm, the scar was light with a typical iron oxide color and almost no visible wear debris. A 200 μm displacement amplitude resulted in large amounts of oxide and wear debris. The composition of the debris was fine with a small amount of larger particles, indicative of abrasive wear. Because the specimens are vertical during testing, it is possible that larger debris was generated but fell from the sample. However, it is believed that the amount of larger debris was insignificant. Clumping of the fine debris may be caused by magnetism in the ferromagnetic α' wear debris.

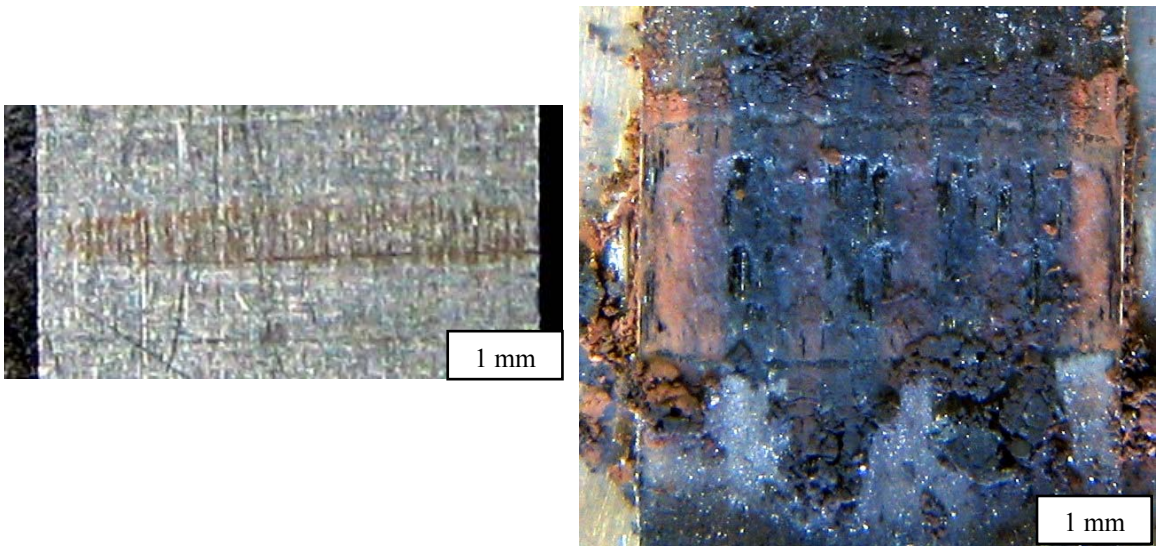

(a) (b)

Figure 5.9: Scars generated on 301 during fretting against 52100 with normal force of 255 N and displacement amplitudes of (a) 20 μm and (b) 200 μm.

Figure 5.10 shows the resulting fretting scars from contact of 301 with A356 with a normal force of 255 N for mixed slip and a gross slip running conditions. In the mixed slip regime the fretting scar is reflective, which indicates a lack of oxidation and transfer of aluminum to the 301 specimen. At larger displacement amplitudes the transfer of aluminum became obvious, and an increasing amount of black wear debris formed. Black cubic alumina (γ-Al_2O_3) has been found to form during fretting in other studies [24, 29, 44]. The moving specimen formed a hemi-cylindrical trough due to the loss of material.

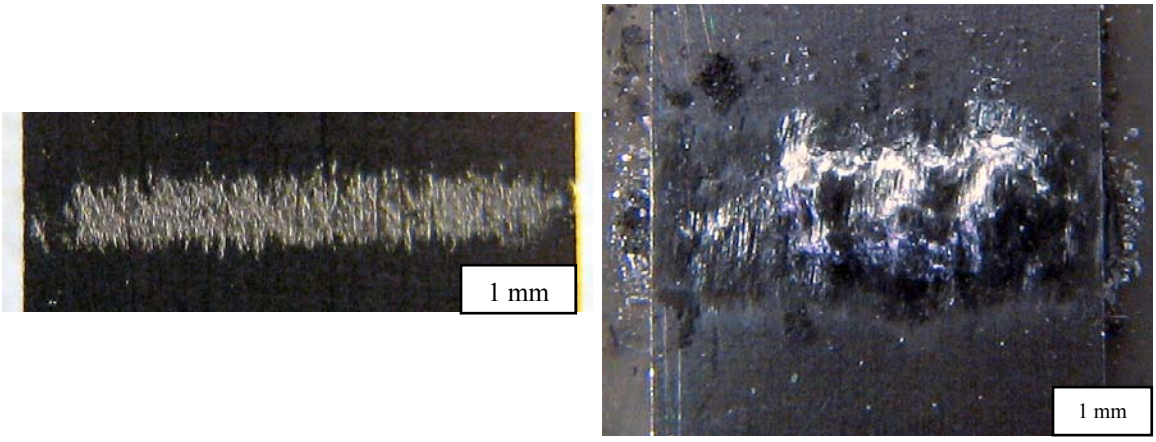

(a) (b)

Figure 5.10: Scars generated on 301 in fretting against A356 with a normal force of 255 N and displacement amplitudes of (a) 20 μm and (b) 200 μm.

Optical microscope images of scars resulting from contact with A356 and 52100 at 20 μm displacement amplitudes are shown in Figure 5.11. Both cases show signs of rough-surface contact. Both scars show portions of intact 301 between bands of contact which are oriented in the fretting direction. For the specimen in contact with A356 the

contact resulted in transfer of A356 to the 301 and contact with 52100 caused wear of the 301 and the formation of oxide.

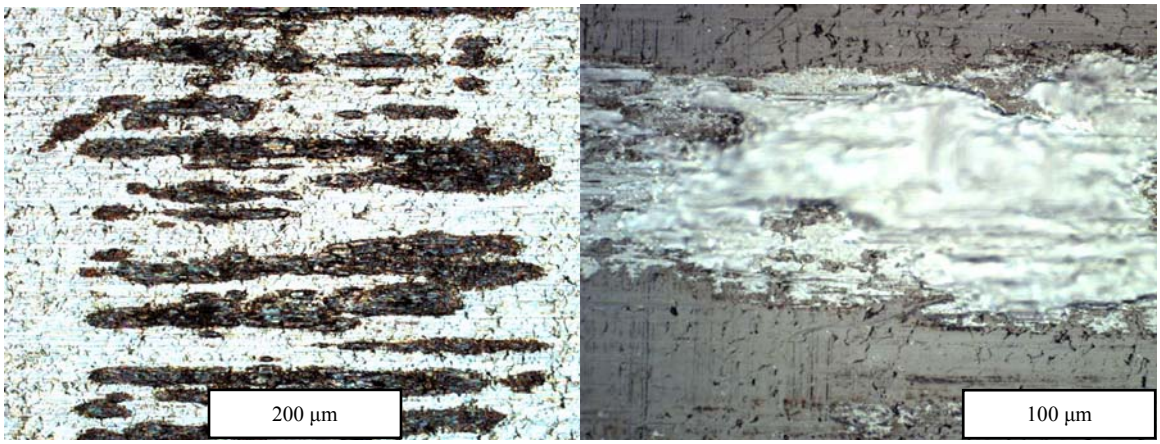

(a) (b)

Figure 5.11: Optical images of fretting scars resulting from a normal force of 375 N and a 20 μm displacement amplitude against (a) 52100 and (b) A356.

The profiles of scars were examined by sectioning and polishing samples using the method described in section 3.1.1. Polished samples were observed with an optical microscope to measure the depth of wear or the thickness of transferred material. The profiles of scars resulting from fretting tests with a normal force of 255 N are shown in Figure 5.12. Contact with A356 resulted in transfer of aluminum for all tests in the mixed slip and gross slip regimes with thicker layers for higher displacement amplitudes. The composition of the layer is mostly metallic with black oxide particles up to 20 μm in diameter distributed throughout.

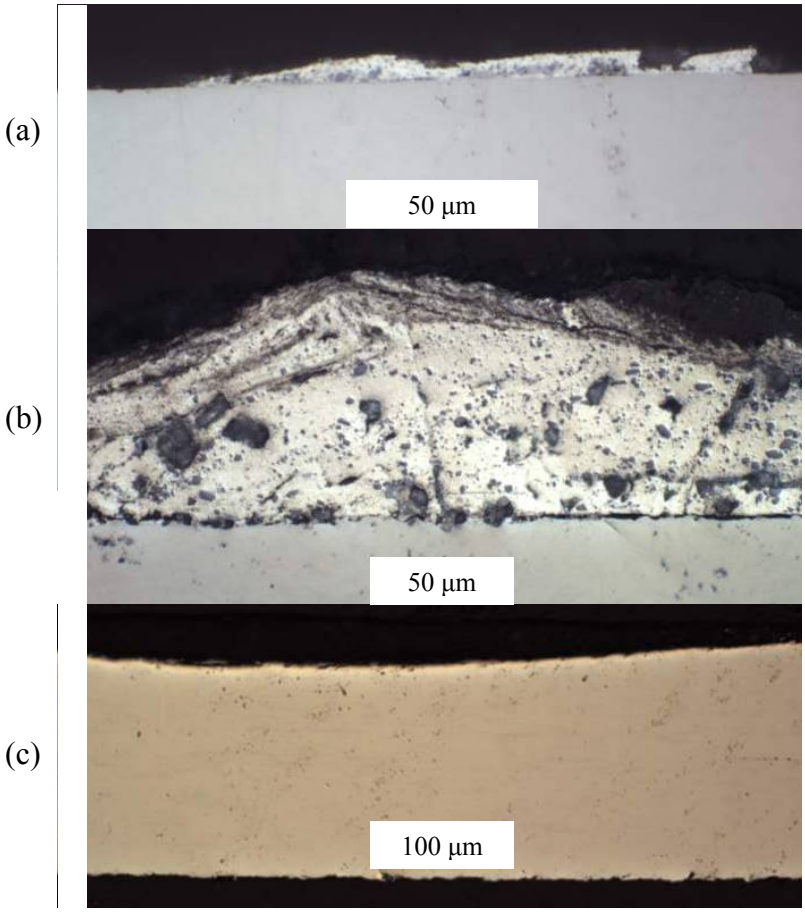

Figure 5.12: Profile of scars generated using a normal force of 255 N for contact with (a) A356 with a 40 µm displacement amplitude, (b) A356 with a 200 µm displacement amplitude, and (c) 52100 with a 200 µm displacement amplitude.

Figure 5.13 shows the height of aluminum deposited on 301 for contact with A356 and the depth of wear of 301 from contact with 52100 for various displacement amplitudes and a normal force of 255 N. Both the height of deposit and depth of wear increased with increasing displacement amplitude. The aluminum deposit reached a maximum of 80 µm for a displacement amplitude of 200 µm, and the maximum wear depth was 30 µm.

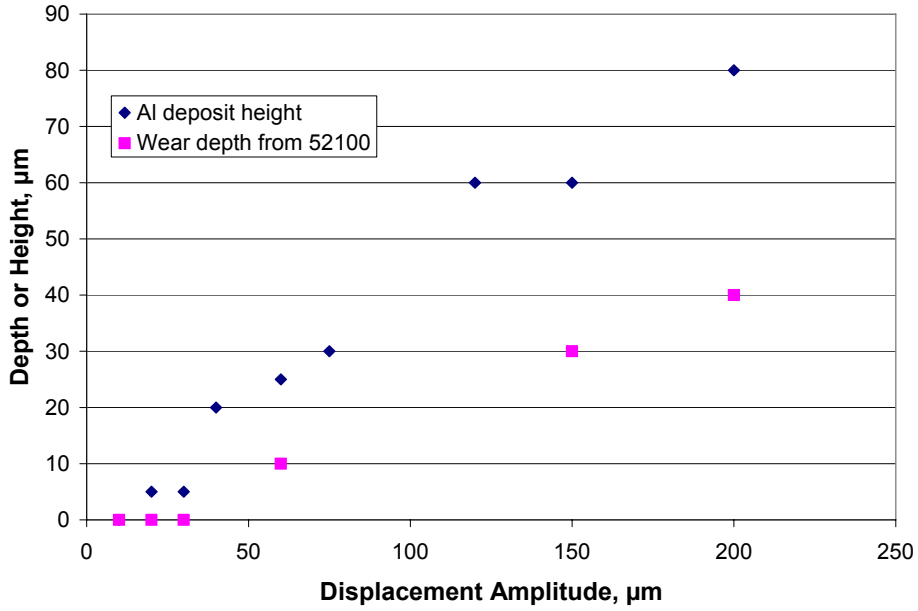

Figure 5.13: The height of aluminum deposited on 301 resulting from contact with A356 and the depth of wear of 301 resulting from contact with 52100 for various displacement amplitudes and a normal force of 255 N.

An estimate of the expected fretting scar width in the direction of fretting can be made based on the sum of the Hertz contact width (2a) and the displacement range. The experimentally observed widths of the fretting scars are approximately three times the width expected based on this calculation for all displacement amplitudes tested assuming each body is semi-infinite. For example, for a 20 µm displacement amplitude with a normal force of 255 N for contact of 301 with 52100 the expected scar width based on Hertz is 0.20 mm, whereas the average observed width is about 0.60 mm. Similarly, for the 200 µm displacement amplitude case the calculated and actual average scar widths are 0.56 and 2.20 mm respectively. Figure 5.14 shows the measured scar widths and the widths calculated based on a Hertz analysis for various displacement amplitudes and a normal force of 255 N for contact of 301 with both A356 and 52100. A test conducted

between 301 and 52100 for 100 cycles with a displacement amplitude of 50 μm and a normal force of 255 N generated an average scar width of approximately 0.40 mm compared to a width of 0.95 after 10^4 cycles and an expected width of 0.26 mm. Initial roughness and wear are partially responsible for a large portion of the increased width.

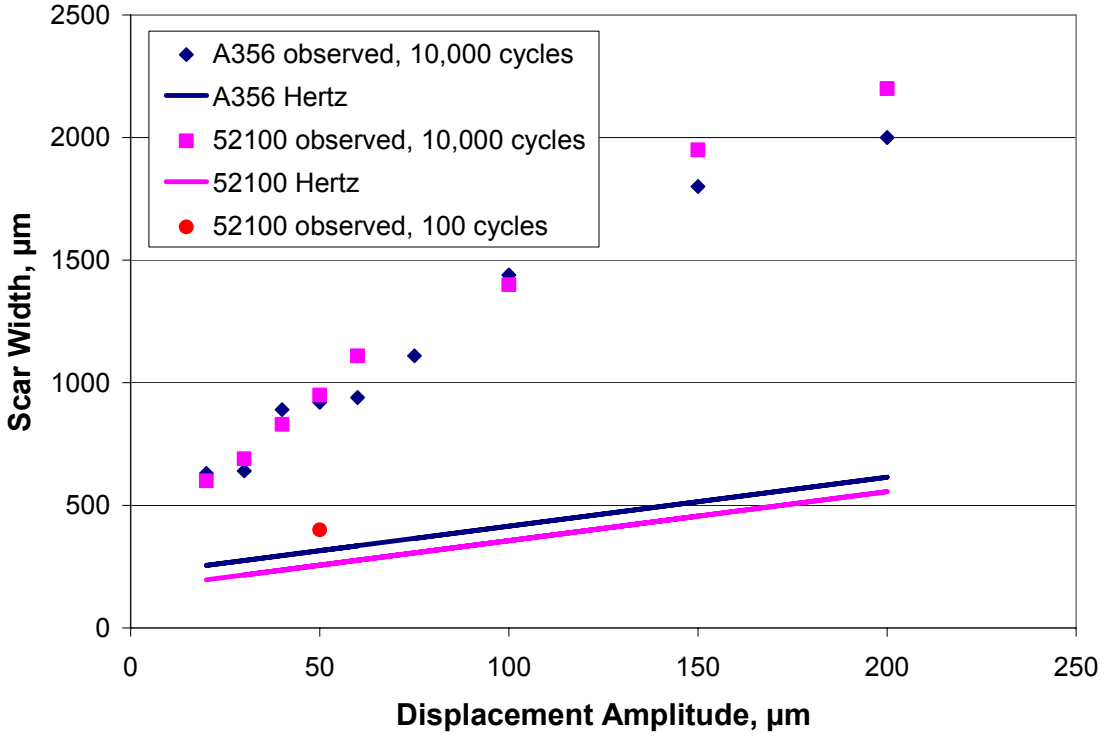

Figure 5.14: Average scar widths for contact of 301 with A356 and 52100 with a normal force of 255 N for various displacement amplitudes where points are experimental results and lines are calculated based on a Hertz analysis.

Another contributor to the increased contact width is the 89 μm thick compliant layer of PTFE between the specimen and the backing plate. The PTFE causes the specimen to conform to the contacting cylinder, thereby bending the specimen. This indicates that it is not appropriate to assume that the specimen is flat in the analysis to

determine the cyclic fretting contact stresses and that the PTFE layer needs to be taken into account in the cyclic stress analysis. When the specimen is removed after the fretting test, it is apparent that permanent deformation of the PTFE occurs during testing. The layer becomes thinner under the contact and extrudes to the side of the gage section. Under the specimen outside of the contact the thickness of the layer is equal to the original thickness. This confirms that the specimen is bent during testing.

The Hertz semi-contact-width (a) for a normal force of 255 N between 301 and 52100 is 78 μm. Therefore, the onset of reciprocating sliding would occur at a displacement amplitude of 78 μm for the idealized configuration. For A356 against 301 for a normal force of 255 N the Hertz semi-contact-width is 107 μm, and would transition to reciprocating sliding at 107 μm. However, the transition to reciprocating sliding will take place at a higher amplitude due to the increased contact size. The initial transition amplitude is approximately 150 μm for contact with 52100 based on the scar size after 100 cycles with a normal force of 255 N and 50 μm contact force when wear was not significant.

A crack was found that formed during a fretting test against 52100. Figure 5.15 shows a planar crack in a sample sectioned parallel to the fretting direction in a specimen with fretting damage generated with a displacement amplitude of 60 μm and a normal force of 255 N. The crack formed near the right edge of contact at an angle of 50 degrees from the surface and is approximately 100 μm in length. Cracks were not found in other samples, including samples tested under the same conditions. Cracks are less likely to form using the test setup in this work because of the bending of the specimens caused by the compliant layer of PTFE. The bending causes compressive normal stress parallel to

the contact surface where cracks would form. Future work is aimed at relating crack size and its characteristics including the aspect ratio, orientation, and number of cracks and their locations to the fretting conditions.

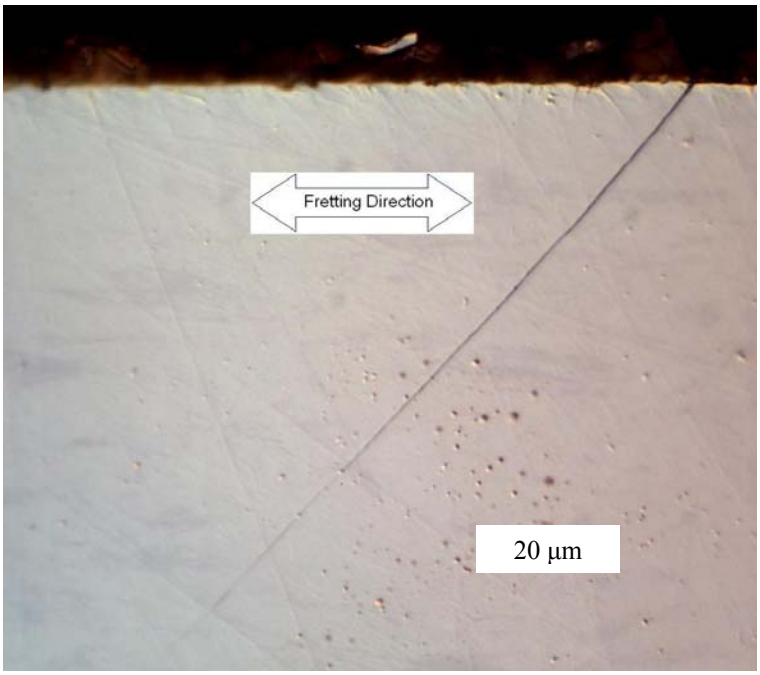

Figure 5.15: A planar crack near the right edge of contact formed after 10^4 cycles of fretting at a normal force of 255 N and displacement amplitude of 60 μm against 52100.

5.2 Residual Fatigue Life

The impact of the fretting damage on the fatigue behavior was determined by performing fatigue tests on dogbone specimens containing fretting damage using the same method described in Section 3.3.1. Subjecting the damaged specimens to cyclic stress either causes cracks to form and grow in the fretting damaged volume or causes cracks present from fretting to grow. Fretting conditions that are more severe result in a shorter life.

The fatigue response of specimens containing fretting damage generated by contact of 301 with 52100 at a displacement amplitude of 60 μm and normal force of 255 N for 10^4 cycles is compared to the response of the undamaged material in Figure 5.16. The fatigue limit of the fretting-damaged material is 257 MPa, compared to the undamaged fatigue limit of 468 MPa at R = 0.05. Hence, for this fretting condition there was a 45% knockdown in fatigue strength. This is a more severe knockdown in fatigue strength than the 30% maximum knockdown that has been found using other 300 series stainless steel in the annealed condition in contact with itself [16].

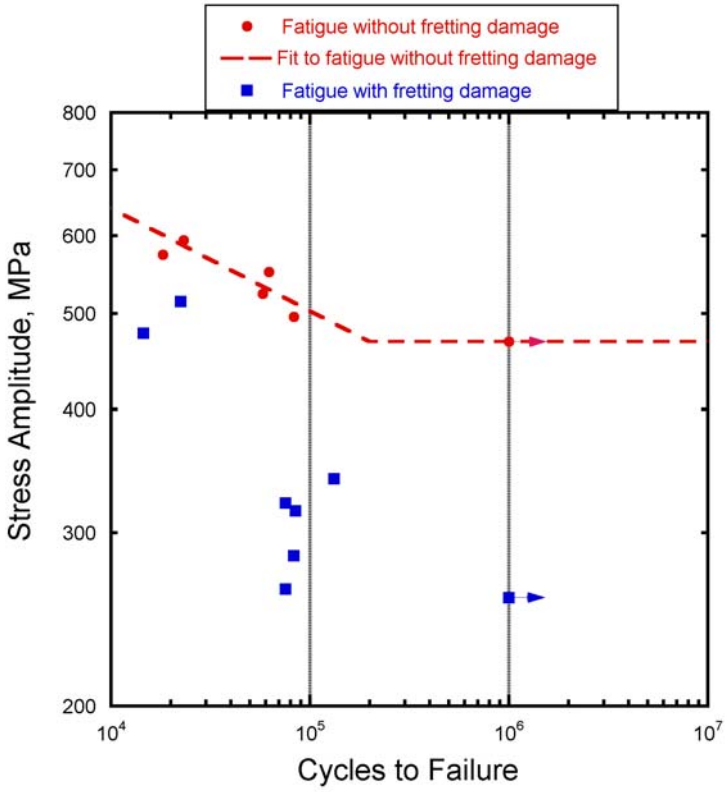

Figure 5.16: Knockdown in fatigue life due to fretting of 301 against 52100 with a normal force of 255 N and displacement amplitude of 60 μm for 10^4 cycles.

Figure 5.17 shows the front and back of a specimen subjected to fretting against 52100 for 10^4 cycles with a normal force of 255 N and 60 μm displacement amplitude and subsequently cycled to failure at a stress amplitude of 468 MPa and R = 0.05. Examining the back of the specimen where it is easy to distinguish features because of the lack of a fretting scar shows the presence of multiple initiation sites in the center of the specimen. Cracks grew outward until the final rupture of the specimen as made evident by the deformation bands on both edges of the specimen.

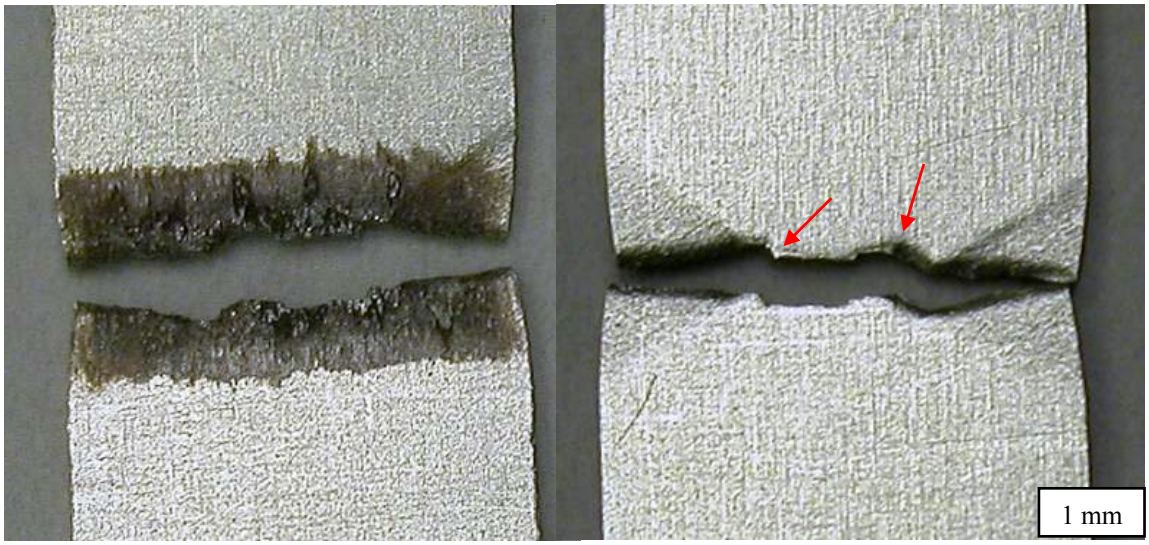

Figure 5.17: Front (left) and back (right) of a 301 specimen subjected to subsequent fatigue after fretting against 52100 for 10^4 cycles with a normal force of 255 N and displacement amplitude of 60 μm showing multiple crack initiation sites in the center of the specimen.

Fatigue tests were conducted with conditions corresponding to the fatigue limit in plain fatigue on the specimens containing different severities of fretting damage. Fretting damage was generated with 52100 at different displacement amplitudes and a normal force of 255 N for 10^4 cycles and subsequent fatigue was performed with a stress

amplitude of 468 MPa and a load ratio of R = 0.05. Figure 5.18 shows the resulting lives and failed specimens. Infinite life was found for a 10 μm displacement amplitude, which was the only test resulting in a partial slip running condition. The fatigue life decreases with increasing fretting displacement amplitude beyond the transition from partial to mixed slip. Therefore, there is a transition displacement amplitude below which there is no negative impact on fatigue strength occurring near the transition between partial and mixed slip conditions. At low displacement amplitudes, the catastrophic flaw is located near the center of contact. As the displacement amplitude increases, the critical fretting cracks formed closer to the edges of the contact as observed in the images of the scars and cracks in Figure 5.18. A specimen with fretting damage generated at a displacement amplitude 20 μm failed during fatigue at locations well outside of the primary fretting scar region, and was therefore not shown in this figure. The specimen for this test failed after 52,407 cycles. Therefore, the residual life associated with the fretting damage generated at 20 μm is greater than this value. This life is greater than the life of the specimen with fretting damage generated at a displacement amplitude of 30 μm, which is consistent with the trend of increasing life with decreasing displacement amplitude.

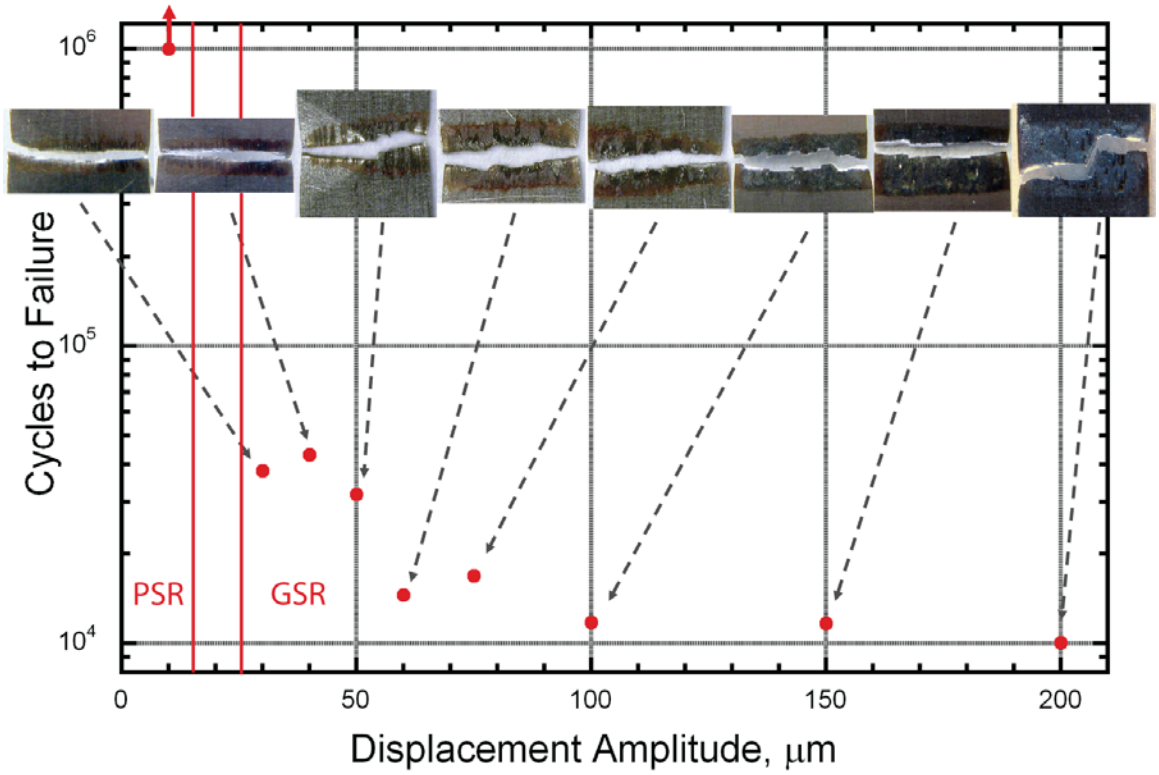

Figure 5.18: Residual fatigue life of specimens containing fretting damage generated by 301 in contact with 52100 at various displacement amplitudes with a normal force of 255 N for 10^4 cycles with running condition indicated. The fatigue tests were conducted at a stress amplitude of 468MPa and R = 0.05.

Figure 5.19 shows the resulting lives and fractured specimens for subsequent fatigue tests performed on 301 specimens contacted with A356 at different displacement amplitudes and a normal force of 255 N for 10^4 cycles. Infinite life was obtained for a displacement amplitude of 40 μm. Increasing displacement amplitude caused reduction in life until 100 μm at which point the life increased slightly. Above a threshold displacement amplitude, the cycles to failure is nearly independent of displacement amplitude. This displacement corresponds to a running condition near the transition from mixed slip to gross slip running conditions.

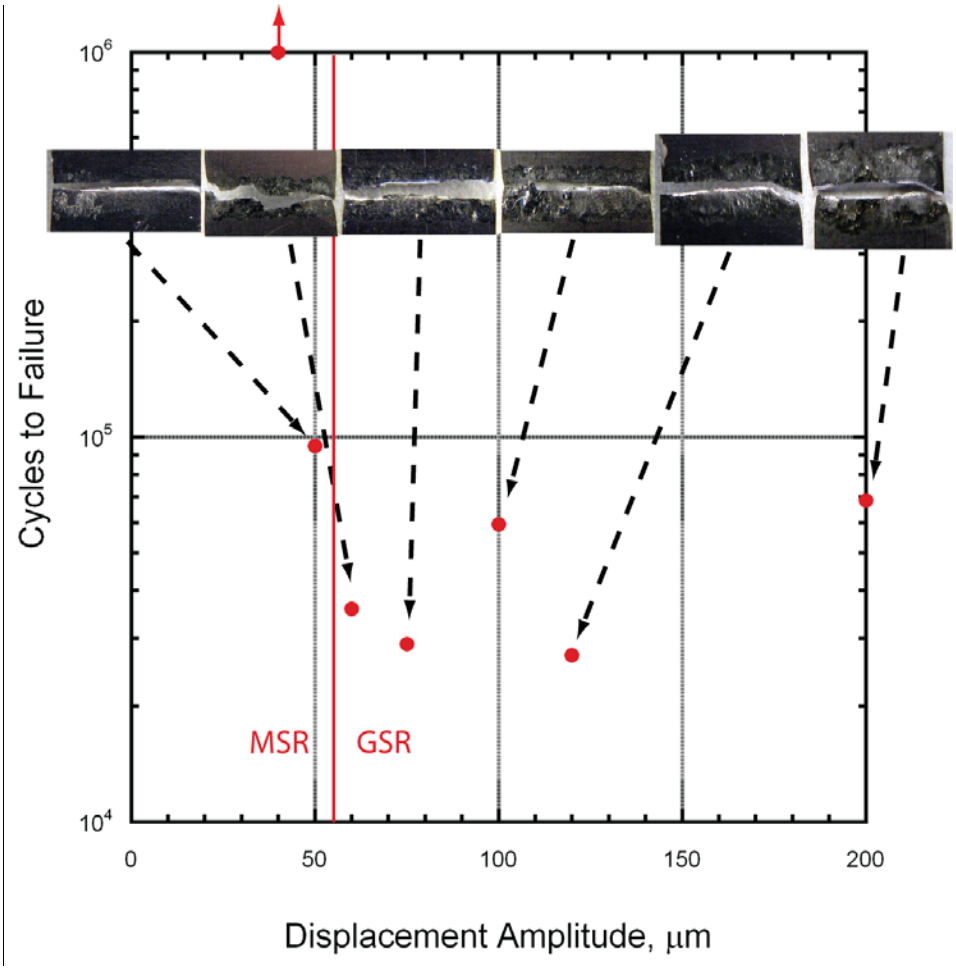

Figure 5.19: Residual fatigue life of specimens containing fretting damage generated by 301 in contact with A356 at various displacement amplitudes with a normal force of 255 N for 10^4 cycles with running condition indicated. The fatigue tests were conducted at a stress amplitude of 468MPa and R = 0.05.

Figure 5.20 shows a comparison between the residual lives obtained when 301 was contacted by A356 and 52100 with a normal force of 255 N and various displacement amplitudes for 10^4 cycles with the running condition indicated. The fretting damage was more severe for 301 in contact with 52100 for all displacement amplitudes.

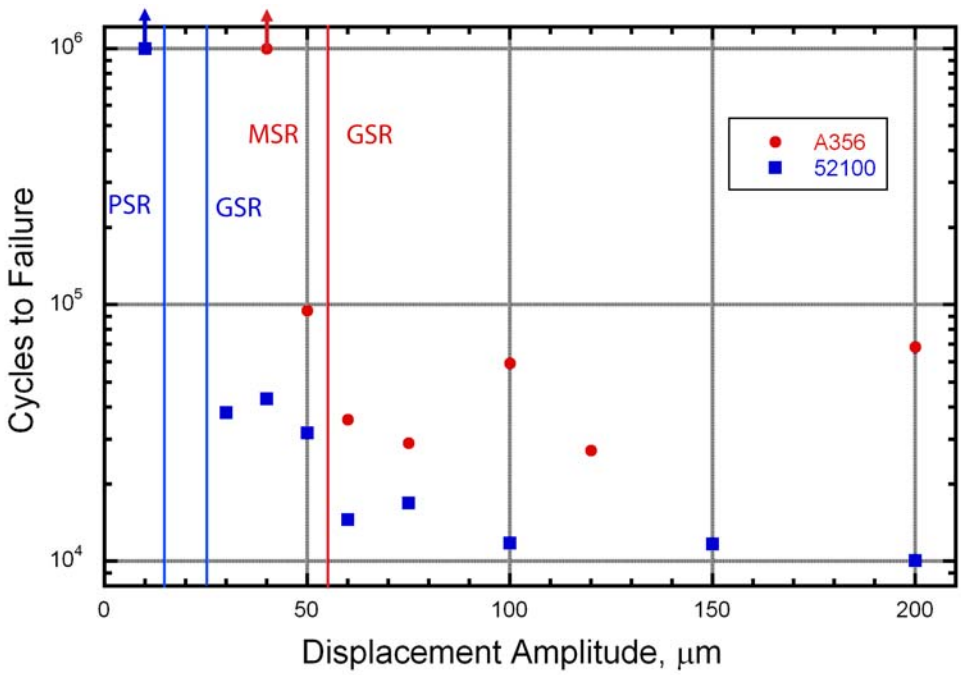

Figure 5.20: Residual fatigue life of specimens containing fretting damage generated by 301 in contact with both A356 and 52100 at various displacement amplitudes with a normal force of 255 N for 10^4 cycles with running condition indicated. The fatigue tests were conducted at a stress amplitude of 468MPa and R = 0.05.

As discussed in Chapter 2, the greatest reduction in fatigue life is expected to occur near the displacement amplitude relating to the transition between mixed and gross slip. However, in this study, the most severe knockdown occurred in the gross slip regime for contact with both A356 and 52100. The threshold displacement amplitude above which fretting affected life occurred just below the observed transition from mixed slip to gross slip for 301 in contact with both A356 and 52100.

At larger displacement amplitudes for thick specimens the fatigue life is expected to increase due to the increased wear rate at larger displacement amplitudes as well as the increased size of contact, causing a reduction in the local pressure [46, 47]. At high wear rates, the rate of material removal is larger than the rate of crack propagation. This results

in the removal of cracks which therefore increases the life of the component. In this study, life did not increase with displacement amplitude for contact with either material as expected. In contact with A356, there was a slight increase in life for a displacement amplitude of 200 μm, though the increase could be considered to be within experimental scatter. Since wear of the 301 specimen did not take place and cracks were not observed, any increase in life observed would not be due to the removal of cracks. Contact size was increased by wear of the aluminum specimen which may have caused the beneficial reduction in contact pressure. The deposited layer of aluminum may have had a protective effect, since the highest stresses from contact would occur in the deposited layer rather than the 301 specimen.

For contact with 52100, the life continued to decrease with increasing displacement. This is due to the reduction in specimen thickness due to wear. At high displacement amplitudes the wear depth was found to be up to 40 μm. This relates to a 20% decrease in cross-section area for these thin specimens. Calculating the stress amplitude based on the reduced area results in a fatigue life similar to the undamaged condition with the same stress as shown in Figure 5.21. The reduction in thickness would not be significant when testing with thick specimens.

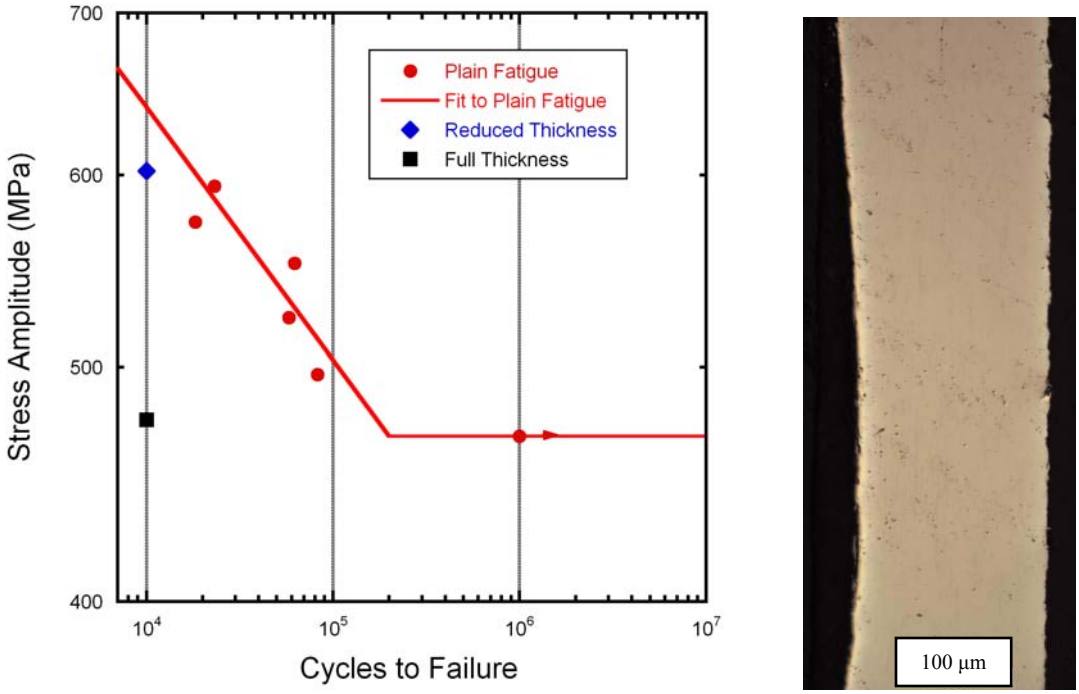

Figure 5.21: Change in actual stress amplitude due to wear of a sample fretted against 52100 with a normal force of 255 N and displacement amplitude of 200 μm for 10^4 cycles.

5.3 Fretting Crack Growth Modeling

The life of a component during fatigue is comprised of crack nucleation, microcrack propagation, and macrocrack propagation. Fretting promotes the nucleation of a crack and influences microcrack propagation, but has been shown not to effect the macrocrack propagation [98]. When fretting generates crack-like damage or damage where cracks form rapidly in the fretting damage volume due to fatigue, a crack growth methodology is a logical choice for life prediction.

Fellows et al. [37] successfully modeled the fretting fatigue lives of two materials by using an Equivalent Initial Flaw Size (EIFS) and a Paris crack growth model [99].

The EIFS represents damage caused by the fretting process, and subsequent crack growth is modeled using a fracture mechanics approach.

In this study, the program AFGROW [94] was used to model crack propagation from an initial flaw. The crack growth model used is based on the NASGRO 3.0 equation. The model was verified suitable to use on 0.2 mm thick specimens and R = 0.05 by comparing the results of the model to crack growth experiments conducted on the same sheet of 301 stainless steel as discussed in section 3.4.

Cracks generally formed on the face of the specimen, rather than at a corner or edge. Multiple cracks formed and appear to quickly link up to form the critical crack that grows under fatigue. Therefore, these multiple cracks are modeled as a center semi-elliptical crack, shown in Figure 5.22. The fretting direction is out of plane along the top surface and the cracks are perpendicular to the loading axis. Even though a crack was found to be angled in experiments, it is assumed that the cracks transition to stage II fatigue cracks rapidly, so a crack plane perpendicular to the loading axis is assumed.

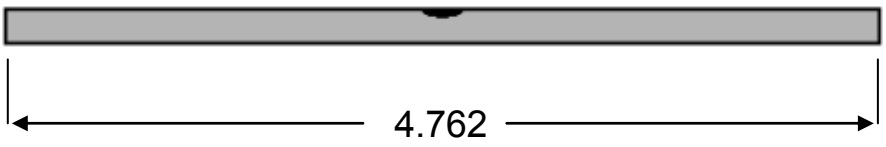

Figure 5.22: Cross sectional view of the modeled geometry.

The dimensions of the flaw were chosen to have a depth of 100 μm which is representative of the crack found from fretting against 52100, and the width was varied to find an appropriate prediction. The results of the model for several EIFS values are shown in Figure 5.23. The life resulting from an initial flaw with a width of 4 μm and

depth of 100 μm was found to correlate to the experimental data well below 10^5 cycles. However, the predicted fatigue limit was much lower, as shown by curve (a) in Figure 5.23. By increasing the value of the threshold stress intensity factor range at R = 0 (ΔK_0) from 3.846 to 6.654 MPa $m^{0.5}$ it was possible to match the observed fatigue limit using the same EIFS, as shown by curve (b) in Figure 5.23. However, it is unrealistic that the cracks generated have this aspect ratio. A semi-circular EIFS was also evaluated. A 32 μm wide flaw with a 16 μm depth and ΔK_0 = 4.989 MPa $m^{0.5}$ was used to generate a correlation to the experimental data, as seen by curve (c) in Figure 5.23. Further characterization of cracks generated in fretting is necessary to provide information about the actual depth and width of the cracks.

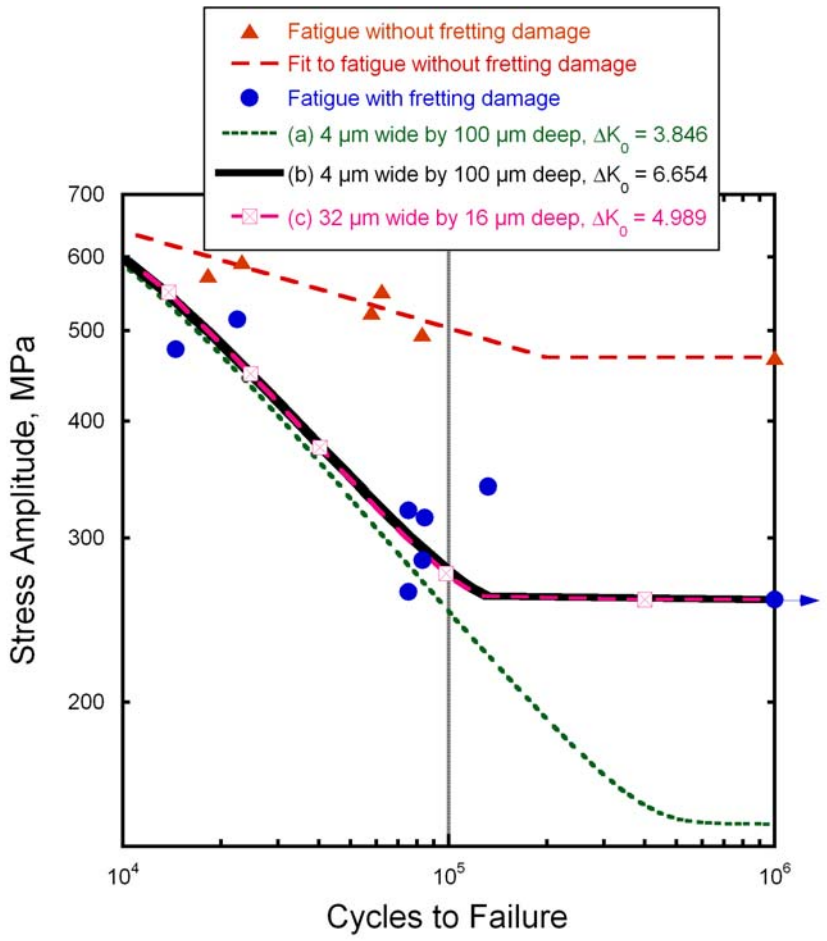

Figure 5.23: Fatigue behavior with and without fretting damage for R = 0.05. Fretting damage was generated with a 52100 contacting body, normal force of 255 N, and displacement amplitude of 60 μm for 10^4 cycles. Fatigue life curves were predicted by NASGRO assuming different initial crack sizes, geometries, and threshold stress intensity range values.

With a constant flaw size, increasing ΔK_0 results in an increase in fatigue life for all stress levels, with the greatest effect on the fatigue limit. The life predictions based on a crack growth analysis are most sensitive to the value of ΔK_0 and less sensitive to the initial flaw size and geometry.

One possible reason an increase in the value of ΔK_0 is needed is related to the orientation of the cracks present from fretting. The model treats the flaw as a straight crack, however the actual cracks were found growing at an angle of 50 degrees from the surface. This will increase the closure level and increase frictional interaction. Because the increase in ΔK_0 needed is fairly small, it is also possible that the material properties of the material tested differ from the values in the database enough to affect the response. Future work is needed to experimentally determine the threshold stress intensity for thin sheets of AISI 301 stainless steel.

The agreement between the model correlation and experimental results, particularly with regard to the ability to model the slope of the stress-life curve in the finite life regime, supports the assumption that fretting fatigue can be separated into a fretting damage stage that is associated with crack nucleation and microcrack growth within a fretting fatigue process volume (FFPV), or weakening of the FFPV so that crack formation occurs rapidly under cyclic loading, and subsequent macrocrack growth stage that involves the growth of these cracks by the bulk cyclic stresses. Fretting conditions that demonstrate a difference in subsequent stress-life behavior will correspond to a different EIFS, with a larger EIFS relating to a more severe fretting condition and a smaller EIFS relating to a less severe fretting condition. In this way, the EIFS characterizes the extent of fretting damage in a quantitative way.

CHAPTER 6

CONCLUSIONS AND RECOMMENDATIONS

6.1 Conclusions

An approach was developed for evaluating the fretting behavior of thin sheets. The approach includes evaluation of baseline structure and properties, conducting fretting tests using a specialized test system, and characterization of the damage using microscopy and subsequent fatigue testing. This approach was applied to study the fretting behavior of AISI 301 stainless steel in the full hard condition in contact with AISI 52100 steel and ANSI A356 cast aluminum. Friction logs were generated to understand the running condition and friction evolution. Fretting maps were generated based on the friction logs to show the running condition as a function of test conditions. The reduction in fatigue life was evaluated to identify the most damaging contact conditions. The following conclusions have been made from this study:

- Contact of 301 with A356 resulted in a large amount of transfer of aluminum to the 301 specimen in the mixed and gross slip regimes. The thickness of the layer increased with increasing displacement amplitude with a maximum of 80 μm at a displacement amplitude of 200 μm and normal force of 255 N. As a result, no wear of the 301 sample takes place.
- A significant amount of wear of the 301 specimen occurs when in contact with 52100 in the gross slip regime. The wear depth in the 301 sample tested at a normal force of 255 N and a 200 μm displacement amplitude for 10^4 cycles was 40 μm.

- For a given normal force, there is a threshold displacement amplitude below which there is no reduction in fatigue life. This threshold displacement amplitude occurs in the mixed slip regime near the transition to gross slip.
- The transfer of aluminum to the 301 specimen resulted in high tangential forces at the ends of the stroke. This was caused by the aluminum deposit on the 301 sample coming into contact with the edge of the wear scar on the aluminum body.
- With a normal force of 255 N, 301 displays a transition displacement amplitude below which the fretting damage is less severe. The transition occurred between 40 and 50 μm for contact with A356 and between 20 and 30 μm for contact with 52100.
- Fretting against 52100 at a displacement amplitude of 60 μm with normal force of 255 N for 10^4 cycles resulted in a 45% knockdown in the fatigue limit.
- The fretting fatigue life continues to decrease with increasing displacement amplitude for contact with 52100 with a normal force of 255 N and 10^4 cycles. This is a result of the increase in the wear rate causing a significant reduction in the net section thickness. The decrease in life at higher displacement amplitudes is not caused by increased crack formation.
- In all cases, a larger knockdown in fatigue life occurred in contact with 52100 than with A356. This is partially due to a protective effect cuased by the aluminum layer transferred to the 301 specimen.
- An EIFS calculated using a fracture-mechanics based crack growth methodology is useful for quantifying the severity of fretting damage. The threshold stress intensity range is the most sensitive parameter in this analysis, with the predicted

fatigue limit of materials containing fretting damage increasing with increasing threshold stress intensity range.

6.2 Recommendations

Now that an experimental approach has been developed and data has been generated, future work is needs to be aimed at understanding the fretting damage in 301 and then use these results to develop and calibrate fretting damage criteria.

- A fractographic study using a scanning electron microscope (SEM) should be performed to understand crack formation and propagation behavior. This will help determine the location of crack formation, including key microstructural features (e.g. inclusions or δ-ferrite stringers). Crack orientation and the possible role of microcrack coalescence in the formation of the catastrophic crack could also be determined. In addition, this will help determine if cracks initiate on the reverse side of the specimen due to the tensile bending stresses from the compliance of the PTFE layer. The role of bending can also be studied by performing tests without a compliant layer by using a lubricant rather than PTFE to alleviate damage to the specimen holder.
- The fatigue crack growth tests performed in this study did not capture the low crack growth rate behavior sufficiently. Decreasing ΔK tests should be performed to find the threshold stress intensity. This is critical to determine crack arrest in fracture mechanics based modeling.
- The role of the phase transformation from austenite to martensite has a significant effect on the fretting performance of austenitic stainless steels. However the effect

is not well understood. Performing fretting tests with the same contact conditions but at elevated temperature, even just 20 to 100^{o}C greater, will result in less martensite formation because of the sensitivity of austenite stability on temperature. Measurement of the martensite content in fretting scars resulting from tests at the different temperatures will aid in the understanding of the effect of martensite on the fretting performance. Measurement of martensite will be performed using Magnetic Force Microscopy (MFM), which is an adaptation of Atomic Force Microscopy (AFM) that uses a magnetic tip to measure forces. This will allow precise measurement of martensite location.

- Material properties at elevated temperature are needed in order to model elevated temperature fretting behavior. Therefore, tensile tests, fatigue tests, and crack growth tests should be performed at elevated temperature. Measurement of martensite formation in these tests will aid in the overall understanding of the effect of phase transformation on the material behavior.
- The wear rate affects the impact of fretting on the fatigue life. The role of oxidation on the wear rate can be studied by performing fretting tests in an argon environment. Comparing the life of samples tested in air to the life of samples tested in argon will show whether the formation of oxidation is beneficial to life.
- Testing using a different austenitic stainless steel such as 201 will provide insight about the role of austenite stability on the fretting behavior.
- The fretting test configuration causes some uncertainty in the resulting stress state because of the compliance introduced by the protective PTFE layer, the thickness of the specimens, and discrepancy between actual and measured displacement.

Creating a finite element model representing the test configuration will determine the actual cyclic stress state and the amount of slip between the contacting bodies. This will permit correlation between the experimental results and the slip and cyclic stress.

- With knowledge of the slip and cyclic stress state, damage parameters such as Smith-Watson-Topper, Fatemi-Socie-Kurath, and Ruiz's fretting damage parameter and fretting fatigue damage parameter can be evaluated. Relating the values of these parameters with the location of crack formation found during the fractographic study and the knockdown in fatigue life due to fretting found during experiments in this project will allow the determination of the critical values of these parameters, thus creating the ability to identify the propensity for fretting damage in other contact geometries. This ability will be invaluable for the design against fretting.

REFERENCES

1. Waterhouse, R.B., "Fretting Fatigue," International Materials Reviews, Vol. 37, No. 2, 1992, pp. 77-97.

2. Lamb, S., Casti Handbook of Stainless Steel and Nickel Alloys. 2001: CASTI Publishing Inc./ASM International.

3. Maxwell, P., A. Goldberg, and J. Shyne, "Influence of Martensite Formed During Deformation on the Mechanical Behavior of Fe-Ni-C Alloys," Metallurgical and Materials Transactions B, Vol. 5, No. 6, 1974, pp. 1319-1324.

4. Khan, Z. and M. Ahmed, "Stress-Induced Martensitic Transformation in Metastable Austenitic Stainless Steels: Effect on Fatigue Crack Growth Rate," European Journal of Radiology, Vol. 21, No. 3, 1996, pp. 201-208.

5. Pineau, A. and R. Pelloux, "Influence of Strain-Induced Martensitic Transformations on Fatigue Crack Growth Rates in Stainless Steels," Metallurgical and Materials Transactions B, Vol. 5, No. 5, 1974, pp. 1103-1112.

6. Schuster, G. and C. Altstetter, "Fatigue of Annealed and Cold Worked Stable and Unstable Stainless Steels," Metallurgical Transactions A (Physical Metallurgy and Materials Science), Vol. 14A, No. 10, 1983, pp. 2077-84.

7. Hsu, K.L., T.M. Ahn, and D.A. Rigney, "Friction, Wear and Microstructure of Unlubricated Austenitic Stainless Steels," Wear, Vol. 60, No. 1, 1980, pp. 13-37.

8. Talyan, V., R.H. Wagoner, and J.K. Lee, "Formability of Stainless Steel," Metallurgical and Materials Transactions A (Physical Metallurgy and Materials Science), Vol. 29A, No. 8, 1998, pp. 2161-72.

9. Garud, C., P. Nash, S. Mostovoy, and J.C. Benedyk. Microhardness Testing as a Method of Evaluating Bauschinger Phenomena in Cold Formed 301 Austenitic Stainless Steel Sheet Used in Automotive Head Gaskets. 2004. Charlotte, NC, United States: Minerals, Metals and Materials Society, Warrendale, PA 15086, United States.

10. Geringer, J., B. Forest, and P. Combrade, "Wear Analysis of Materials Used as Orthopaedic Implants," Wear, Vol. 261, No. 9, 2006, pp. 971-979.

11. Brown, S.A. and K. Merritt, "Fretting Corrosion in Saline and Serum," Journal of Biomedical Materials Research, Vol. 15, No. 4, 1981, pp. 479-488.

12. Iwabuchi, A., K. Kato, K. Hokkirigawa, and T. Suzuki, "Fretting Damage of Sus304 in a Vacuum (Discussion of the Condition of Crack Generation," JSME International Journal, Vol. 30, No. 266, 1987, pp. 1319-1325.

13. Kayaba, T. and A. Iwabuchi, "The Fretting Wear of 0.45% C Steel and Austenitic Stainless Steel from 20 to 650&Deg;C in Air," Wear, Vol. 74, No. 2, 1981, pp. 229-45.

14. Raman, S.G.S. and M. Jayaprakash, "Plain Fatigue and Fretting Fatigue Behaviour of Aisi 304 Austenitic Stainless Steel," Materials Science and Technology, Vol. 23, No. 1, 2007, pp. 45-54.

15. Sato, J., M. Sato, and S. Yamamoto, "Fretting Wear of Stainless Steel," Wear, Vol. 69, No. 2, 1981, pp. 167-77.

16. Nakazawa, K., N. Maruyama, and T. Hanawa, "Effect of Contact Pressure on Fretting Fatigue of Austenitic Stainless Steel," Tribology International, Vol. 36, No. 2, 2003, pp. 79-85.

17. Waterhouse, R.B., "Fretting at High Temperatures," Tribology International, Vol. 14, No. 4, 1981, pp. 203-207.

18. Wang, H.-W., Y.-L. Kang, Z.-F. Zhang, and Q.-H. Qin, "Size Effect on the Fracture Toughness of Metallic Foil," International Journal of Fracture, Vol. 123, No. 3-4, 2003, pp. 177-185.

19. Vingsbo, O. and S. Soderberg, "On Fretting Maps," Wear, Vol. 126, No. 2, 1988, pp. 131-47.

20. Waterhouse, R.B., "Fretting Fatigue," Applied Science Publishers, 1981.

21. Lindley, T.C. and K.J. Nix, "The Role of Fretting in the Initiation and Early Growth of Fatigue Cracks in Turbo-Generator Materials," ASTM STP 853, 1982, pp. 340.

22. Hoeppner, D.W., "Mechanisms of Fretting Fatigue and Their Impact on Test Methods Development," ASTM STP 1159, 1992, pp. 23-32.

23. Tomlinson, G.A., "The Rusting of Steel Surfaces in Contact," Proc. R. Sot . London, Ser. A, No. 115, 1927, pp. 472-483.

24. Waterhouse, R.B., "Fretting Corrosion " Pergamon Press, Oxford, 1972.

25. Shreir, L.L., Corrosion. 1963: John Wiley & Son, Inc., New York.

26. Sato, H., "Recent Trend in Studies of Fretting Wear," Transactions JSLE, Vol. 30, 1985, pp. 853-858.

27. Shaffer, S.J. and W.A. Glaeser, "Fretting Fatigue," Metals Handbook, Vol. 19, pp. 321-329.

28. Waterhouse, R.B., "The Role of Adhesion and Delamination in the Fretting Wear of Metallic Materials," Wear, Vol. 45, No. 3, 1977, pp. 355-64.

29. Doeser, B.A. and R.B. Waterhouse, "Metallographic Features of Fretting Corrosion Damage," Microstructural Science, Vol. 7, 1979, pp. 205-215.

30. Suh, N.P., "The Delamination Theory of Wear," Wear, Vol. 25, 1973, pp. 111-124.

31. Suh, N.P., "An Overview of the Delamination Theory of Wear," Wear, Vol. 44, No. 1, 1977, pp. 1-16.

32. Fleming, J.R. and N.P. Suh, "Mechanics of Crack Propagation in Delamination Wear," Wear, Vol. 44, No. 1, 1977, pp. 39-56.

33. Glaeser, W.A. and B.H. Lawless, "Behavior of Alloy Ti-6al-4v under Pre-Fretting and Subsequent Fatigue Conditions," Wear, Vol. 250-251, No. PART 1, 2001, pp. 621-630.

34. Conner, B.P., T.C. Lindley, T. Nicholas, and S. Suresh, "Application of a Fracture Mechanics Based Life Prediction Method for Contact Fatigue," International Journal of Fatigue, Vol. 26, No. 5, 2004, pp. 511-520.

35. Golden, P.J. and J.R. Calcaterra, "A Fracture Mechanics Life Prediction Methodology Applied to Dovetail Fretting," Tribology International, Vol. 39, No. 10, 2006, pp. 1172-1180.

36. Nowell, D., D. Dini, and D.A. Hills, "Recent Developments in the Understanding of Fretting Fatigue," Engineering Fracture Mechanics, Vol. 73, No. 2, 2006, pp. 207-22.

37. Fellows, L.J., D. Nowell, and D.A. Hills, "Analysis of Crack Initiation and Propagation in Fretting Fatigue: The Effective Initial Flaw Size Methodology,"

Fatigue and Fracture of Engineering Materials & Structures, Vol. 20, No. 1, 1997, pp. 61-70.

38. Hills, D.A., "Mechanics of Fretting Fatigue," Wear, Vol. 175, No. 1-2, 1994, pp. 107-113.

39. Wharton, M.H., D.E. Taylor, and R.B. Waterhouse, "Metallurgical Factors in the Fretting Fatigue Behavior of 70/30 Brass and 0.7% Carbon Steel by Fretting," Wear, Vol. 17, 1973, pp. 139-147.

40. Nicholas, T., "Critical Issues in High Cycle Fatigue," International Journal of Fatigue, Vol. 21, No. SUPPL, 1999, pp. 221-231.

41. Dobromirski, J.M., "Variables of Fretting Process: Are There 50 of Them?," ASTM Special Technical Publication, Vol. 1159, 1992, pp. 60-66.

42. Fouvry, S., P. Kapsa, and L. Vincent, "A Global Methodology to Quantify Fretting Damages," Fretting Fatigue: Advances, 2003, pp. 17-33.

43. Colombie, C., Y. Berthier, A. Floquet, L. Vincent, and M. Godet, "Fretting: Load Carrying Capacity of Wear Debris," Journal of Tribology, Transactions of the ASME, Vol. 106, No. 2, 1984, pp. 194-201.

44. Blanchard, P., C. Colombie, V. Pellerin, S. Fayeulle, and L. Vincent, "Material Effects in Fretting Wear: Application to Iron, Titanium and Aluminum Alloys," Metallurgical Transactions A (Physical Metallurgy and Materials Science), Vol. 22A, No. 7, 1991, pp. 1535-44.

45. Waterhouse, R.B., "Fretting Wear," Wear, Vol. 100, No. 1-3, 1984, pp. 107-118.

46. Gordelier, S.C. and T.C. Chivers, "A Literature Review of Palliatives for Fretting Fatigue," Wear, Vol. 56, No. 1, 1979, pp. 177-190.

47. Nishioka, K. and K. Hirakawa, "Fundamental Investigations of Fretting Fatigue. Iv. The Effect of Mean Stress," Bulletin of the Japan Society of Mechanical Engineers, Vol. 12, No. 51, 1969, pp. 408-14.

48. Malkin, S., D.P. Majors, and T.H. Courtney, "Surface Effects During Fretting Fatigue of Ti-6al-4v," Wear, Vol. 22, No. 2, 1972, pp. 235-244.

49. Magaziner, R., O. Jin, and S. Mall, "Slip Regime Explanation of Observed Size Effects in Fretting," Wear, Vol. 257, No. 1-2, 2004, pp. 190-197.

50. Madge, J.J., S.B. Leen, I.R. McColl, and P.H. Shipway, "Contact-Evolution Based Prediction of Fretting Fatigue Life: Effect of Slip Amplitude," Wear, Vol. 262, No. 9-10, 2007, pp. 1159-70.

51. Jin, O. and S. Mall, "Influence of Contact Configuration on Fretting Fatigue Behavior of Ti-6al-4v under Independent Pad Displacement Condition," International Journal of Fatigue, Vol. 24, No. 12, 2002, pp. 1243-1253.

52. Mindlin, R.D., "Compliance of Elastic Bodies in Contact," American Society of Mechanical Engineers -- Transactions -- Journal of Applied Mechanics, Vol. 16, No. 3, 1949, pp. 259-268.

53. Cattaneo, C., "Sul Contatto Di Due Corpi Elastici: Distribuzione Locale Degli Sforzi," Rendiconti dell' Accademia nazionale dei Lincei, Vol. 27, No. 6, 1938.

54. Hills, D.A. and D. Nowell, Mechanics of Fretting Fatigue. 1994, Dordrecht, The Netherlands: Kluwer Academic Publishers.

55. Ruiz, C., P. Boddington, and K. Chen, "An Investigation of Fatigue and Fretting in a Dovetail Joint," Experimental Mechanics, Vol. 24, No. 3, 1984, pp. 208-217.

56. Nowell, D. and D.A. Hills, "Mechanics of Fretting Fatigue Tests," International Journal of Mechanical Sciences, Vol. 29, No. 5, 1987, pp. 355-365.

57. Nowell, D. and D.A. Hills, "Crack Initiation Criteria in Fretting Fatigue," Wear, Vol. 136, No. 2, 1990, pp. 329-43.

58. Kuno, M., R.B. Waterhouse, D. Nowell, and D.A. Hills, "Initiation and Growth of Fretting Fatigue Cracks in the Partial Slip Regime," Fatigue & Fracture of Engineering Materials & Structures, Vol. 12, No. 5, 1989, pp. 387-98.

59. Ruiz, C. and K.C. Chen. Life Assessment of Dovetail Joints between Blades and Discs in Aero-Engines. 1986. Sheffield, Engl: Mechanical Engineering Publ Ltd, London, Engl.

60. Neu, R.W., J.A. Pape, and D.R. Swalla, "Methodologies for Linking Nucleation and Propagation Approaches for Predicting Life under Fretting Fatigue," ASTM Special Technical Publication, No. 1367, 2000, pp. 369-388.

61. Camp, J.M. and C.B. Francis, Making, Shaping and Treating of Steel. 6th Edition ed. 1951: United States Steel Co.

62. Sessler, J. and V. Weiss, Materials Data Handbook Type 301 Stainless Steel, N.A.a.S. Administration and G.C.M.S.F. Center, Editors. 1966: Huntsville, Alabama. p. 152.

63. Greenwood, G.W. and R.H. Johnson, "Deformation of Metals under Small Stresses During Phase Transformations," Royal Society -- Proceedings Transactions Series A, Vol. 283, No. 1394, 1965, pp. 403-422.

64. Fischer, F.D., G. Reisner, E. Werner, K. Tanaka, G. Cailletaud, and T. Antretter, "A New View on Transformation Induced Plasticity (TRIP)," International Journal of Plasticity, Vol. 16, No. 7-8, 2000, pp. 723-748.

65. Nosova, L.V., V.G. Serebryakov, and E.L. Estrin, "Dependence of the Plasticity of Dual-Phase Austenite-Martensite Steels on Phase Composition," Physics of Metals and Metallography (English translation of Fizika Metallov i Metallovedenie), Vol. 71, No. 5, 1991, pp. 191-194.

66. Estrin, E.I., "Martensite Transformations in Metals and Alloys," Steel in Translation, Vol. 24, No. 9, 1994, pp. 3.

67. Fischer, F.D., Q.P. Sun, and K. Tanaka, "Transformation-Induced Plasticity (TRIP)," Applied Mechanics Reviews, Vol. 49, No. 6, 1996, pp. 317-364.

68. Stringfellow, R.G., D.M. Parks, and G.B. Olson, "A Constitutive Model for Transformation Plasticity Accompanying Strain-Induced Martensitic Transformations in Metastable Austenitic Steels," Acta Metallurgica et Materialia, Vol. 40, No. 7, 1992, pp. 1703-16.

69. Haupt, S. and H.H. Strehblow, "Combined Surface Analytical and Electrochemical Study of the Formation of Passive Layers on Fe/Cr Alloys in 0.5 M H2so4," Corrosion Science, Vol. 37, No. 1, 1995, pp. 43-54.

70. Sugimoto, K. Passivity of Fe-Cr and Fe-Cr-Ni Alloys in High-Temperature Aqueous Solutions. 1985. Goteborg, Swed: Inst of Metals (Book n 320), London, Engl.

71. Marshall, P., Austenitic Stainless Steels - Microstructure and Mechanical Properties. 1984, London; New York: Elsevier Applied Science.

72. Voort, G.F.V., G.M. Lucas, and E.P. Manilova, eds. Metallography and Microstructures of Stainless Steels and Maraging Steels. Asm Handbook. Vol. 9: Metallography and Microstructures. 2004, ASM.

73. Narutani, T., "Effect of Deformation-Induced Martensitic Transformation on the Plastic Behavior of Metastable Austenitic Stainless Steel," Materials Transactions, JIM, Vol. 30, No. 1, 1989, pp. 33-45.

74. Tanaka, T., K. Ito, and K. Hoshino, "Effect of Alloying Elements, Cold-Rolling Reduction and Deformation-Induced Martensite on Mechanical Properties of Low Carbon Type 301 Hard Stainless Steel. (Development of Low Carbon High Strength Stainless Steels - Ii)," Transactions of the Iron and Steel Institute of Japan, Vol. 23, No. 4, 1982, pp. -140.

75. Kalkhof, D., M. Grosse, M. Niffenegger, and H.J. Leber, "Monitoring Fatigue Degradation in Austenitic Stainless Steels," Fatigue and Fracture of Engineering Material and Structures, Vol. 27, No. 7, 2004, pp. 595-607.

76. Miller, A., Y. Estrin, and X.Z. Hu, "Magnetic Force Microscopy of Fatigue Crack Tip Region in a 316l Austenitic Stainless Steel," Scripta Materialia, Vol. 47, No. 7, 2002, pp. 441-446.

77. Luksza, J., M. Ruminski, W. Ratuszek, and M. Blicharski, "Texture Evolution and Variations of A-Phase Volume Fraction in Cold-Rolled Aisi 301 Steel Strip," Journal of Materials Processing and Technology, Vol. 177, 2006, pp. 555-560.

78. Pineau, A.G., L.F. Van Swam, and R.M. Pelloux, "Cyclic Stress-Strain Curves of a Stainless Austenitic Steel in the M//S-M//D Range," Scripta Metallurgica, Vol. 7, No. 6, 1973, pp. 657-660.

79. Barclay, W.F. and Publ, Mechanisms of Deformation and Work Hardening in Aisi Type 301 Stainless Steel. 1965, American Society for Testing and Materials (ASTM), Philadelphia, PA, United States. p. 26-29.

80. Mughrabi, H. and H.-J. Christ, Cyclic Deformation and Fatigue of Selected Feritic and Austenitic Steels: Specific Aspects. Isij International. Vol. 37. 1997. 1154-1169.

81. Baudry, G. and A. Pineau, "Influence of Strain-Induced Martensitic Transformation on the Low-Cycle Fatigue Behavior of a Stainless Steel," Materials Science and Engineering, Vol. 28, No. 2, 1977, pp. 229-242.

82. Maier, H.J., B. Donth, M. Bayerlein, H. Mughrabi, B. Meier, and M. Kesten, "Low-Temperature Fatigue-Induced Martensitic Transformation of a Metastable Austenitic Stainless Steel: Optimization of Strength and Fatigue Properties," Zeitschrift fur Metallkunde, Vol. 84, No. 12, 1993, pp. 820-6.

83. Socie, D. Critical Plane Approaches for Multiaxial Fatigue Damage Assessment. 1993. San Diego, CA, USA: Publ by ASTM, Philadelphia, PA, USA.

84. Plumbridge, W.J., "Review: Fatigue-Crack Propagation in Metallic and Polymeric Materials," Journal of Materials Science, Vol. 7, No. 8, 1972, pp. 939-62.

85. Wright, R.N., "The High Cycle Fatigue Strength of Commercial Stainless Steel Strip," Materials Science and Engineering, Vol. 22, 1976, pp. 223-230.

86. Suh, N.P. and N. Saka, "The Stacking Fault Energy and Delamination Wear of Single-Phase F.C.C. Metals," Wear, Vol. 44, No. 1, 1977, pp. 135-143.

87. Kubota, M., N. Noyama, C. Sakae, and Y. Kondo, "Fretting Fatigue in Hydrogen Gas," Tribology International, Vol. 39, No. 10, 2006, pp. 1241-1247.

88. Kato, K., T. Suzuki, A. Iwabuchi, and K. Hokkirigawa, "Fretting Damage of Sus 304 in a Vacuum," JSME International Journal, Vol. 30, No. 260, 1987, pp. 330-336.

89. Nakazawa, K., M. Sumita, and N. Maruyama, "Fatigue and Fretting Fatigue of Austenitic and Ferritic Stainless Steels in Pseudo-Body Fluid," Journal of the Japan Institute of Metals, Vol. 63, No. 12, 1999, pp. 1600-8.

90. Bateni, M.R., J.A. Szpunar, X. Wang, and D.Y. Li, "Wear and Corrosion Wear of Medium Carbon Steel and 304 Stainless Steel," Wear, Vol. 260, 2006, pp. 116-122.

91. Leheup, E.R. and R.E. Pendlebury, "Unlubricated Reciprocating Wear of Stainless Steel with an Interfacial Air Flow," Wear, Vol. 142, No. 2, 1991, pp. 351-372.

92. Rice, R.C., Jackson, J. L., Bakuckas, J., and Thompson, S. (2003). "Metallic Materials Properties Development and Standardization (MMPDS)." DOT/FAA/AR-MMPDS-01, U.S. Department of Transportation, Federal Aviation Administration.

93. Dingdinger, P.M., Ultimate and Fatigue Properties of 301 Stainless Steel Sheet. 2005, Stork Technimet Inc.

94. Harter, J.A., Afgrow Users Guide and Technical Manual. 2006, Air Force Research Laboratory: WPAFB, OH.

95. Fouvry, S., P. Duo, and P. Perruchaut, "A Quantitative Approach of Ti-6al-4v Fretting Damage: Friction, Wear and Crack Nucleation," Wear, Vol. 257, No. 9-10, 2004, pp. 916-29.

96. Zhou, Z.R., Q.Y. Liu, M.H. Zhu, L. Tanjala, P. Kapsa, and L. Vincent, "Investigation of Fretting Behaviour of Several Metallic Materials under Grease Lubrication," Tribology International, Vol. 33, No. 2, 2000, pp. 69-74.

97. Zhou, Z.R., S. Fayeulle, and L. Vincent, "Cracking Behaviour of Various Aluminium Alloys During Fretting Wear," Wear, Vol. 155, No. 2, 1992, pp. 317-330.

98. Golden, P.J. and A.F. Grandt Jr, "Fracture Mechanics Based Fretting Fatigue Life Predictions in Ti-6al-4v," Engineering Fracture Mechanics, Vol. 71, No. 15, 2004, pp. 2229-2243.

99. Paris, P.C., M.P. Gomez, and W.P. Anderson, "A Rational Analytic Theory of Fatigue," The Trend in Engineering, Vol. 13, 1961, pp. 9-14.